Agglomeration of gold nanoparticles in microgravity

Dissertation

zur Erlangung des Grades

des Doktors der Naturwissenschaften

der Naturwissenschaftlich–Technischen Fakultät

der Universität des Saarlandes

von

Andrea Pyttlik

Saarbrücken
2024

Acknowledgments

First, I want to thank my supervisor **Prof. Dr. Tobias Kraus** for the great opportunity to perform my PhD thesis in the group "Structure Formation" at the Leibniz Institute for New Materials here in Saarbrücken. I want to thank you for all your guidance and your support during my project. You took time out of your busy schedule for all these insightful scientific discussions, and you established a lot of different contacts to facilitate a broader and more interdisciplinary network and cooperation possibilities.

A second special thanks goes to **PD Dr. Guido Falk** not only for the time and effort he invested in acting as my second referee but also for accepting to be my academic mentor during this thesis.

I want to thank **Dr. Andrea Vaccaro** and **Ricardo Armenta** from LS Instruments for their support on the development of the instrumental set-up. I especially want to thank Ricardo for all his help during the initial test at the drop tower. It would not have been possible to perform these DLS experiments in the drop tower in Bremen without your knowledge and skills regarding the design of DLS set-ups.

I want to thank the **DLR (German Aerospace Center)** for founding this project and making this thesis possible, especially for founding the performed drop tower experiments in Bremen.

A special thanks goes to **Dr. Thorben Könemann** and his team from **ZARM (Center of Applied Space Technology and Microgravity)** for all their support. Not only for the organization of the drop tower experiments but also for the integration of the experimental set-up into the drop tower capsule and the performance of the experiments. I want to thank you for all your support during the experiments. Thank you for all the insightful discussions and all the spontaneous adjustments, which were possible to implement directly on-site.

A very special thanks goes to **Dr. Björn Kuttich** for all his support and guidance during data analysis, preparation of the publication, and, of course, this thesis. Thanks for your company during our many business trips to Bremen and for making them so much more fun!

I would like to thank **Robert Strahl** and **Dr. David Doblas-Jimenez** very much for their help and support, especially during the early stages of this project. Your help and insights were

extremely valuable in realizing the experimental set-up, and your fellowship on business trips was highly appreciated.

Thanks to **Dr. Thomas Kister** for already guiding me through my Master Thesis, which made the start of my PhD-project so much easier for me. Many thanks also for the subsequent support throughout my whole PhD thesis!

I want to thank the whole structure formation group for creating such a wonderful working environment. Thanks to you guys, working in the lab was always fun! And of course, I want to thank you all for your supportive and productive cooperation during my project. In particular, I want to thank my good friends **Indra Backes**, **Michael Klos**, **Anja Colbus,** and **Dr. Long Zhang**.

From all my heart, I want to thank my dear parents, **Roswitha** and **Thomas Pyttlik**, for their sacrificial support throughout my life and for basically making these studies possible in the first place.

A thousand thanks to my two great sisters, **Anna** and **Christine Pyttlik**, for accompanying me through my whole life and for all the emotional support they provided to me in difficult times. Thank you both for all the advice and the fun we had together, but also for proofreading during my studies!

I want to thank my partner, **Dr. Philipp Willmes,** for all his help and understanding during this time, as well as his invaluable support during this thesis. Especially for all the hard work he put in, the countless proofreading he did and the scientific discussions we had about the project.

Abstract

The arrangement and distribution of nanoparticles inside a matrix crucially affect the material properties of nanocomposites. Agglomeration of the particles and the gravitational sedimentation of the agglomerates can alter the structure of the particles inside the matrix. To quantify the influence of gravity, agglomeration experiments were performed under normal and microgravity conditions. An experimental set-up was successfully developed to study the temperature induced agglomeration of hexadecanethiol-capped gold nanoparticles in tetradecane with dynamic light scattering. The sample was heated inside an aluminum block and injected into the pre-cooled measurement cell. Microgravity experiments were realized in the drop tower of the ZARM Institute (Bremen, Germany), providing a microgravity duration of 9.3 s. Comparing those measurements with the corresponding ground experiments showed the formation of larger agglomerates in microgravity, indicating a more reaction-limited agglomeration on ground and a more diffusion-limited agglomeration in microgravity. In line with this assumption, a stronger dependency between the initial particle concentration and the size of the formed agglomerates was observed in microgravity. Increasing the gold concentration by a factor of 2.7 on ground doubled the hydrodynamic diameter. In microgravity, however, increasing the gold concentration by a factor of 3.8 led to an increase in the hydrodynamic diameter by a factor of 3.8.
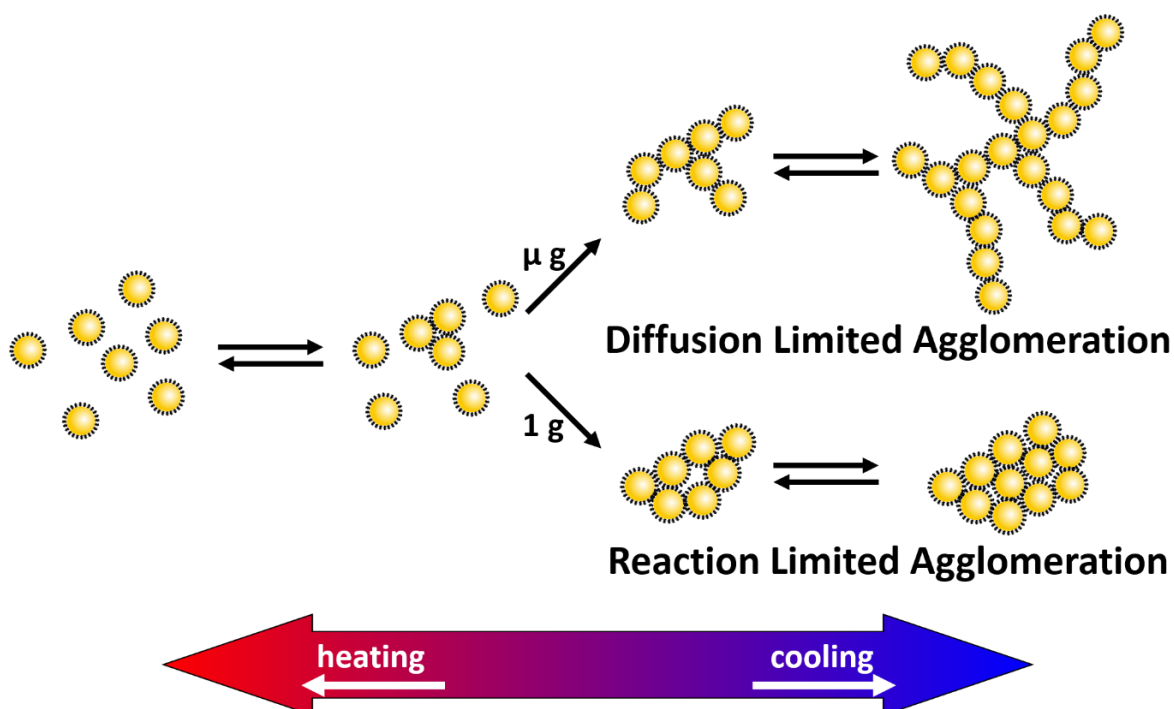
Zusammenfassung

Die Anordnung und Verteilung von Nanopartikeln in einer Matrix hat wesentlichen Einfluss auf die Eigenschaften von Nanokompositen. Die Agglomeration der Partikel und Sedimentation der Agglomerate können die Anordnung der Partikel innerhalb der Matrix verändern. Um den Einfluss der Schwerkraft zu quantifizieren, wurden Agglomerationsversuche unter normalen - und Mikrogravitationsbedingungen durchgeführt. Ein Versuchsaufbau zur Verfolgung der temperaturinduzierten Agglomeration von Hexadecanthiol stabilisierten Goldnanopartikel in Tetradecan mit dynamischer Lichtstreuung wurde erfolgreich entwickelt. Die Probe wurde in einem Aluminiumblock erhitzt und in die vorgekühlte Messzelle injiziert. Mikrogravitationsexperimente wurden im Fallturm des ZARM-Instituts (Bremen, Deutschland) mit einer Mikrogravitationsdauer von 9,3 s durchgeführt. Der Vergleich der Messungen mit den Bodenexperimenten zeigte die Bildung größerer Agglomerate in Schwerelosigkeit, was auf eine eher reaktionslimitierte Agglomeration am Boden und eine eher diffusionslimitierte Agglomeration in Mikrogravitation hinweist. Damit übereinstimmend wurde eine stärkere Abhängigkeit zwischen der Partikelkonzentration und der Größe der gebildeten Agglomerate in Schwerelosigkeit gefunden. Am Boden führte die Erhöhung der Konzentration um den Faktor 2,7 zur Verdopplung des hydrodynamischen Durchmessers. In Mikrogravitation führte die Erhöhung der Konzentration um den Faktor 3,8 zur Erhöhung des Durchmessers um den Faktor 3,8.
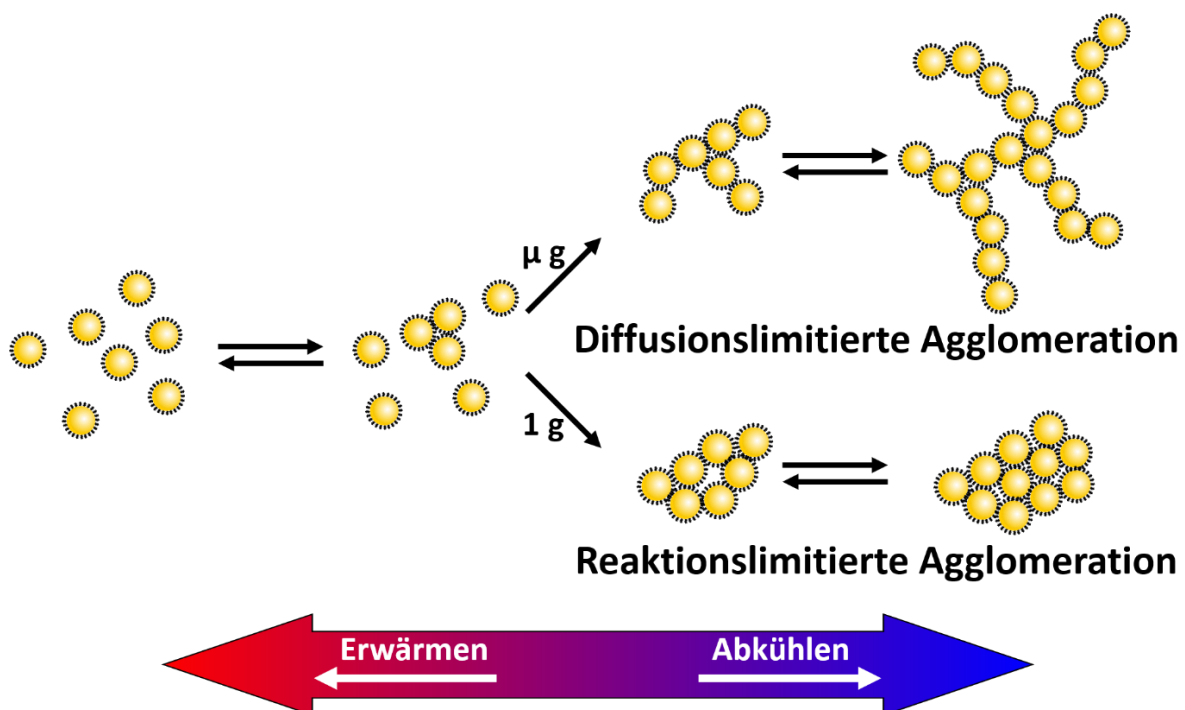
Publications and Statement of Contributions

Publication 1

A. Pyttlik, B. Kuttich, T. Kraus, „Microgravity Removes Reaction Limits from Nonpolar Nanoparticle Agglomeration", *Small* **2022**, *18(46)*, 2204621 (1-6).

- *Andrea Pyttlik:* Planning and performance of experiments; data analysis; writing of the original draft; visualization
- *Björn Kuttich:* Data analysis; review and editing; visualization
- *Tobias Kraus:* Conceptualization; methodology; review and editing; project administration; funding acquisition

Publication 2

A. Pyttlik, B. Kuttich, T. Kraus, „Dynamic Light Scattering on Gold Nanoparticles in Mircorgravity in a Drop Tower", *Microgravity Sci. Technol.* **2022**, *34*, 1–11.

- *Andrea Pyttlik:* Planning and performance of experiments; data analysis; writing of the original draft; visualization
- *Björn Kuttich:* Data analysis; review and editing; visualization
- *Tobias Kraus:* Conceptualization; methodology; review and editing; project administration; funding acquisition

This project was conducted at the Leibniz Instite for New Materials in Saarbrücken, in the program division "Strcture Formation". Many collegues of the institute offered their valuble contribution to the project, which I want to acknowledge here.

Particle characterization

TEM images were recorded by Anna Zimmermann.

SAXS experiments and the data analysis were done in cooperation wih David Doblas-Jimenez and Björn Kuttich.

ICP-OES measurements were conducted by Andrea Jung.

Instrumental set-up

The DLS instrument was modified by LS Instruments.

The heating stage and the liquid handling system of the experimental set-up were built in collaboration with Robert Strahl and the team from the technical workshop of the INM.

Microgravity experiments

Microgravity experiments were performed at the ZARM Institute in Bremen (Center of Applied Space Technology and Microgravity). The coordination of the experiments was done in collaboration with Thorben Könemann. The drop experiments and catapult launches on side were prepared and performed together with the ZARM Operations and Service team.

Hypergravity experiments

Hypergravity experiments were performed at Bremen University. The coordination of the experiments was done in collaboration with Thorben Könemann from ZARM. The centrifuge experiments on side were prepared and performed together with Bernd Carsten Sander.

List of Abbreviations

1 g	Earth's acceleration on ground
A	Amplitude of the correlation function
a	Acceleration
A_{coh}	Coherence area of the particles
B	Baseline of the correlation function
β	Friction constant
β_{Tetra}	Thermal expansion coefficient of tetradecane
c_{P_Tetra}	Isobaric heat capacity of tetradecane
CCF	Critical Casimir Forces
CTAB	Cetrimonium bromide
χ_{Agglo}	Agglomeration fraction
$\Delta\rho_S$	Difference in scattering length densities
ΔT	Temperature difference
Δt	Reaction time
Δx	Distance between scattering particle and detector
d	Diameter of the particles
d_{Core}	Core diameter
D_{Diff}	Diffusion coefficient
D_f	Fractal dimensions
d_H	Hydrodynamic diameter
d_L	Ligand length
DLA	Diffusion-limited aggregation
DLR	German Aerospace Center

DLS	Dynamic light scattering
ϕ	Volume concentration
ϕ_{Agglo}	Volume concentration of the agglomerated particles
ϕ_{Dis}	Volume concentration of the dispersed particles
φ	Volume fraction
$F(q)$	Form factor
F_B	Buoyancy force
F_F	Friction force
F_G	Gravitation force
G	Period function
$g_1(\tau)$	Correlation function of the electric field
$g_2(\tau)$	Normalized autocorrelation function
h	Height of free fall tube
k_B	Boltzmann constant
k_{Tetra}	Thermal conductivity of tetradecane
η	Dynamic viscosity
η_{Tetra}	Dynamic viscosity of tetradecane
η_V	Hard-sphere volume fraction
$I(q)$	Scattering Intensity of the scattering vector q
$I(t)$	Time dependent scattering intensity
I_{Agglo}	Scattering Intensity of the agglomerated particles
I_B	Scattering Intensity of the background
I_{Dis}	Scattering Intensity of the dispersed particles
I_{Par}	Scattering Intensity of the core particles

I_{Sol}	Scattering Intensity of the solvent
l	Characteristic particle length
λ	Wavelength
λ_{max}	Absorption maximum
ISS	International Space Station
μ	Particle mobility
μg	Microgravity
m	Mass of the particles
m_S	Mass of the solvent
MSL-1	Microgravity Science Laboratory
N	Number of scattering particles
n	Refractive index
N_{Agglo}	Agglomeration number
NASA	National Aeronautics and Space Administration
NFS	Near field scattering
OAm	Oleylamine
P	Sticking Probability
$p(r)$	Polydispersity of the particles
PCS	Physics of Colloids in Space
PMMA	Polymethylmethacrylat
PS	Polystyrene
q	Modulus of the scattering vector
$\vec{q}$	Scattering vector
ρ	Density

ρ_{Au}	Density of gold
ρ_{Tetra}	Density of teradecane
ρ_P	Density of the particle
ρ_{rel}	Relative density
ρ_S	Density of the solvent
r	Radius of the scattering volume
r_{Avg}	Average core radius of the particles
r_{Core}	Core radius of the particles
r_H	Hydrodynamic radius
r_{H0}	Hydrodynamic radius of a single particle
r_{HS}	Hard sphere radius
RLA	Reaction-limited aggregation
$RMSD$	Root mean squared displacement
σ	Deviation of average particle radius r_{Avg}
$S(q)$	Structure factor
SAXS	Small angle X-ray scattering
SEM	Scanning electron microscopy
SODI-COLLOID	Selectable Optical Diagnostic Instrument
θ	Scattering angle
T	Temperature
T_{Agglo}	Agglomeration temperature
t	Time
t_{Diff}	Diffusion time
t_{Sed}	Sedimentation time

Γ	Ratio of the sedimentation time t_{Sed} and the diffusion time t_{Diff}
τ	Delay time
τ_{Diff}	Mean residence time
TEM	Transmission electron microscopy
UV light	Ultraviolet light
UV/Vis	Ultraviolet/visible light
V	Scattering volume
v	Sedimentation velocity
v_0	Initial velocity
v_F	Fractal exponent
V_P	Volume of the particle
w	Laser beam width
x	Travelled distance
x_0	Initial height
z	Characteristic length
ZARM	Center of Applied Space Technology and Microgravity

Contents

1 Introduction

Gravity is an all-encompassing force. In physics it is one of the Four Fundamental Interactions, besides strong interaction, weak interaction and electromagnetism.[1] Even though it is the weakest,[2] it probably plays the most recognized role in our everyday life. On Earth it is responsible for physical objects having a weight,[3] and it gives the universe the structure we know.[4] Gravity inherently guides the growth of plants (gravitropism)[5,6] and is causing the tides of the oceans,[7] to name only some prominent examples. While the phenomenon of gravity has fascinated scholars back to ancient times, modern physicists and also material scientists are still attracted by exploring the versatile facets of gravity.

Gravity affects all matter not only on a macroscopic scale but also on a micro- and nanoscopic scale. Gravitational acceleration leads to convection and sedimentation.[8,9,10,11] Convection occurs as the result of a temperature gradient inside a medium. For example, when the bottom layer of a fluid is heated, the heated layer expands resulting in a decreased density compared to the cooler top layer of the fluid. Due to gravitational acceleration, the cooler top layer will start to sink and the warmer bottom layer will start to rise.[8] A similar effect can be observed during sedimentation, where particles with a larger density will settle in a medium with a lower density.[11] These two effects result in a directed motion of matter and accordingly in mechanical, hydraulic and hydrodynamic stresses, that impact various different processes and phenomena.[12,13,14] An effect of gravity has been reported for crystallization processes, for example on the crystallization of hard spheres,[12] semiconductors,[15] ionic crystals,[16] macromolecules,[17,18] proteins [19,20,21,22] and even of viruses.[23] Notably, during the formation of hybrid materials, the distribution of different components inside hybrid materials can be affected by gravitation.[24,25] An important family of materials are nanocomposites, where nanoparticles are embedded into a polymer-matrix to tune its properties.[26] The type of particles utilized as filler can alter mechanical, dielectric or optical characteristics of the material.[27,28,29] These characteristics of the final material depend on the composition, shape and size of the nanofillers.[30,31] The volume fraction and the spatial distribution of the fillers change key properties of the materials.[32,33,34] For example, a homogeneous distribution of nanofillers can enhance the mechanical properties of the polymer while retaining its flexibility.[35,36] Percolating superstructures of conductive (e.g. silver) or porous particles (e.g. carbon black) increase electrical or ion transport and thus conductivity.[37,38] To realize specific

structures inside a matrix, the particle distribution can be manipulated by particle self-assembly. For example, the formation of gold nanowire networks can be exploited to synthesize various conductive composites,[39] which can be used as sensors,[40,41] or implementable or wearable bioelectronics.[42,43,41] By applying an electrical field on the nanocomposite, semiconductor nanorods have been arranged inside solar cells.[44] Alivisatos *et al.* demonstrated that carbon black networks can be aligned to obtain conductive nanocomposites.[45] DNA guided self-assembly of gold nanorods can be used for the manufacturing of nanoelectronics or drug carriers.[46,47]

During the preparation of hybrid materials, the distribution and the arrangement of filler particles can be influenced by the agglomeration of the filler particles and by gravity. Gravity can affect the distribution of larger nanoparticles and their superstructures, and thus can lead to concentration gradients of the filler inside the matrix that change material properties.[48,49]

The investigation of the influence of gravity on the agglomeration process of particles, or particle dynamics in general, remains challenging. There are only very few practical approaches to study particle dynamics, undisturbed of gravitational acceleration.

One of them is known as density matching. Thereby the density difference between the colloidal particles and solvent is minimized to prevent the sedimentation of the particles and to simulate microgravity conditions.[50,51,52] It is an accessible and affordable option since no alterations to any conventional experimental set-ups are required. However, combinations between colloidal metal particles and dispersion medium with a matching density are uncommon, leading to limited options on samples to investigate. The most prominent samples are PMMA or stearylated-silica particles dispersed in halogenated hydrocarbons.[53,54] By matching the density of the solvents to the density of the particles, other parameters of the systems are inevitably changed, such as the refractive index, the polarity, or the salt concentration, and therefore possibly influencing the stability of the particles.

Another possibility is the performance of experiments under microgravity conditions. Four major options exist for achieving microgravity conditions: Space stations, such as the International Space Station (ISS),[55,56] sounding rockets,[57] parabolic flights,[58] and drop tower facilities.[59,60,61] Generally, experiments in microgravity are challenging due to their restricted accessibility and the high costs of the experiments.[62]

Dynamic light scattering (DLS) is a commonly used tool to analyze particle dynamics of colloidal systems, from submicron to micro scale particles.[63,64] By determining the hydrodynamic diameter and the polydispersity of particles, the growth [65,66,67] or the colloidal stability of particles,[68,69] polymers [70,71] and proteins can be investigated.[72,73] DLS instruments are easy to use and they can be built compactly and robustly. Due to these benefits, DLS measurements are well-established in microgravity.[74,75,76,77,78]

Nanoparticles based on gold have received considerable attention due to multiple applications, from catalysis[79] over imaging[80] and sensing [81,82,83] to drug delivery systems.[84,85] They are important filler particles for nanocomposites,[86,87] functional inks,[88,89,90] in thermochromic materials,[91] or biosensors.[92,93] Particle dynamics and the interaction between gold nanoparticles in colloidal systems are affected by temperature, which plays an important role for their colloidal stability, dictating if the particles are well dispersed or agglomerated.[94] Alkylthiol-capped gold nanoparticles show a completely reversible temperature induced agglomeration. By cooling these particles under a certain temperature (agglomeration temperature), the agglomeration of the particles can be induced. By reheating the agglomerates, the particles can be redispersed. The agglomeration temperature strongly depends on the diameter of the gold nanoparticle,[94] the length of the ligand used to stabilize the particles [95,96] and the concentration of the particles.[97] The temperature-dependent reversible agglomeration of nanoparticles provides the opportunity to investigate the effect of gravity on the agglomeration process by repeating the same experiments under normal (1 g) and under microgravity conditions (μ g). A similar study has already been reported by Potenza *et al*. using the SODI-Colloid instrument on the International Space Station (ISS).[98] The early stages of agglomeration of latex particles in water were studied via near filed scattering measurements.[98] In this project the influence of gravity on the temperature induced reversible agglomeration of sterically stabilized non-polar nanoparticles was investigated.

Despite both, the attention nanocomposites have received during the last decades, and the relevance of gravity during the formation of materials, to the best of our knowledge no study of high-density nanoparticles in dispersion has been reported in the absence of gravity. We decided to exploit the temperature dependent behavior of alkylthiol-capped gold nanoparticles to investigate the agglomeration process of this system in microgravity.

1. Introduction

As the most appropriate option to study microgravity experiments, the drop tower at the ZARM Institute (Center of Applied Space Technology and Microgravity) in Bremen (Germany) was identified. While a drop experiment provides a microgravity interval of 4.7 s, a unique catapult system extends it to 9.3 s, which appeared sufficient to collect agglomeration process data. However, inherent physical stresses have to be taken into account, launch and impact in the landing phase cause accelerations effects up to 50 g.[99] The drop tower offers the most accessible and affordable option to perform microgravity experiments. However, due to the high maintenance and operation cost of the tower and the time needed to evacuate and ventilate the tower, only 2-3 experiments can be performed per day restricting the access of the drop tower and resulting in a high cost per microgravity experiment.

In cooperation with LS Instruments AG (Fribourg, Switzerland) an instrumental set-up was developed to withstand the lift-off and landing phase and to be able to introduce a fast agglomeration of the particles at a well-defined moment. The instrumental set-up consists of a temperature-controlled liquid handling system to create a fast temperature drop and induce fast agglomeration of the particles, and a dynamic light scattering instrument to follow agglomeration. The gold nanoparticles are heated above their agglomeration temperature for an extended period of time to ensure that the particles are completely deagglomerated and fully dispersed in the solvent. During the microgravity experiments, a defined volume of the sample is injected into the pre-cooled measurement cell right before the lift off of the instrumental set-up. Autocorrelation functions were recorded as soon as the sample injection was completed.

This thesis is structured as follows: First, the instrumental DLS set-up developed in this project is discussed in detail. Subsequently, the study of a non-agglomerating reference system is reported. Particle dynamics of non-agglomerating oleylamine-capped gold nanoparticles in tetradecane are followed at a constant temperature and with a rapid temperature drop by DLS measurements on ground (1 g) and in microgravity (μ g). Next, the agglomeration process of hexadecanethiol-capped gold nanoparticles in tetradecane on ground is discussed. Investigations are performed at two different initial particle concentrations. The evolution of their average mean residence times and the corresponding hydrodynamic diameters are reported. Finally, results of the agglomeration experiments repeated under microgravity conditions are described. Experiments at two different initial particle concentrations are performed with catapult launches. To assess possible effects of the catapult launch, a drop

experiment is performed with one particle concentration. As the final conclusion of this thesis, a proposal for different agglomeration mechanisms on ground and in microgravity are discussed to explain differences in agglomerate growth. The data collected clearly indicate the transition from a reaction limited agglomeration on ground to a diffusion limited agglomeration in microgravity.

2 State of the Art

2.1 Gold nanoparticles

Nanoparticles are commonly defined as particles of a size between 1 and 100 nm[100] or 10 and 1000 nm in at least one dimension.[101,102] They show unique properties compared to their bulk form due to their high surface area to volume ratio,[103,104] and possible quantum effects.[105,106] Additionally, their optical properties such as absorption, scattering or the occurrence of plasmon resonance are strongly size dependend.[107,108] Nanoparticles are so small that they are less effected by gravity, resulting in a more free mobility of the particles in dispersions.[109] They can consist of numerous materials, such as metal,[110] metal oxide,[111] semiconductors,[112,113] carbon,[114,115] silicon,[116,117] or polymers.[118,119]

Nanoparticles are commonly and broadly used in today's industry,[120,121,122] for example as pigments, as UV protectors, catalysts, antimicrobial additives, or in functional coatings.[123] Gold nanoparticles are used in drug delivery systems,[124,125] biosensors,[126,127] the synthesis of various nanocomponents,[128,129] or functional inks.[130,131] To prevent agglomeration, the surface of gold nanoparticles is modified with surfactants, either by adsorption or chemical bonding.[111] Aqueous dispersion gold nanoparticles are often stabilized with charged ligands, like citrate,[132,133,134] cetrimonium bromide (CTAB),[135,136] or amino acids like L-Lysine.[137,138] The charged ligands and their respective double layer lead to a repulsive interaction between the nanoparticles and thus an electrostatic stabilization of the colloidal system.[139] Gold nanoparticles in non-aqueous dispersion can be sterically stabilized by using polymers,[140] e.g. polystyrene (PS),[141] poly(dimethylsiloxane) (PDMS),[142] or N,N-dihexylcarbodiimide [143] as ligands. Also, small molecules, such as oleylamine,[144] or alkanethiols can be used to stabilize small gold nanoparticles in organic solvents.[145]

Gold nanoparticles capped with alkanethiols show a temperature-dependent agglomeration behavior. By cooling the dispersion below a certain temperature (agglomeration temperature), the particles start to agglomerate. By reheating the sample above the agglomeration temperature, the particles will deagglomerate and can be redispersed. The agglomeration temperature of the dispersion is influenced by the diameter of the core gold nanoparticles[94] and the ligand length of the alkanethiol.[95] If the temperature is kept constant, the start point of agglomeration depends on the particle concentration. As soon as a critical

particle concentration is exceeded, the system will start to agglomerate. Notably, it was found that this concentration is significantly affected by the solvent used to disperse the nanoparticles.[97] Furthermore, the used solvent has an impact on the geometry of the formed agglomerates.[146] The precise agglomeration temperature of alkanethiol-capped gold nanoparticles can easily be measured by using different techniques, like small angle X-ray scattering (SAXS) or dynamic light scattering (DLS), see **Chapter 2.2** and **Chapter 2.3**.

2.2   X-Ray Analysis of nanoparticle agglomeration

SAXS (small angle X-ray scattering) is a powerful tool to resolve structures on a nanometer length scale,[147] investigate colloidal systems,[148,149,150,151] and biological macromolecules.[152,153,154,155] It can be employed to determine the size, the size distribution, the shape and the surface structure of nanoparticles.[156,157] SAXS measurements can also be used to follow the formation process of nanoparticles,[157,158,159] or their self-assembly.[160,161,162] SAXS measurements are a well-established method to follow the temperature induced agglomeration process of nanoparticles.[94,95,163]

The agglomeration temperature of nanoparticles can be determined as follows. The recorded scattering intensity $I(q)$ depends on the modulus q of scattering vector $\vec{q}$ and consists of the scattering of the particles I_{Par}, the scattering of the solvent I_{Sol} and the background scattering I_B adding up incoherently, see **Equation (1)**.[156] It is worth noticing that the scattering contrast between the ligand hexadecanethiol and the tetradecane is so small, that the solvent and the ligand shell cannot be distinguished.[164] Consequently, only the gold core of the particle is taken into consideration. The contribution of the solvent scattering and the background scattering are generally measured simultaneously. By preparing the sample and the solvent identically and measuring them both under identical conditions, the contribution of the background scattering is already taken into account by the measurement of the solvent, simplifying **Equation (1)** to **Equation (2)**. A background correction of the scattered data of the particles can be performed by subtracting the recorded scattering data of the solvent from the scattering data of the sample.

$$I(q) = I_{Par}(q) + I_{Sol}(q) + I_B(q) \tag{1}$$

$$I(q) = I_{Par}(q) + I_{Sol,B}(q) \tag{2}$$

During the agglomeration process dispersed particles and agglomerated particles are observed simultaneously in the sample. Consequently, the scattering of the particles can be described as the summation of the scattering intensity of the dispersed particles I_{Dis} and the agglomerated particles I_{Agglo}, see **Equation (3)**.[165] The scattering intensity of nanoparticles depends on the number of scattering particles N, the scattering volume V, the difference in scattering length densities $\Delta\rho_S$, the form factor $F(q)$ and the structure factor $S(q)$. For randomly distributed particles in dispersion, the contribution of the structure factor can be neglected and only the form factor is considered, see **Equation (4)**.[156] The form factor describes the size and the shape of the individual particle, whereas the structure factor contains information about the relative position of the particles.[156] For spherical particles the form factor $F(q)$ can be described by using the core radius of the single particle r_{Core}, see **Equation (5)**.[156,166] To consider polydispersity of the particles $p(r)$, the average radius of the particles r_{Avg} and its deviation σ is estimated using the Schulz-Zimm distribution, see **Equation (6)**. To take the polydispersity of the particles into consideration, the form factor will be averaged over the individual particles, see **Equation (7)**.

$$I_{Par}(q) = I_{Dis}(q) + I_{Agglo}(q) \tag{3}$$

$$I_{Dis}(q) = \frac{N_{Dis}}{V} \cdot \Delta\rho_S^2 \cdot \langle F(q)^2 \rangle \tag{4}$$

$$F(q) = 4 \cdot \pi \cdot r_{Core}^3 \, 3 \, \frac{\sin(q \cdot r_{Core}) - q \cdot r \cdot \cos(q \cdot r_{Core})}{q^3 \cdot r_{Core}^3} \tag{5}$$

$$p(r_{Core}) = \frac{1}{\sigma^2}^{\frac{1}{\sigma^2}} \left(\frac{r_{Core}}{r_{Avg}}\right)^{\frac{1}{\sigma^2}-1} \frac{e^{-\frac{r_{Core}}{\sigma^2 \cdot r_{Avg}}}}{r_{Avg} \Gamma\left(\frac{1}{\sigma^2}\right)} \tag{6}$$

$$\langle F(q, r_{Avg})^2 \rangle = \int_0^\infty F(q, r_{Core})^2 \cdot p(r_{Core}) \, dr_{Core} \tag{7}$$

For the agglomerated particles the structure factor needs to be considered in addition to the form factor. During the agglomeration of gold nanoparticles, the particles arrange themselves irregularly. The structure factor $S(q)$ can be described by using a combination of the hard-

sphere model and a power law, see **Equation (8)**.[167,168] With the hard-sphere volume fraction η_V, the hard sphere radius r_{HS}, the periodic function G, a pre-factor c and the power-law exponent v.

$$S(q) = S_{HS}(q) + c \cdot q^{-v} = \frac{1}{1 + 24 \cdot \eta_V \dfrac{G(q, 2r_{HS})}{4 \cdot q \cdot r_{HS}}} + C \cdot q^{-v} \tag{8}$$

Considering the structure factor of the agglomerated particles, their scattered intensity can be described according to **Equation (9)**.

$$I_{Agglo}(q) = \frac{N_{Agglo}}{V} \Delta\rho_S^2 \cdot \langle F(q)^2 \rangle \cdot S(q) \tag{9}$$

The determined scattering intensity $I(q)$ of an agglomerating sample containing fully dispersed and agglomerated particles can therefore be expressed considering the different scattering contributions, see **Equation (10)**.

$$I(q) = I_{Dis} + I_{Agglo} + I_{Sol,B} \tag{10}$$

To be able to determine the agglomeration temperature of gold nanoparticles by SAXS measurements, the sample was heated to ensure that particles were completely dispersed and then cooled down to initiate particle agglomeration. Finally, the agglomerated particles were heated to redisperse them. Additionally, the scattering data of the pure solvent was recorded. It is assumed, that the scattering of the solvent does not change by changing the temperature. The recorded scattering of the solvent is then subtracted from the scattering data of the gold nanoparticles at different temperatures, simplifying **Equation (10)** to **Equation (11)**. By using **Equation (4)** and **(9)**, **Equation (11)** can be described as **Equation (12)** or **Equation (13)**.

$$I(q) = I_{Dis} + I_{Agglo} \tag{11}$$

$$I(q) = \frac{N_{Dis}}{V} \cdot \Delta\rho_S^2 \cdot \langle F(q)^2 \rangle + \frac{N_{Agglo}}{V} \cdot \Delta\rho_S^2 \cdot \langle F(q^2) \rangle \cdot S(q) \tag{12}$$

$$I(q) = \frac{\Delta\rho_S^2}{V} \langle F(q)^2 \rangle [N_{Dis} + N_{Agglo} \cdot S(q)] \tag{13}$$

The scattering volume V and the particle numbers N can be described as the volume concentrations ϕ, see **Equation (14)** and **(15)**.

$$\phi_{Dis} = \frac{N_{Dis}}{V} \tag{14}$$

$$\phi_{Agglo} = \frac{N_{Agglo}}{V} \tag{15}$$

The ratio of particles which are part of an agglomerate is described using the agglomeration fraction χ_{Agglo}, see **Equation (16)**.

$$\chi_{Agglo} = \frac{\phi_{Agglo}}{\phi_{Dis} + \phi_{Agglo}} \tag{16}$$

By fitting the recorded SAXS data, the agglomeration fraction of the particles can be determined at different temperatures, to show the temperature at which the agglomeration of the particles has started. The data analysis is shown for hexadecanethiol-capped gold nanoparticles in tetradecane. The sample was heated to 80 °C and cooled to 10 °C. Measurements were recorded every 5 K. Selected measurements and the corresponding fits are shown in **Figure 1**.
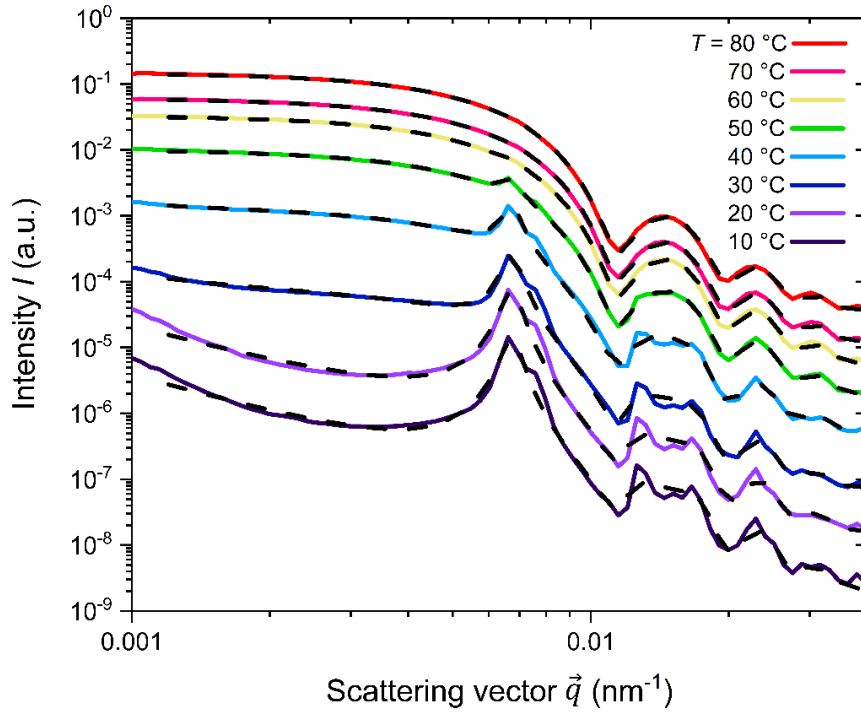
Figure 1: Selected SAXS data (colored, solid lines) and corresponding fits (black, dashed lines) of hexadecanethiol gold nanoparticles in tetradecane. The particles had a core diameter of 7.8 nm (± 0.5 nm) and a hydrodynamic diameter of d_H = 13 nm (± 1 nm). The particles were heated to 80 °C and cooled down to 10 °C.

First, the scattering data of the dispersed nanoparticles are fitted. Due to the uniform size and shape of the used gold nanoparticles, the Schulz-Zimm distribution is used to describe the data.[169] Additionally, the scattering data of the dispersed particles can be described according to **Equation (4)**. By applying the volume concentration, **Equation (4)** can be expressed as **Equation (17)**.

$$I_{Dis}(q) = \phi_{Dis} \cdot \Delta\rho_S^2 \cdot \langle F(q)^2 \rangle \tag{17}$$

The polydisperse spherical form factor can be used to determine the core radius r_{Core} of the particles and the polydispersity, see **Equation (7)**. The radius of particles affects the q-position of the minimum of the scattering data and the polydispersity describes how narrow the minimum is. The volume concentration ϕ_{Dis} and the difference in the scattering length densities $\Delta\rho_S$ cannot be fitted independently, but the difference in the scattering length densities can be calculated theoretically by using the different densities of the particles and the solvent (see National Institute for Standards and Technology – Center for Neutron Research)[170], see **Equation (18)**. The scattering length densities are temperature independent

for the applied temperature range and therefore constant. Three parameters remain which can be fitted independently: the volume concentration, the radius of the particles and the polydispersity.

$$\Delta\rho = \rho_{Gold} - \rho_{Tetradecane} \tag{18}$$

$$\Delta\rho = 124.7 \cdot 10^{-6}\,\text{Å}^{-2} - 7.5 \cdot 10^{-6}\,\text{Å}^{-2} = 117.2 \cdot 10^{-6}\,\text{Å}^{-2}$$

When all particles are agglomerated at a lower temperature, not only the form factor but also the structure factor needs to be considered, see **Equation (9)**. By using the volume concentration **Equation (9)** can be described as **Equation (19)**.

$$I_{Agglo}(q) = \phi_{Agglo} \cdot \Delta\rho^2 \cdot \langle F(q)^2 \rangle \cdot S(q) \tag{19}$$

The structure factor can be described according to **Equation (8)**.

$$S(q) = S_{HS}(q) + c \cdot q^{-v} = \frac{1}{1 + 24 \cdot \eta_V \dfrac{G(q, 2r_{HS})}{4 \cdot q \cdot r_{HS}}} + C \cdot q^{-v_F} \tag{8}$$

The hard-sphere radius r_{HS} describes the q-position of the structure peak, whereas the hard-sphere volume fraction η_V describes the width and height of the peak. The fractal exponent v_F is described by the slope at low q-ranges, next to the structure peak. The constant c is a pre-factor which scales the intensity of the scattered data with respect to the structure peak. During the agglomeration process, the size and shape of the dispersed particles, $\Delta\rho_S$ and $\langle F(q)^2 \rangle$ stay constant. Furthermore, the parameters for the structure factors can be fitted. At a high temperature all the particles are dispersed, and the form factor can be fitted. At a low temperature, all the particles are agglomerated and by using the form factor the structure factor can be fitted. To analyze the scattering data at the temperatures at which the agglomerated and dispersed particles exist simultaneously, only the parameters ϕ_{Dis}, ϕ_{Agglo}, and c are fitted. Finally, the agglomeration fraction χ_{Agglo} can be calculated according to **Equation (16)**, for each temperature at which scattering data are recorded. The agglomeration temperature is then defined as the temperature at which $\chi_{Agglo} = 0.2$.[94]

$$\chi_{Agglo} = \frac{\phi_{Agglo}}{\phi_{Dis} + \phi_{Agglo}} \tag{16}$$

2.3   Dynamic light scattering

Dynamic light scattering (DLS, also known as photon correlation spectroscopy) is a common method to investigate the dynamics of colloidal systems such as nanoparticles,[171,172] polymers,[173,174] viruses,[175] macromolecules and proteins.[175,176] DLS is a useful tool to determine the size of particles in colloidal systems and to obtain information about their agglomeration process.[175] DLS is a non-invasive method, only requiring small sample volumes, and is applicable over a broad range of concentrations, temperatures and solvents as long as the sample is transparent.[175]

An instrumental DLS set-up consists of a laser as a light source (typically a laser with a wavelength of a several hundred nanometers),[169] a measurement cell (mostly a cuvette), a photo-multiplier detector and a correlator.[177] Often different optical components, such as lenses or an attenuator are added to focus or to control the intensity of the laser or the scattered light.[178,72] The volume of the intersection between the incident laser beam and the detected scattered light is called measurement volume. A systematic overview of a DSL set-up is shown in **Figure 2**. A pseudo cross correlation arrangement is used, thereby the scattered light is collected by one glass fiber and split into two more or less equal contributions, before transmitting the collected light to the two used photo multiplier detectors. Two signals are generated independently by the two detectors, and subsequently cross correlated before the autocorrelation functions are generated.
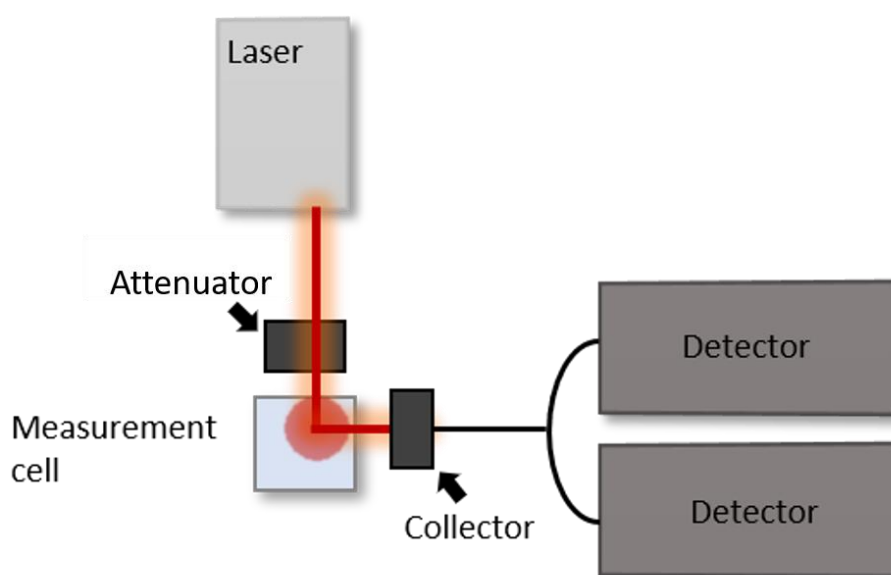
Figure 2: Schematic overview of a dynamic light scattering (DLS) set-up, modified from Sourav Bhattacharjee "DLS and zeta potential – What they are and what they are not?".[171]

The scattering of light by a colloidal suspension was first described by John Tyndall in 1868 and thus became known as the Tyndall-effect.[179] He characterized particles larger than the incident light beam, reporting one of the first dynamic light scattering experiments.[180] In 1871, John William Strutt, third Lord Rayleigh, described the scattering of light on particles that are smaller than the wavelength of the incident light beam, reporting the "Rayleigh scattering" and explaining the blue color of the sky.[181,182] Soon it was discovered by Strutt that not only the particles influence the light scattering, but also the refractive index of the medium.[183,184] In 1908 Gustav Mie investigated the scattering of particles that are larger compared to the wavelength of the incident light beam and considered the refractive index of the particles and the medium.[185] Seven years later, Peter Debye discovered that the scattering of the light can be described independently of the particle properties by using the scattering angle.[186,175,187]

A laser is used to illuminate the sample and the particles inside the sample scatter the incident light evenly in all directions. At a constant scattering angle, the scattering intensity contains information about the size, the shape and the concentration of the particles.[175,175] Considering a non-interacting colloidal system, the movement of the particles can be described according to the Brownian Motion. The thermal kinetic energy of the particles results in the change of the relative position of the particles, creating density and concentration fluctuations.[175,188] The movement of the particles results in variations of the refractive index and therefore fluctuations of the intensity of the scattered light produce random fluctuations of dark and bright spots in the detector.[63,189] The mean square displacement of the particles is proportional to time.[175] These stochastic fluctuations can be summarized as autocorrelation functions of the intensity of the scattered light and depend on the diffusion time of the particles.[64,72,190] Larger particles move more slowly than smaller particles, resulting in smaller changes of the positions.[175] For well-dispersed, single particles and macromolecules, the obtained correlation time directly depends on the diffusion coefficient.[64,176]

The Einstein-Smoluchowski theory describes the relation between the diffusion coefficient D_{Diff} and the particle mobility μ, showing that the diffusion coefficient is inversely proportional to particle size, indicating that larger particles move slower than smaller ones, see **Equation (20)**.[191,192] Additionally, the diffusion coefficient depends on the temperature and the Boltzmann constant.

$$D_{Diff} = \mu \cdot T \cdot k_B \qquad \textbf{(20)}$$

The particle mobility μ can be expressed by using the friction constant of the particle in the solvent β, see **Equation (21)**.[193,194]

$$D_{Diff} = \frac{T \cdot k_B}{\beta} \tag{21}$$

Considering Stokes findings about the movements of spherical particles in a medium, the friction constant β can be described using the hydrodynamic radius of the particles r_H and the solvent viscosity η, see **Equation (22)**.[193]

$$\beta = 6 \cdot \pi \cdot r_H \cdot \eta \tag{22}$$

By applying **Equation (22),** the Einstein-Smoluchwoski theory can be evolved to the Stoke-Einstein relation to determine the hydrodynamic radius of the particles r_H, see **Equation (23)**.[72,193,188]

$$r_H = \frac{k_B \cdot T}{6 \cdot \pi \cdot \eta \cdot D_{Diff}} \tag{23}$$

To be able to make valid interpretations of the recorded DLS data, knowledge of the precise temperature during the measurements is indispensable, regarding the direct influence on the particle mobility and the indirect influence on the refractive index and the viscosity of the solvent.[175]

To be able to detect the fast light fluctuations, the photo detectors need to have a fast response, a minimal dead time and a high sensitivity. The response depends on the ratio of the detector area and the coherence area of the observed particles. The coherence area of the particles A_{coh} depends on the wavelength of the incident beam λ, the radius of the scattering volume r, the distance of the scattering particle and the detector Δx, see **Equation (24)**:[63]

$$A_{coh} = \frac{\lambda^2 \cdot (\Delta x)^2}{\pi \cdot r^2} \tag{24}$$

The resolution of the measurement depends on the ratio of the aperture area of the detector and the coherence area. Consequently, the resolution can be improved by minimizing the detector area using pinholes in front of the detector.[63] Formerly used lenses and pinholes to

collect the light are mostly replaced with optical fibers by now, because they require less alignment and allow for cheaper and more flexible designs of the optical components.[178]

The intensity of the scattered light depends on the scattering angle, the observation time,[63] the difference of the refractive indices of the particles and the medium of the colloidal system,[169] and on the concentration of the particles. A high particle concentration may not only disturb light scattering measurement, because of unwanted particle-particle interactions, but also multiple scattering can occur. This means the initial light beam is scattered on a first particle and subsequently the scattered light is scattered by a second particle before it is detected affecting the recorded autocorrelation functions.[187] To avoid the detection of multiple scatterings, we use a pseudo cross correlation, a well-established method.[178] If the particle concentration is too low, the detected signal is also low, resulting in a low signal-to-noise-ratio. At a high particle concentration, the free distance between non-interacting particles becomes too small (smaller than 20-40 times the distance of the particle diameter), resulting in either attractive or repulsive electrostatic, steric or van der Waals interaction between the particles, influencing the diffusion coefficients compared to the diffusions coefficient of a single particle.[187] If the particle concentration is so low that the total number of particles observed varies significantly as particles move in and out of the scattering volume, base-errors or a second decay in the autocorrelation function can occur. This second decay is much slower than the decay generated by the Brownian motion of the particles, which implies a smaller diffusion coefficient and makes the determined particle size appear larger than the real particles.[187,63] Interparticle interaction can influence the diffusion coefficient. To avoid these effects, the average number of particles N within the scattering volume should be larger than 1000. Therefore, the particle concentration has to be optimized for DLS experiments. In addition to the particle concentration, the particle size can also be a limitation. If larger particles (typically about a several microns) start to sediment, they undergo a directive movement, influencing the scattering signal and overtime the particle concentration in the scattering volume.[63]

The intensity also depends on the size of the particles. It scales with the power of 6 of the particle diameter (d), larger particles scatter light with a higher intensity than smaller ones and the obtained hydrodynamic diameters are biased towards the size of the larger particles.[63,175] Additionally, the intensity of the scattered light is proportional to the square of the volume of the detected particles, showing the sensitivity of DLS towards the

agglomeration of particles.[63,176] Typically, dynamic light scattering can distinguish particles with hydrodynamic diameters differing at least by a factor of three.[72]

Photodetectors always produce a dark count rate by generating random output pulses, even without any measurements. This dark count rate contributes to the overall autocorrelation function.[195] To guarantee the signal of nanoparticles is high enough to ensure a high signal-to-noise-ratio, typically lasers with a power of at least 100 mW are used.[190] The signal-to-noise-ratio can be further improved by increasing the measurement duration.[195] Additionally, the pseudo cross correlation improves the signal-to-noise-ratio by minimizing afterpulses and dead times of the used photo multiplier detectors.[181]

2.3.1 Analysis of DLS data

DLS is a suitable method to determine the size as well as the size distribution of colloidal systems. DLS can resolve sizes with in a q-range even smaller than $2\pi/r$.[169] The modulus of the scattering vector $\vec{q}$ is given by **Equation (25)** and depends on the wavelength of the incident laser beam λ, the scattering angle θ, and the refractive index n.[63,169]

$$q = |\vec{q}| = \frac{4 \cdot \pi \cdot n}{\lambda} sin \frac{\theta}{2} \qquad \textbf{(25)}$$

The autocorrelation function describes the time dependence of the measured intensity. Usually the intensity fluctuates in the range between ns and µs,[63,175] resolving mean residence times of µs to ms, and thus particle sizes between several nm and µm.[187]

The normalized autocorrelation function $g_2(\tau)$ can be described by comparing the time depended scattering intensity $I(t)$ and the scattering intensity after a delay time τ, see **Equation (26)**. The brackets indicate that the average over the measurement duration is used.[63,175]

$$g_2(\tau) = \frac{\langle I(t) + I(t + \tau)\rangle}{\langle I(t)^2\rangle} \qquad \textbf{(26)}$$

The decay of the autocorrelation function depends on the diffusion coefficient of the scattering particles. A high diffusion coefficient leads to fast fluctuations of the intensity and therefore a faster decay, compared to slower diffusive particles, see **Figure 3**.[63]
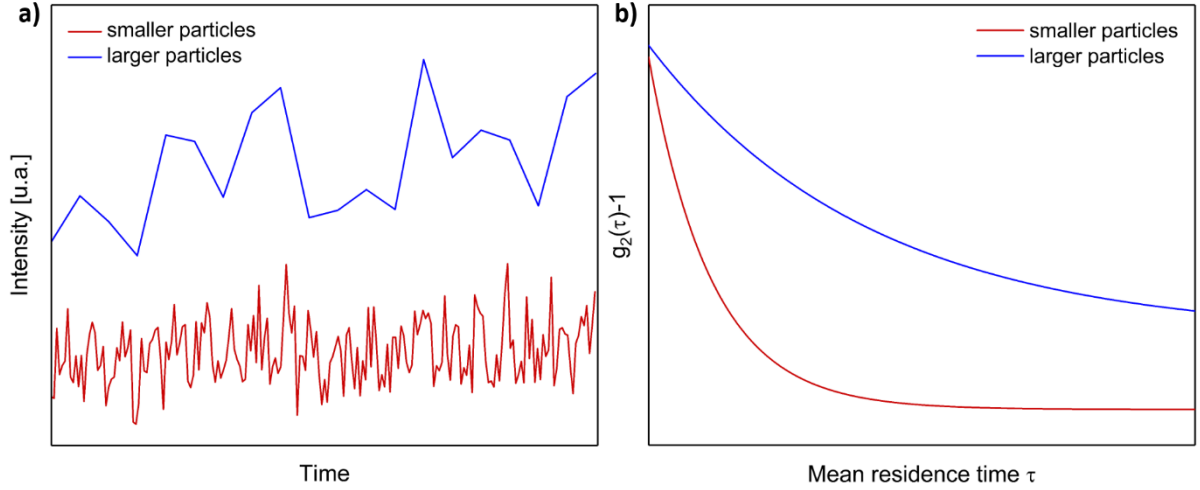
Figure 3: (a) Schematic representation of the intensity fluctuations over time of smaller and larger particles and (b) the corresponding autocorrelation functions over the mean residence time of smaller and larger particles, inspired from Puthusserickal A. Hassan *et al* "Making Sense of Brownian Motion: Colloid Characterization by Dynamic Light Scattering".[63]

Assuming a Gaussian distribution of the intensity fluctuations, the autocorrelation function and the correlation function of the electric field $g_1(\tau)$ can be described according to **Equation (27)**.[63]

$$g_1(\tau) = [g_2(\tau) - 1]^{0.5} \tag{27}$$

For monodisperse, spherical particles undergoing only Brownian diffusion, the autocorrelation function can be described as exponential functions, see **Equation (28)**.[63]

$$g_1(\tau) = A \cdot e^{-D_{Diff} q^2 \tau_{Diff}} + B \tag{28}$$

A describes the amplitude and *B* the baseline of the correlation function. The decay of the function depends on the diffusion coefficient D_{Diff}, the scattering vector $\vec{q}$ and the mean residence time τ_{Diff} of the particles. A narrow size distribution of the particles leads to an almost single exponential decay, whereas for a polydisperse sample the autocorrelation function can be described as a sum of exponentials functions, which are weighted by their amplitudes.[63]

Considering that the scattered intensity depends on the number of particles *N*, the square of the particle mass *m* and the form factor *F(q,R)* of the particles, the diffusion coefficient D_{Diff} can be described according to **Equation (29)**.[63]

$$\overline{D} = \frac{\sum_i N_i m_i^2 P(q,R) D_i}{\sum_i N_i m_i^2 P(q,R)} \tag{29}$$

This shows, that the obtained diffusion coefficient by DLS is weighted by the square of the mass of the particles and therefore biased towards larger sizes compared to other optical techniques like TEM.[63]

In the following chapters, the hydrodynamic radius r_H of the gold nanoparticles will be determined as published previously.[196] Consequently, the recorded DLS data are fitted using an exponential decay, using the decay time τ, the mean residence time τ_{Diff} and the constant C, see **Equation (30)**.[197]

$$g_2 - 1 = A \cdot \exp\left(-\frac{2\tau}{\tau_{Diff}}\right) + C \tag{30}$$

The diffusion coefficient D_{Diff} can then be determined by using the scattering vector $\vec{q}$ see **Equation (25)** and the mean residence time τ_{Diff}, see **Equation (31)**.[195]

$$D_{Diff} = \frac{1}{q^2 \cdot \tau_{Diff}} \tag{31}$$

The diffusion coefficient D_{Diff} can be used to determine the hydrodynamic radius of the particles r_H, using the Stoke-Einstein relation, see **Equation (32)**.[188] The hydrodynamic radius also depends on the dynamic viscosity of the solvent η, and the temperature of the sample T.

$$r_H = \frac{k_B \cdot T}{6 \cdot \pi \cdot \eta \cdot D_{Diff}} \tag{32}$$

During the agglomeration process of the gold nanoparticles, the hot sample is cooled down. Consequently, the temperature dependency of the refractive index and the dynamic viscosity of the solvent needs to be considered. In this project, only tetradecane was used as a solvent, and data from literature were used to extrapolate the refractive index and the dynamic viscosity for the temperature range applied,[198,199,200,201] as previously published, see **Figure 4** and **Figure 5**.[196] For the refractive index, a linear correlation,[202] see **Equation (33)**, and for the dynamic viscosity an exponential correlation was found, see **Equation (34)**. The obtained refractive indices and viscosities are used to determine the hydrodynamic diameter of the particles during the cooling of the sample for the corresponding temperatures.

$$n = a + b \cdot T = 1.55739 - 0.00044 \, K^{-1} \cdot T \tag{33}$$

$$\eta = A \cdot \exp\left(\frac{B}{T - T_0}\right) = 2.05 \cdot 10^{-5} Pa \, s \cdot \exp\left(\frac{1085.1 \, K}{T - 64.2 \, K}\right) \tag{34}$$
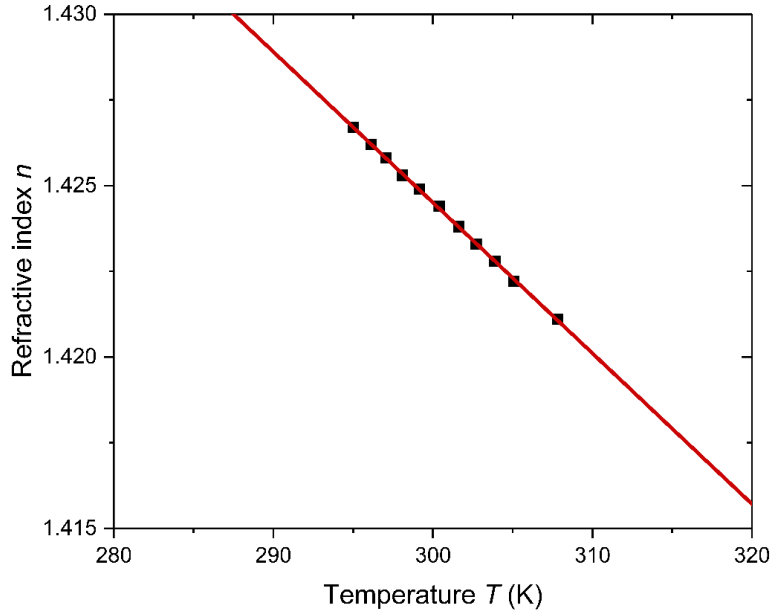
Figure 4: Extrapolated refractive index of tetradecane at different temperatures (red line), reproduced from literature (black dots).[198]
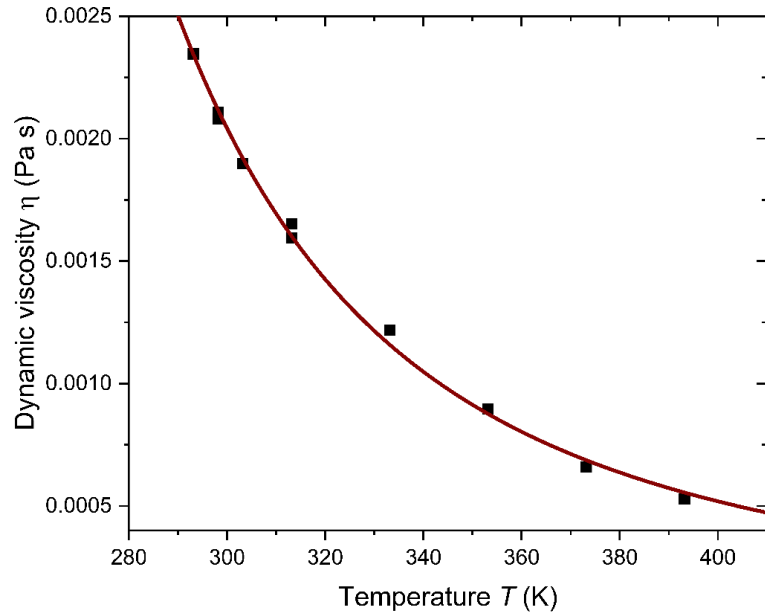
Figure 5: Extrapolated dynamic viscosity of tetradecane at different temperatures (red line), reproduced from literature (black dots).[199,200,201]

Dynamic light scattering measurements are very sensitive to the size of the particles, making DLS a useful tool to follow any changes in the size of the particles.[203] Consequently, early stages of the agglomeration process can be followed, however, as soon as the agglomerates become larger and start to sediment, conventional DLS measurements reach their limits. As discussed earlier, DLS measurements are based on the Brownian motion of the particles. By adding additional convective flows, such as thermal convection or sedimentation, particles move faster than what is expected from Brownian motion alone, resulting in an underestimation of the particle size.[204] By performing experiments in microgravity, changing particle dynamics can be observed and analyzed by DLS measurements, without the disturbing influence of convective flows.[78,205]

2.4 Microgravity

On the Earth's surface the gravitational acceleration is defined as 1 g (9.81 m s^{-2}). The term microgravity describes an environment in which objects experience a reduced gravitational acceleration compared to the gravity on the Earth's surface. The prefix "micro" indicates that the gravitational acceleration is only one millionth of the gravity on the Earth's surface (10^{-6} g).[206,207] However, the term is generally used to describe an environment with reduced gravitational acceleration, in which objects experience weightlessness.[208,209] The use of the term microgravity should emphasize that even when objects are weightlessness, the gravitational acceleration is never zero.[209] Microgravity does not only influence the weight of objects, but also provides a convection- and sedimentation-free environment.[210] Performing experiments under microgravity conditions offers the unique possibility to study various fundamental processes in the absence of gravity, and thus investigate its influence. On Earth, options to realize microgravity conditions suitable for performing experiments are rather limited. In drop towers,[61] and during parabolic flights sufficient microgravity conditions can be available. Another option are space experiments that can be performed during space shuttle missions or on space stations, like the ISS (International Space Station).[211] Sounding rockets can be considered as an option in between Earth and space, which have been successfully employed for investigation under microgravity conditions.[212]

For initial experiments, drop towers appeared to be the most accessible and affordable option. They provide the possibility to realize excellent microgravity conditions up to

10^{-5} - 10^{-6} g by utilizing a free fall in vacuum. However, depending on the height of the drop tower, these free falls only have a duration of a few seconds.[213] The free fall duration can be calculated using Newton's law, see **Equation (35)**.[214]

$$x = x_0 + v_0 \cdot t + \frac{1}{2} a \cdot t^2 \tag{35}$$

Where x is the distance the object travelled, x_0 is the initial height, v_0 is the initial velocity, a is the acceleration of the object, and the time of the free fall t.

In a drop tower the acceleration a is the Earth's acceleration (1 g), the initial velocity is zero, and the difference of the distance x the object travelled and the initial distance x_0 can be expressed as the height of the free fall tube h, resulting in the free fall time t as following, see **Equation (36)**.[214]

$$t = \sqrt{\frac{2 \cdot h}{1g}} \tag{36}$$

Worldwide there are several drop towers providing microgravity conditions for under 2 s.[213] The Beijing Drop Tower at the National Microgravity Laboratory in China has a free fall zone of 60 m, providing microgravity conditions for 3.5 s.[215] The Drop Tower in the Zero Gravity Research Facility at the NASA Glenn Research Center in Cleveland, USA, is the highest drop tower built in the US, with a free fall tube height of 155 m, providing microgravity conditions for 5.18 s.[216,217] The Drop Tower in Bremen, Germany, has a tube height of 146 m and provides microgravity conditions for a free fall of 4.7 s.[216] Additionally, in Bremen there is the possibility to use their unique catapult system to extend the microgravity duration to 9.3 s.[213] As can be seen from **Equation (36)**, if the height of the tube is doubled, the microgravity duration is only increased by the factor $\sqrt{2}$. However, if a catapult system is used, the drop capsule describes a parabolic flight patch, leading to a doubled microgravity duration compared to a free fall.[214]

Parabolic flights are a second option to access microgravity conditions. The parabolic flight maneuver starts with a steady, horizontal flight. This is followed by a climb flight of the aircraft at 45 ° for approximately 20-25 s and the aircraft accelerating with approximately 1.8 g. Subsequently, the acceleration of the airplane is stopped rapidly by strongly decreasing the thrust of the engines. When the acceleration of the aircraft decreases, the microgravity phase is entered. The microgravity phase lasts between 20-25 s, while the aircraft undergoes a dive

at an angle of 45 ° and an acceleration of 1.8 g. The aircraft transitions into a steady horizontal flight again. Now the parabolic flight maneuvers can start over again resulting in the possibility to experience microgravity phases of 20-25 s between 30-60 times, with an interval of 40 s between. It is worth mentioning, that the microgravity phase starts with the decreasing acceleration of the aircraft, not with its downwards movement, see **Figure 6**.[214,218]
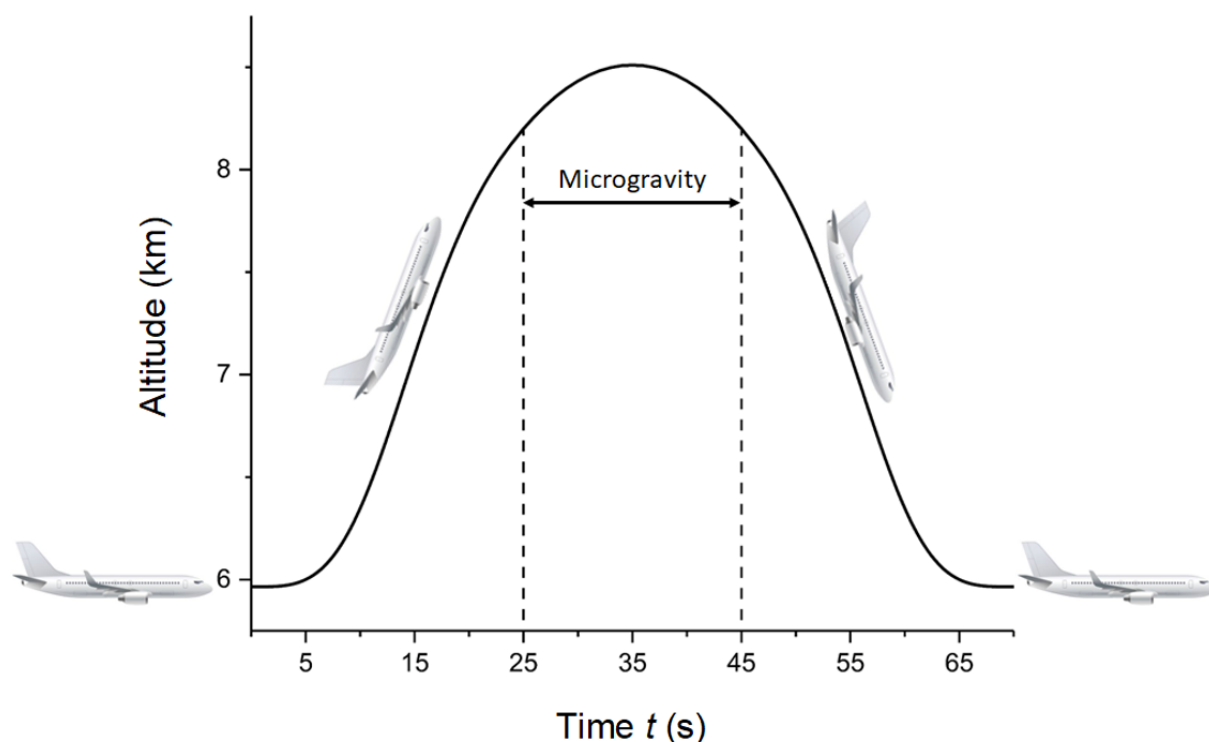
Figure 6: Schematic overview of the flight maneuver of a parabolic flight, inspired by D. Beysens and J. Van Loon "Generation and Applications of Extra-Terrestrial Environments on Earth".[214]

Parabolic flights offer the unique possibility to allow the scientists to perform their experiments by themselves. Additionally, parabolic flights allow the access to various different g-levels, through different pull up and down maneuvers. Microgravity conditions up to 10^{-3} g can be achieved only for 5 - 10 s.[214] Experiments performed during parabolic flights are exposed to the aircraft pitch rotation of average 3 °/s [218] and complex vibration pattern of the aircraft.[219] These effects can alter the experiments and need to be kept in mind.

The launch of a sounding rocket allows for microgravity conditions for several minutes.[220] Various rockets offer different possibilities regarding payloads and microgravity durations. For example, the European TEXUS/MAXUS program offers the possibility of scientific payloads

between 100 kg and 500 kg, and a payload diameter of 480 mm or 640 mm. Microgravity durations between 230 s and 730 s are accessible. The rockets are reaching heights between 140 km and 750 km.[221] TEXUS and MAXUS rockets experience a peak acceleration between 10 - 13 g, whereas the MiniTEXUS rocket reaches a peak acceleration up to 21 g.[222]

Even longer microgravity durations can only be realized in space. For example the International Space Station (ISS) allows the performance of experiments under microgravity conditions for months or even longer.[223] Experiments are either performed fully automated or with the help of trained astronauts. It has to be kept in mind, that depending on the operating onboard systems and different crew activities, the microgravity conditions can differ from 0.01 g to 10^{-6} g.[224]

2.4.1 Experiments in microgravity

Performing experiments in microgravity and comparing them with the corresponding experiments performed on ground under normal gravity conditions (1 g) was proven to considerably improve understanding of physical and chemical processes. Especially the crystallization of inorganic materials,[16,225] semiconductors, proteins,[226,227,228] and macromolecules [229] is strongly affected by gravity. Also the investigation of biological samples,[13,230,231] or colloidal system offered insights in their different growth mechanism and the influence of gravity on these systems.[75,232,205,233]

2.4.1.1 Effects of microgravity on crystallization

Crystallization has been a subject of fascination for scientists for many centuries,[234,235,236] and is still attracting the scientific community today.[237,238,239] While initially considered a laboratory curiosity, indeed the growth of crystals has ever been a useful tool in science for several reasons,[240] it is an efficient method to isolate molecules from mixtures of several products. Furthermore, it can be employed to effectively purify products by isolating them in a single crystalline form.[240] Today, an important factor is structural elucidation of complex molecules. X-ray diffraction can be addressed to characterize structures otherwise difficult to analyze, e.g. macromolecules.[241] Besides classical chemists and materials scientist, early on especially biochemists and molecular biologists [242,243] were attracted by the chance to perform

detailed structure analysis of proteins,[244,245] or enzymes.[246,247] Furthermore, today still numerous industrial processes rely on crystallization, e.g. crystals of inorganic or organometallic salts are the basis for non-linear optics[248] or optical-electronic devices.[249]

In general, all crystallization processes proceed in two steps, initial nucleation followed by the growth of the crystal.[240,250] Nucleation is the more complex part to be adressed,[240] both experimentally and theoretically and many approaches have been reported during the last years to understand and describe the mechanism.[251,252,253]

First, the so-called classical nucleation theory was developed. In supersaturated solutions, metastable dense liquid clusters arise as intermediate states prior to crystal formation.[250,254] Later on, non-classical nucleation mechanisms were developed, suggesting a two-step mechanism via the formation of stable dense liquid phases, so called pre-nucleation clusters.[250]

Consensus prevails that besides this initial nucleation (primary nucleation), so called secondary nucleation can occur: Nucleation processes in a solution already containing growing crystals. The mechanism can be to some degree considered inverse to nucleation. Partially solvated clusters are removed from the crystal surface by buoyancy fluid-driven flows and act as source of nucleation.[207] Generally, high nucleation rates result in the formation of a large number of crystals with smaller size. Lower nucleation rates, however, favor fewer and larger crystals. Consequently, the nucleation process plays an important role for characteristics of the final crystals, such as number, size, quality or polymorphism.[250]

The mechanism for crystal growth after initial nucleation is more straightforward and well understood.[240] During the growth phase of the crystallization process, ions, atoms or molecules from the solution are incorporated into the crystal. Important to understand mass transport in the course of crystal growth is the concept of the depletion zone.[207] As soon as molecules start diffusing from the solution surrounding the crystal to add to it, a solution depleted in the corresponding molecule is formed around the crystal. This solution is significantly lower in density than the surrounding supersaturated bulk solvent. This concentration gradient is compensated by convection since the depleted solution is lower in density and will rise up.[207] In case the difference in density between the crystal and the solution is sufficiently large, the crystal will start to sediment after formation. Also, the

sedimentation process is preventing the crystal from remaining in the depleted zone, as it will sink into the supersaturated bulk solution.[207]

Performing crystallization experiments in microgravity severely attenuates bouncy driven convection and sedimentation, and thus the crystal is only subject to Brownian motion.[207] While no effect of microgravity conditions on primary nucleation is observed, secondary nucleation is basically suppressed. The before mentioned removal of clusters from the crystal surface, which initiated secondary nucleation, is driven by fluid flows, which do not existent in the absence of gravity. Hindered secondary nucleation results in reduced number of crystals and thus an increased crystal size. Also, the crystal growth is significantly affected by microgravity. Since neither convection nor sedimentation can occur, the crystal remains stable in a depleted zone, only showing slight supersaturation.[207] A lower supersaturation during crystal growth is postulated to result in larger crystals and provide better-order crystal lattices.[255] [207] Furthermore, it allows the dissociation and a reorganization of crystal party, decreasing the number of defects. The absence of gravity also hinders the sedimentation of the formed crystals, further contributing to a constant and uniform crystallization environment.[207]

Indeed it was reported that crystals formed in microgravity tend to have fewer cracks, striations, inclusion and defects and therefore a higher quality than crystals obtained under normal conditions.[18,19,21,22] The increased crystal quality might be the result of a more uniform environment at the crystal interface during the crystal growth due to elimination of convection.[226] It was shown, that crystallization in microgravity can increase the size and the quality of crystals and even lead to the crystallization of samples not forming crystals on ground. For example, Smith *et al.* investigated the formation of insulin crystals on three space shuttle flights. Larger crystals with a higher crystal resolution were found, meaning an increased distance between the crystal lattice planes and therefore showing a more ordered structure.[227] Additionally, the formation of larger crystals, displaying more uniform morphologies and an increased crystal quality of γ-interferon D^1, porcine elastase, and isocitrate lyase were observed on the U.S. space shuttle flight STS-26.[226] Littke and John found larger β-galactosidase and lysozyme on the space shuttle mission Spacelab 1 than on ground.[228]

2.4.1.2 Effects of microgravity on colloidal systems

While plenty of research has been published on microgravity investigations of the crystallization from molecular precursors, less is reported on colloidal systems in general.[256] According to Yamanaka *et al.*, "the effect of gravity on colloidal crystallization was still controversial" (*Int. J. Microgravity Sci. Appl.* 35, p.1, **2018**).[256] Weitz *et al.* define colloidal systems very general as "fluids with other particles dispersed in them, particularly particles of size between one nanometer and one micrometer" (in *53rd International Astronautical Congress No. IAC–02*, p.2, **2002**).[77] The colloids can vary distinctly in various parameters such as size, shape, surface charge and charge distribution.[77] This diversity in structure combined with its tunability leads to widespread applications in industrial processes, in material science [257] and pharmaceuticals.[258] The difference to pure atomic system from solution crystallization was described by Chaikin *et al.* Crystallization is triggered by a defined volume rather than osmotic pressure. Furthermore, the ability to exchange energy and momentum with the solvent together with a low number of particles per volume, lead to a lower dependency on temperature.[229] For charged colloidal particles, phase transitions from a disordered fluid state to a more ordered crystal state, due to increased electrostatic particle interaction, have been reported.[256,259] Dynamics of atoms or molecules are generally more rapid compared to colloidal systems.[256]

Weitz *et al.* studied multiple colloidal systems in the course of the Physics of Colloids in Space (PCS) experiment, accommodated on the ISS within overall 2400 hours operations in orbit.[77] A sophisticated analytical set-up to perform various static and dynamic light scattering experiments was applied and remotely controlled. Four colloid classes were investigated during those experiments and compared with results under terrestrial conditions: binary colloidal crystals, colloid-polymer mixtures, disordered fractal structures and colloidal glass samples.[77] Weitz *et al.* concluded that gravity is significantly affecting both, size and morphology of the crystals. Reasons, according to them, are on one hand the shear forces from sedimentation destroying the particle edges, and on the other hand, a changing growth mechanism since sedimentation time of the particles competes with the diffusion time.[77]

Chaikin *et al.* investigated the influence of gravity on the formation of hard spheres. As a model for hard spheres, the crystallization of spherical PMMA (polymethyl methacrylate) particles with a diameter of 600 nm was followed by time-resolved Bragg light scattering. To

match the refractive index of the particles and the solvent, the particles were dispersed in a mixture of cis-decalin and tetralin. Experiments were performed on the Space Shuttle's Microgravity Science Laboratory (MSL-1) and on ground. It was found that the crystals grow larger and faster in microgravity than on earth. According to Chaikin *et al*. sedimentation limits crystallite grows. Furthermore, coarsening processes are affected by sedimentation due to long-range interaction between the crystallites moving through diffusion in the surrounding solvent.[229]

Rogers *et. al* investigated the behavior of hard spheres in microgravity by following the phase transition of dispersed poly(methyl methacrylate) particles with static and dynamic light scattering. These experiments were performed using a compact laser light scattering instrument, developed in cooperation with NASA during the Second United States Microgravity Laboratory space shuttle mission. It was found that crystals grew larger in microgravity than on ground and that one sample only crystallized under microgravity conditions.[232]

Okuba *et al.* followed the formation of colloidal silica particles in microgravity using fast-scanning transmitted-light-intensity, fast dynamic light scattering, and a charge-couple device video camera. The experiments were performed during parabolic flights with a MU 300 rear-jet aircraft. Silica particles were formed via the polymerization reaction of tetraethyl orthosilicate. Increased induction times and decreased polymerization rate of the reaction were found. A final conclusion on the obtained particle size in microgravity compared to the particles synthesized on ground could not be drawn due to the short microgravity duration of 20 s.[75]

The agglomeration of nickel nanoparticles in the gas phase was documented by Günther *et al*. An inert gas condensation process was established to yield nickel agglomerates in microgravity and on ground. Microgravity conditions were obtained during the European sounding rocket MAXUS 8 mission and a parabolic flight with the European Parabolic Flight aircraft Airbus A300. The agglomerates were investigated ex-situ via Scanning Electron Microscopy (SEM) and Transmission Electron Microscopy (TEM). On ground and under microgravity conditions chain-like agglomerates were found. However, the agglomerates obtained under microgravity conditions tended to grow longer for extended agglomeration times and showed a narrower intra-chain particle size distribution than on ground. In contrast, no chain-like agglomerates

could be found after the agglomeration process during the sounding rocket mission, which was attributed to a different (multi-domain) magnetic structure of the particles by the authors.[225]

Recently, Yamanaka *et al.* reported the clustering of charged colloids in microgravity during parabolic flights [256] as well as in space.[260] Parabolic flights experiments performed in a MU 300 jet aircraft providing a μ g interval of less than 0.03 G for 20 seconds. Colloidal silica particles were studied via time resolved reflection spectroscopy and small- and ultra-small-angle neutron scattering. Generally larger crystals were found in microgravity compared to ground experiments. The authors attribute those findings to a smaller nucleation rate in microgravity and a longer incubation time.[260] In a subsequent study Yamanaka *et al.* conducted a clustering experiment on the ISS investigating PS (polystyrene) and titania particles associating by electrostatic attraction (for both types the respective positively and negatively charged derivatives were mixed). While the PS particles have a rather small relative density (ρ_{rel} = 1.05), the relative density (ρ_{rel} > 3) as well as the refractive index of the titania particles is quite high. A special set-up was developed by Yamanaka and Mata *et al.* to allow the formation of charged clusters and immobilize the final structures into gel cured using ultraviolet UV-light. These hybrid materials were synthesized on the ISS and analyzed on ground by optical microscopy.[260] Even though the relative density of PS particles and its medium are similar, the PS particles grew approximately 50% larger in microgravity than on ground, and featured enhanced structural symmetry. Furthermore, the experiments allowed to study the cluster formation of charged titania particles, which have a high relative density, which usually hinders the formation of macroscopic aggregates on ground due to rapid settling.[260] According to Miki, the study indicates that sedimentation and convection occurring on ground significantly affects the structure formation of colloids, and unperturbed studies "will help us to develop a model which will be used to design photonic materials and better drugs" (*npj Microgravity* 33, 1-6, **2023**).[260]

Agglomeration kinetics of nanoparticles and the effects of microgravity on the corresponding systems have been studied by Veen and Potenza *et al.*[98,205] The authors operated microgravity experiments on the ISS and were able to control remotely from ESA's Spanish User Support and Operations Center in Madrid. For a system of charged stabilized fluorinated latex particles with a radius of 200 nm, the agglomeration process was followed by near field scattering (NFS) on ground and in space. The latex particles were suspended in a critical solvent, namely a

mixture of 3-methylpyridine and D_2O/H_2O, allowing to control aggregation with Critical Casimir Forces (CCF). CCF colloid systems basically show an opposing temperature dependent behavior compared to classic examples since agglomeration is observed above T_{Agglo} and the particles disperse below T_{Agglo}.[261,262] This phenomenon is attributed to increasing attractive interactions between the particles with an increase in temperature due to restricted solvent fluctuation between the particles.[263,264] Veen and Potenza et al. reported experiments inducing agglomeration at T_{Agglo} and $T = T_{Agglo}$ + 0.1, + 0.2, + 0.3 and + 0.4 K, thus successively increasing the attractive strength. Comparing the results of the experiments carried out on ground with µ g, indicated a transition from a reaction-limited mechanism to a purely diffusion-controlled process due to the absence of sedimentation. According to the authors, this was reflected by the measured fractal dimensions D_f, as well as the power law behavior. On the one hand, the fractal dimensions were significantly affected by the change of T_{Agglo} in microgravity: Higher temperatures and thus higher attractive strength led to a decrease of D_f. On ground, the change in the temperature had no influence on D_f, it was constantly close to the highest temperature measurement in µ g. The change in the fractal dimension indicates a diffusion-limited process: The depletion zone around the agglomerates increases with interaction strength between the particles. On the other hand, the growth rate in microgravity follows a power law $1/D_f$ for all temperatures, which is characteristic for a diffusion-limited process. On ground however, only the early stages of aggregation follow the law $1/D_f$. Afterwards, for later stages, a shift to a more exponential form is observed, showing a massive increase in size. The latter phase strongly depends on the temperature and is more pronounced for larger attractive strengths, indicating a reaction-controlled process.[98,205]

Veen and Potenza et al. made use of the experimental set-up described above to investigate the early stages of the formation of agglomerates of weakly attractive particles and to evaluate whether the process is nucleation governed. Strongly attractive colloidal systems aggregate without nucleation, as particles stick the moment they collide. Under terrestrial conditions, the study of the isolated interplay between nucleation and agglomeration is hindered by concurrent sedimentation and convection. The authors demonstrated that formation of weakly attractive structures is indeed still nucleation based. Increasing attractive forces (realized with higher temperatures) successively result in smaller critical radii until direct particle sticking is observed instead of nucleation.[98,205]

3 Results and Discussions

3.1 Instrumental set-up

3.1.1 Drop tower

The results of the following chapter have been published in "Dynamic Light Scattering on Nanoparticles in Microgravity in a Drop Tower" by Pyttlik, Kuttich and Kraus in *Microgravity Science and Technology* in **2022**.[196]

A set-up was developed to investigate the agglomeration process of gold nanoparticles by dynamic light scattering measurements on ground and in microgravity. To realize the measurements under microgravity conditions, a capsule equipped with an analytical set-up to perform DLS measurements was integrated into the drop tower at the ZARM Institute in Bremen. By performing a simple drop from the top of the tower (drop height 146 m), a microgravity duration of 4.7 s could be reached.[99] Additionally, the drop tower offers the unique possibility to perform a catapult launch. Here the capsule is accelerated from the bottom to the top of the tower, providing a microgravity duration of 9.3 s (during a catapult the very end of the drop range is not targeted for safety reasons).[213] Considering an integration time of 1 s to record one measurement with DLS and a delay time of approximately 100 ms between the measurements, a simple drop allowed to record 4 consecutive data sets. Catapult launches provided sufficient time to record 8 measurements. A sketch of the drop tower is shown in **Figure 7**.[265]
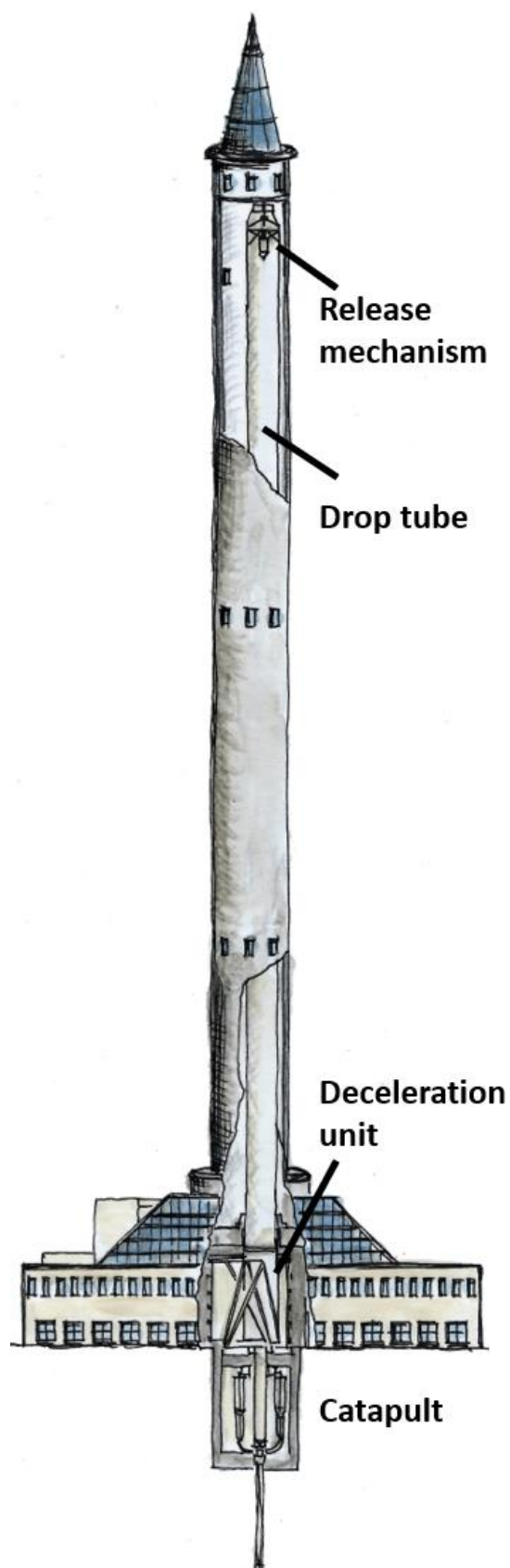

Figure 7: Sketch of the structure of the ZARM drop tower in Bremen was provided by the ZARM Institute in Bremen.[267]

The drop or the catapult launch, respectively, were performed with a drop capsule. All devices required for the measurements had to be integrated inside a drop capsule. The capsule is designed as a cylindrical torso with an inner diameter of 600 mm and two cones as tips. A sketch of a catapult capsule and a platform is shown in **Figure 8**. Inside this cylindrical torso several platforms can be mounted to integrate the experimental set-up. The lowest two platforms are generally occupied with the capsule control system and the power supply.[266,267]
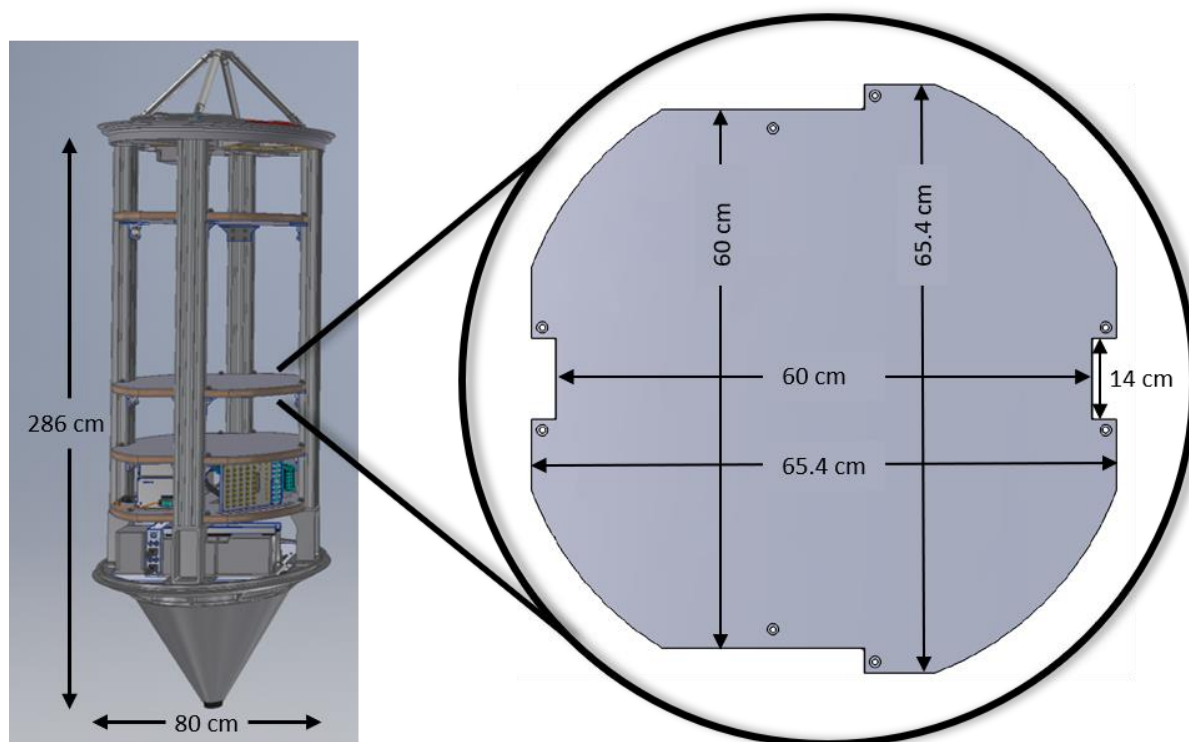
Figure 8: Sketch of the structure of a catapult capsule and the format of platform, modified from the sketch of a catapult capsule and the capsule platform provided by the ZARM Institute.[268]

The experimental set-up was integrated into the drop tower capsule and sealed inside a steel shell, see **Figure 9**, providing a dark environment for the DLS measurements and minimizing the background counts of the photodetectors, improving the signal-to-noise-ratio. To minimize condensation on the measurement cell during the cooling, the capsule was filled with argon. The drop tower capsule was placed either into the catapult system (see **Figure 10**) or lifted to the top of the tower for the drop experiments.
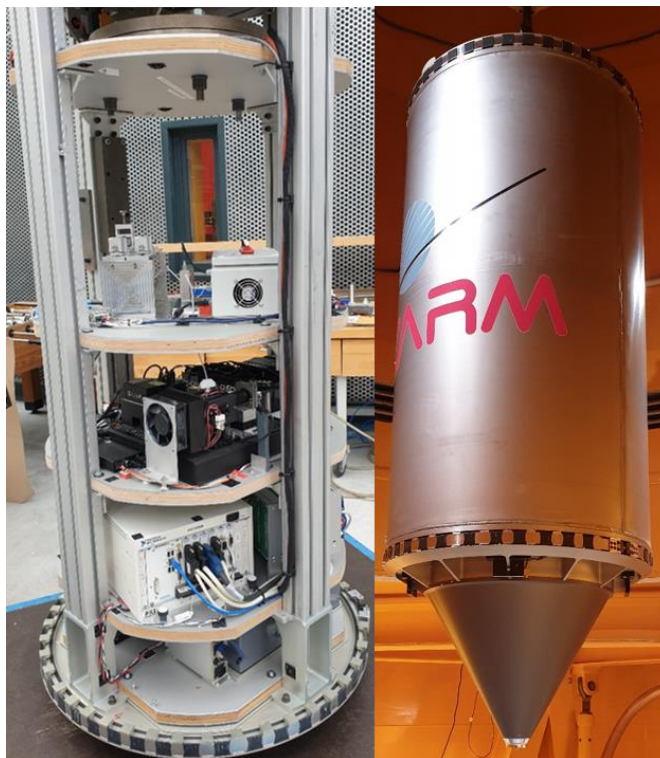
Figure 9: Photograph of the instrumental set-up integrated into the drop tower capsule and the sealed argon filled drop tower capsule. Published in the course of this project in "Dynamic Light Scattering on Nanoparticles in Microgravity in a Drop Tower" by Pyttlik, Kuttich and Kraus in *Microgravity Science and Technology*, in **2022**.[196]

**Figure 10:** Photograph of the sealed drop tower capsule being placed into the catapult system.

3.1.2 Analytical Setup

To follow the agglomeration process in microgravity by DLS measurements, the analytical set-up needed to be integrated into the capsule. To be able to integrate the set-up into the capsule and to successfully perform the experiments, several requirements needed to be met. First, it had to actually fit into the drop tower capsule. All devices had to be sized accordingly to fit into the dimensions described in **Chapter 3.1.1**. Another central requirement to perform reliable DLS measurements with a catapult launch was a very high robustness of the set-up. To ensure reproducibility of reliable measurements, it was desired to perform multiple experiments with the same device. Consequently, it had to withstand vibrations during the flight as well as acceleration forces during the launch and the deceleration impact of the capsule when landing. During the lift-off, the experimental set-up was exposed to 18 g on average for about 280 ms. For the peak even 30 g were expected. Deceleration features an impact of 25 g on average for about 200 ms and a peak of just below 50 g for nearly 11 ms.[266,99] The capsule platforms had a sandwich structure of plywood layered with an aluminum plate on top and at the bottom to provide maximum damping during the acceleration and deceleration of the capsule.[266]

In cooperation with the company LS Instruments AG (Fribourg, Switzerland), a suitable dynamic light scattering (DLS) instrument for these conditions was built during this project. Additional mechanical damping was added as bottom layer to the DLS instrument to prevent any misalignment of the optics during the drop or catapult experiments. Additionally, it had to be considered that the particle system to be analyzed in the drop tower absorbs UV/Vis light. Gold nanoparticles show significant absorption of light between 350 nm and 600 nm (with an absorption maximum of λ_{max} = 526 nm, compare also **Figure 50**). To minimize any unwanted absorption of the incident laser beam by the gold nanoparticles, a laser with a wavelength of 638 nm was used. The scattering of the sample was recorded at an angle of 90 °. As a measurement cell, a 46 mm tall quartz glass cuvette with a square cross-section, an outer side length of 12.5 mm, an inner length of 10 mm and a base thickness of 1.25 mm was used. A schematic view of the dynamic light scattering set-up and the optical path is shown in **Figure 11**. To follow the growth of the agglomerates, a good time-resolution of the DLS measurements was required. The DLS instrument was capable to perform DLS measurements with an integration time of 1 s, which is adequate to record autocorrelation function with

sufficient signal-to-noise-ratio and with distinguished corresponding specific mean residence times τ_{Diff} between nano- and microseconds.
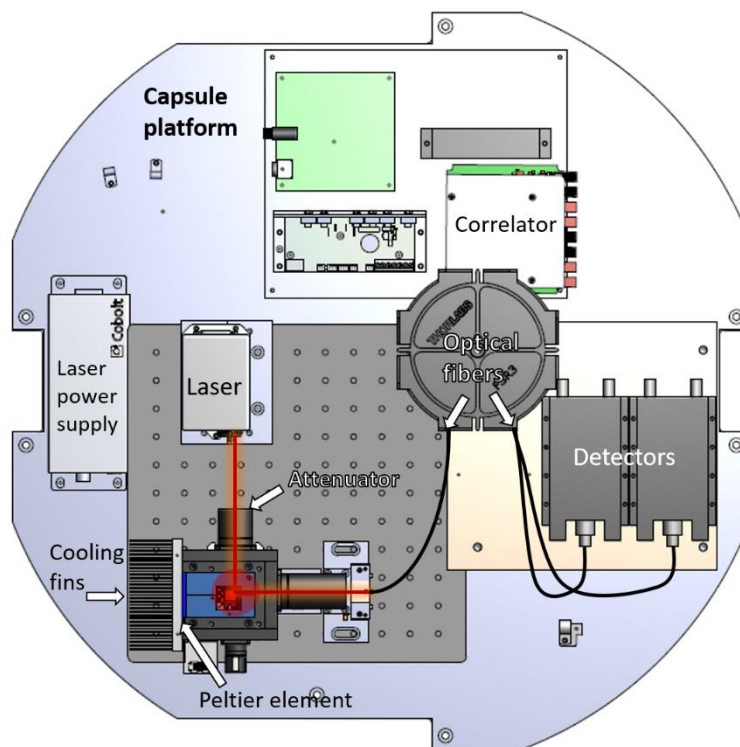
Figure 11: Schematic view of the dynamic light scattering instrument. The optical path is marked in red. Graphic modified from "Dynamic Light Scattering on Nanoparticles in Microgravity in a Drop Tower" by Pyttlik, Kuttich and Kraus in *Microgravity Science and Technology*, in **2022**.[196]

3.1.3 Liquid handling system to induce a rapid temperature drop

The final objective of this thesis was to study the agglomeration of hexadecanethiol-capped gold nanoparticles in tetradecane in microgravity. The hexadecanethiol-capped gold nanoparticles exhibit an agglomeration temperature of $T_{Agglo} = 60\,°C$ (compare also **Chapter 3.3.1**).[94,95,96,97] To ensure that the particles were completely dispersed before the experiment, the sample was heated up to $T = 70\,°C$. To be able to follow the agglomeration process during the microgravity duration of 9.3 s, a fast agglomeration of the nanoparticles needed to be induced. In addition to the analytical set-up, a system had to be integrated into the capsule allowing to induce agglomeration of the particles at a defined moment.

To do so, the system had to be heated above its agglomeration temperature and to be cooled down rapidly after complete dispersion. The measurement had to begin instantaneously after

start of agglomeration. For this purpose, a liquid sample handling system was designed (a schematic overview can be found in **Figure 12**). Using a syringe pump, liquid samples can be passed through an aluminum heating block that can in principle be heated up to 85°C. Subsequently, the heated sample can be transferred directly into the DLS measurement cell, which can be cooled down to 5 °C.

First, the sample was heated externally and injected into the aluminum heating block, which was already heated to 70 °C by using the syringe pump. The sample was stored at 70 °C until the experimental set-up entered microgravity. In the meantime, the measurement cell was pre-cooled to 10 °C. During the catapult launch of the capsule, the sample was injected into the measurement cell. The injection of the sample was completed as soon as the capsule entered microgravity and the DLS measurements were simultaneously started. The whole set-up could be controlled remotely. Due to this rapid temperature drop the particles were expected to agglomerate immediately, which was proven during the following experiments, see **Chapter 3.3**.
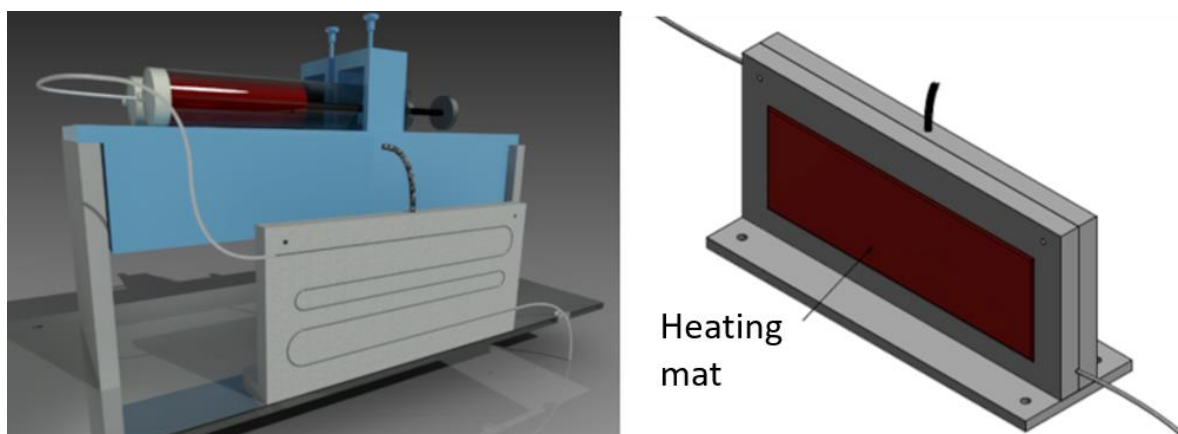
Figure 12: Schematic overview of the sample handling system and the aluminum heating block. The gold nanoparticle dispersion was injected with the syringe pump inside the heating block and heated to 70 °C, before injecting it into the pre-cooled measurement cell. From Pyttlik *et al.*, **2022**.[196]

3.1.4 Integration of the set-up into the drop capsule

Finally, the complete instrumental set-up needed to be integrated into a drop tower capsule. To have sufficient space and be able to arrange all parameters of the set-up conveniently, it was decided to design a staggered five-platform system, see **Figure 13**.

Initially, it was required to stabilize the flight of the capsule. For this purpose, the top platform of the catapult capsule was equipped with weight plates. On one hand, a general increase of the overall weight of the capsule had a stabilizing effect, on the other hand the additional weight was strategically placed to precisely balance out the mass center of the asymmetrical instrumental set-up. The second platform held the heating stage with the liquid handling system. The analytical set-up was integrated on the third platform. Here, the DLS set-up with the measurement cell to collect the data of the agglomeration process was installed. The fourth platform held the capsule-control computer. This computer was not only able to monitor dynamic data such as the acceleration of the capsule during the flight, but also enabled to access the instrumental set-up via remote control. The fifth and lowest platform held the power supplies for the devices discussed before.[266,267]
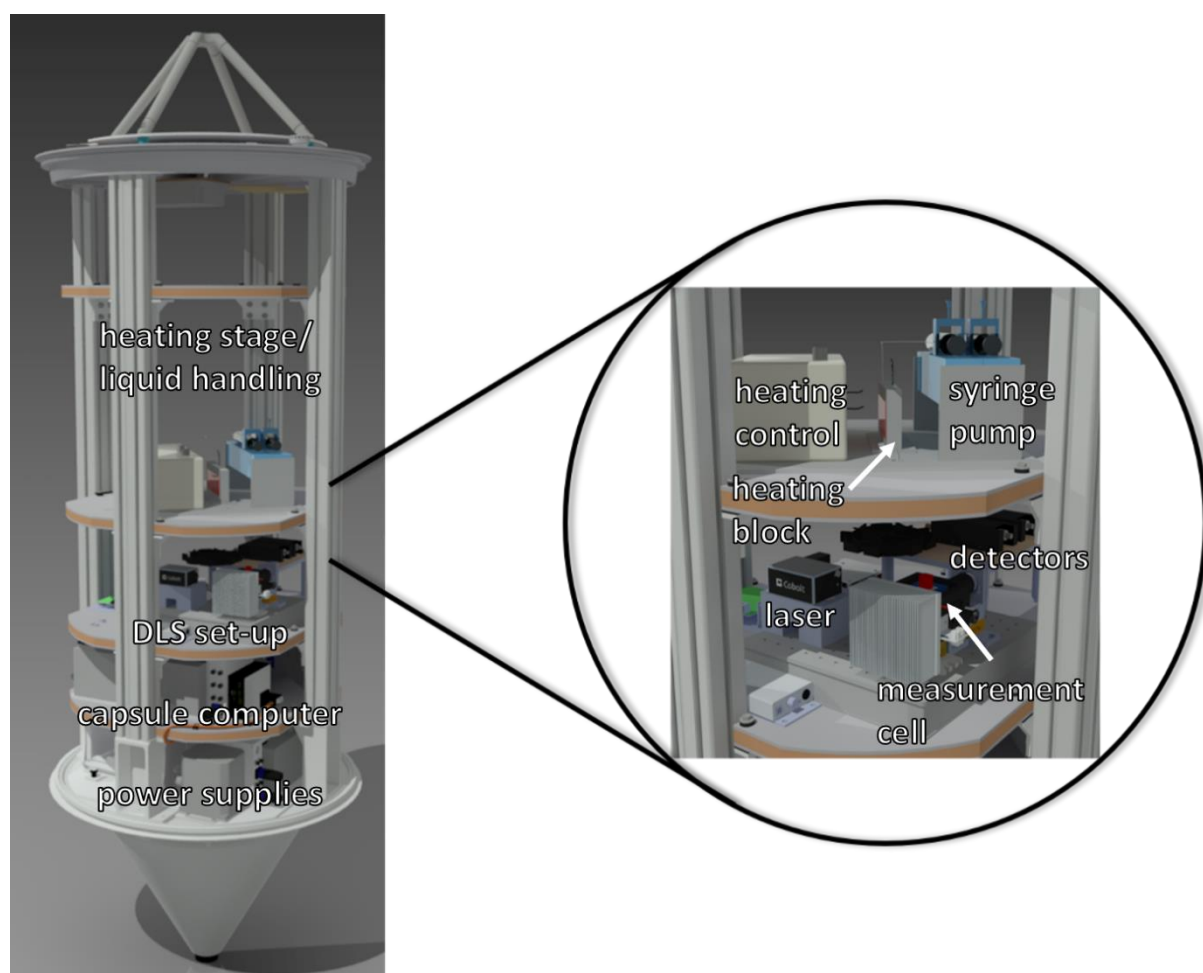

Figure 13: Schematic view of the instrumental set-up integrated into the drop tower capsule, visible are weight plates on the first (top) platform, the heating stage with the liquid handling on the second platform, the DLS set-up on the third platform, the capsule computer on the fourth and the power supplies on the fifth (lowest) platform. From Pyttlik *et al.*, **2022**.[196]

3.1.5 Test of the developed instrumental set-up

After the set-up was developed, as a very first step a proof-of-concept measurement should be performed. The main objective was to demonstrate that the dynamic light scattering device is indeed sufficiently robust to record reliable data in the drop tower. To minimize variables and limit this test measurement to the record of DLS data, we decided to do an initial experiment without using the liquid handling system (described in **Chapter 3.1.3**), by placing the sample directly into the measurement cell at room temperature. Furthermore, non-absorbing transparent silica nanoparticles in water were investigated during the proof-of-concept measurement as preferably simple particle system. The particles had a hydrodynamic diameter of d_H = 25 nm (± 3 nm). With this system, measurements were performed on ground and in microgravity at room temperature. Two catapult launches were performed with the test system and each time autocorrelation functions were recorded and analyzed. In **Figure 14**, autocorrelation functions recorded on ground are compared with an autocorrelation function recorded in microgravity. Selected autocorrelation functions recorded in microgravity are shown in **Figure 15**. The full set of recorded autocorrelation functions can be found in **Figure 54** in the appendix. The autocorrelation functions could be analyzed using a single exponential decay. It can be clearly seen that all autocorrelation functions show an identical shape indicating that reliable DLS experiments can be performed in the drop tower and that the acceleration of the catapult does not influence the measurement. Additionally, in microgravity, an identical hydrodynamic diameter of 25 nm (± 5 nm) was found compared to the ground measurements.
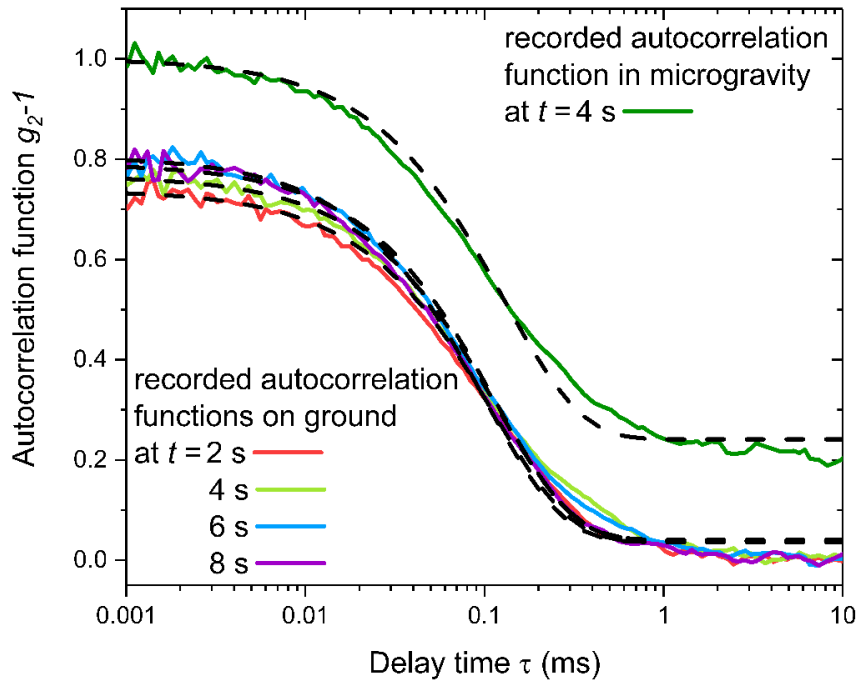
Figure 14: Selected autocorrelation functions (colored, solid lines) and corresponding fit (black, dashed lines) of silica nanoparticles in water on ground, compared with a recorded autocorrelation function and corresponding fit in microgravity. The recorded autocorrelation function in microgravity is shifted along the y-axis. The particles have a hydrodynamic diameter of d_H = 25 nm (± 3 nm). The measurements were performed at room temperature.
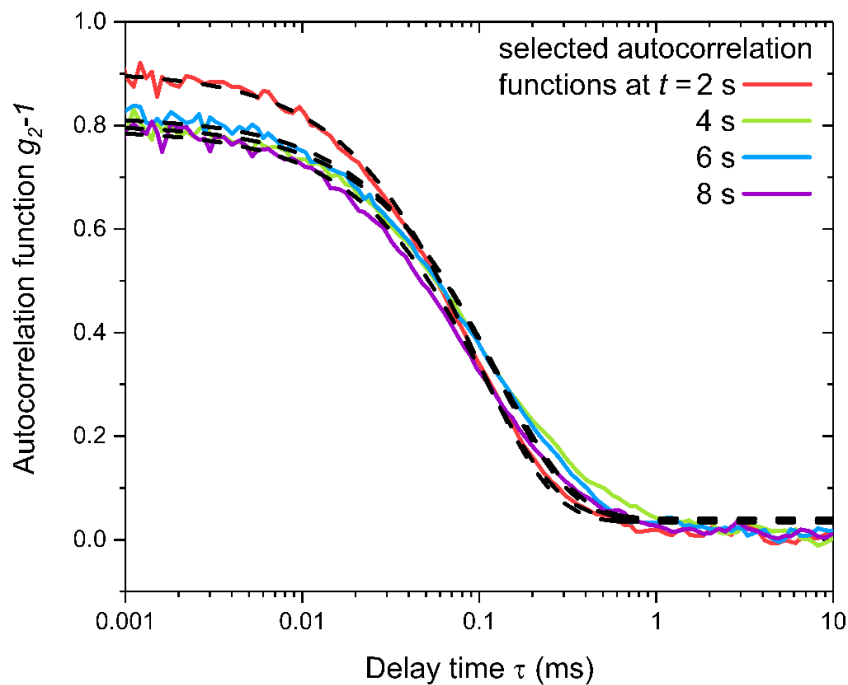
Figure 15: Autocorrelation function (colored, solid lines) and corresponding fit (black, dashed lines) of silica nanoparticles recorded in microgravity (µg) after a catapult launch. The particles had a hydrodynamic diameter of d_H = 25 nm (± 5 nm). The measurements were performed at room temperature.

3.2 Reference system

The results of the following chapter have been published in "Dynamic Light Scattering on Nanoparticles in Microgravity in a Drop Tower" by Pyttlik, Kuttich and Kraus in *Microgravity Science and Technology*, in **2022**.[196]

After the basic test with silica nanoparticles in water had proved that reliable DLS data can be collected in the drop tower despite physical stress during the catapult launch (see **Chapter 3.1.5**), the entire instrumental set-up was further tested with a non-agglomerating reference system. Objective of the investigation of this reference system was to demonstrate that the experimental procedures (injection into the measurement cell, temperature drop, catapult launch) had no significant influence on the data generated.

As reference system it was decided to study oleylamine (OAm) capped gold nanoparticles. The system was chosen since it showed no agglomeration in the investigated temperature range (70 °C – 10 °C, see also **chapter 3.2.2**) but, however, resembled the later investigated agglomerating system (hexadecanthiol-stabilized gold nanoparticles) as close as possible. Solvent, nanoparticle core size and material were identical to the agglomeration system planned to investigate. The only difference was the ligand shell, which does not have a significant influence on the scattering contrast. As agglomeration system hexadecanthiol-stabilized gold nanoparticles were used, which show a temperature-dependent agglomeration with an agglomeration temperature of T_{Agglo} = 60 °C.

The OAm-capped gold particles had a core diameter of 7.8 nm (± 0.4 nm) and a hydrodynamic diameter of d_H = 21 nm (± 1 nm) and were dispersed in tetradecane. To exclude any unwanted effects on the DLS measurement resulting from the catapult launch or the rapid temperature change, DLS measurements were performed at a constant temperature of 20 °C and with a temperature drop (70 °C to 10 °C) and each experiment was performed on ground and in microgravity.

3.2.1 Renewal of the oleylamine ligand shell

Oleylamine-capped gold nanoparticles were synthesized in toluene according to the route of Zheng *et al.*[269] A core diameter of 8.0 nm (± 0.6 nm) was determined by SAXS measurements and a hydrodynamic diameter of d_H = 14 nm (± 0.8 nm) was measured via DLS. Considering the ligand length of d_L = 2 nm for oleylamine,[270] the measured hydrodynamic diameter is in line with expectations. The hydrodynamic diameters of sterically stabilized non-polar nanoparticles is typically determined by the most outward extended ligand tail.[271] Assuming a monolayer of oleylamine which is typically observed,[271] the hydrodynamic diameter is expected according to **Equation (37)**, see **Figure 16**.

$$d_H = d_{Core} + 2 \cdot d_L \tag{37}$$
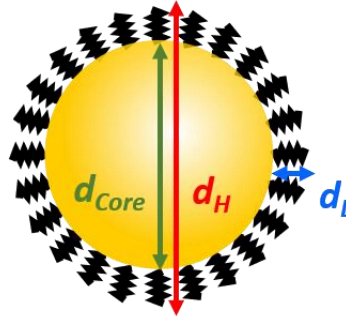
Figure 16: Schematic overview of the relationship between the core diameter d_{Core} of the gold nanoparticles, the ligand length of oleylamine d_L and the hydrodynamic diameter of the particles d_H. Inspired by S. Hinman "Plasmonic Interrogation of Biomimetic Systems for Enhanced Toxicity Assays".[272]

After the synthesis of the oleylamine-capped gold nanoparticles, a direct use of the freshly prepared particle system could not be realized due to the organizational aspects of performing experiments in the drop tower in Bremen. The sample had to be stored for at least two weeks at room temperature before experiments in microgravity could be performed. Oleylamine is only weakly bond to the gold surface of the particles, and can in principle desorb from the surface over time.[273] To ensure an intact ligand shell during the agglomeration experiments, the ligand shell was generally renewed on-site. To guarantee microgravity and ground experiments were performed under the same preconditions, the ligand shell was also renewed prior to the ground experiments.

To renew the ligand shell, oleylamine-capped nanoparticles in toluene were heated under reflux and additional oleylamine was added to the suspension. The sample was stirred under reflux for a certain reaction time (Δt). The excessive oleylamine was removed by precipitation of the gold nanoparticles with a mixture of ethanol and methanol (2:1) followed by centrifugation. Subsequently, the particles were redispersed in toluene. This washing step was repeated 3 times. After the last washing step, the particles were redispersed in tetradecane. It was decided to perform all DLS measurements in tetradecane as solvent, to ensure that all experiments performed with the reference system are as similar as possible to the experiments performed with the agglomerating system, which are described in **Chapter 3.3**. DLS measurements after the renewal of the ligand shell revealed that the reaction time of the heated sample affected the hydrodynamic diameter of the product. The reaction mixture was either heated for $\Delta t = 30$ min or for $\Delta t = 150$ min after oleylamine was added. DLS measurements were always performed after the particles were washed and transferred in tetradecane. A comparison of the obtained hydrodynamic diameters can be found in **Figure 17**. After $\Delta t = 30$ min, the hydrodynamic diameter decreased from 14 nm (± 0.8 nm) to 10 nm (± 0.6 nm). After $\Delta t = 150$ min, however, the hydrodynamic diameter increased to 19 nm (± 0.7 nm). To exclude a change of the core diameter, SAXS measurements were performed on the samples two weeks after the synthesis and after renewing the ligand shell. **Figure 18** shows that the core diameter remained constant at 8.0 nm (± 0.6 nm), excluding any changes of the gold core particles. To explain the increased hydrodynamic diameter of the particles after renewal of the ligand shell (with a reaction time of $\Delta t = 150$ min) compared to the hydrodynamic diameter of the synthesis of the particles, a formation of oleylamine multilayers on the surface of the gold nanoparticles is assumed. To ensure identical conditions for all the sample used as referenced systems (see **Chapter 3.2.2** - **3.2.5**), renewal of the ligand shell with a reaction of $\Delta t = 150$ min was performed before any experiments were conducted.
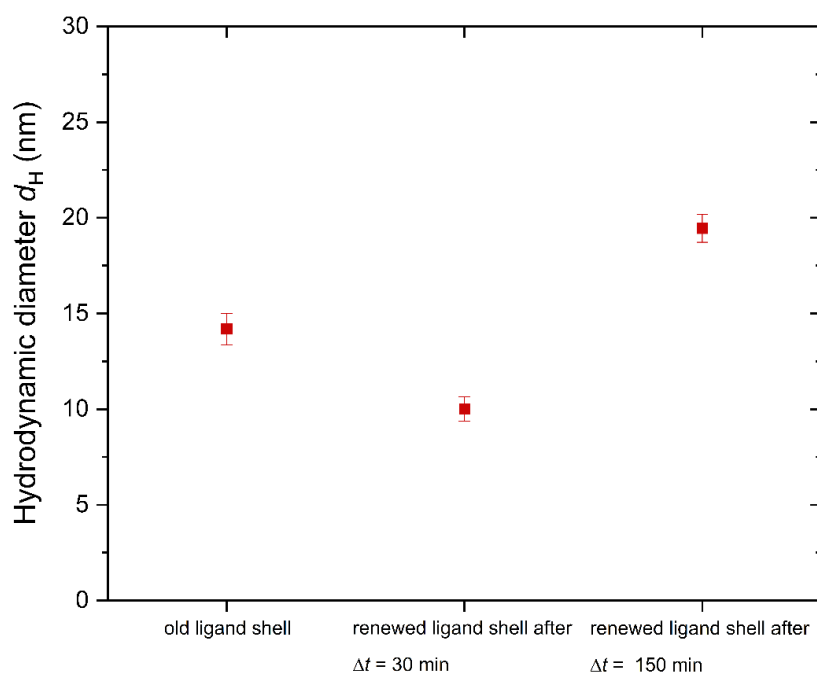
Figure 17: Obtained hydrodynamic diameters of oleylamine-capped gold nanoparticles in tetradecane, at room temperature. The particles had a core diameter of $d_{Core} = 8.0$ nm ($\pm$ 0.6 nm). Shown are the initial hydrodynamic diameter after the sample were synthesized and after the renewal of the ligand shell with a reaction time of $\Delta t = 30$ min and $\Delta t = 150$ min. From Pyttlik *et al.*, **2022**.[196]
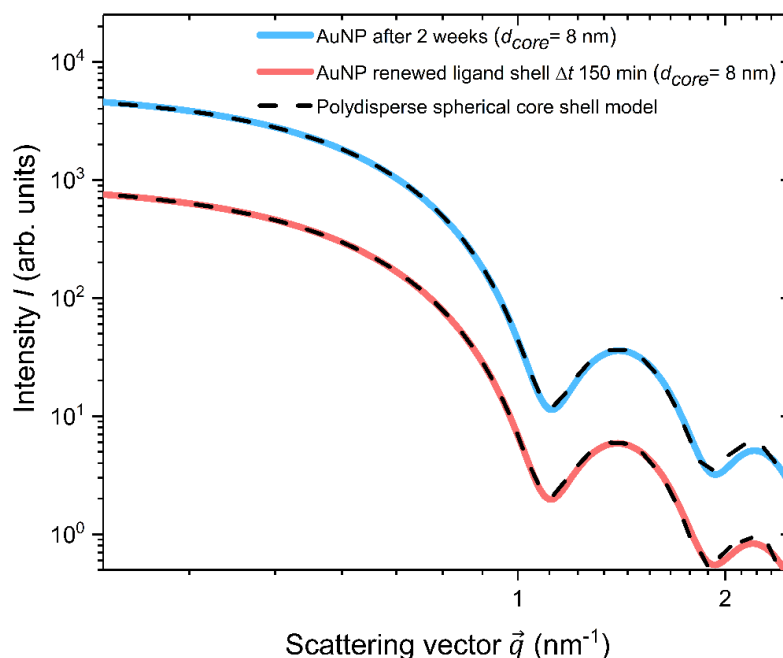
Figure 18: SAXS measurement (colored, solid lines) and corresponding fit (back, dashed lines) of gold nanoparticles after the synthesis and after renewal of the ligand shell with a reaction time of $\Delta t = 150$ min. A core diameter of $d_{Core} = 8$ nm ($\pm$ 0.6 nm) was obtained for both samples.[196] The data were analyzed using a polydisperse spherical core shell model, see **Equation (17)**. From Pyttlik *et al.*, **2022**.[196]

## 3.2.2 Temperature dependent behavior of the gold reference system

In **Chapter 3.3.2** and **Chapter 3.3.3** the study of the agglomeration of hexadecanethiol-capped gold nanoparticles in tetradecane by DLS measurements was discussed. For this purpose, an experimental set-up was developed and described in **Chapter 3.1**. To be able to distinctively identify the influence of gravity on the agglomeration process, the experiments were first performed by using the non-agglomerating reference system and later compared with the agglomerating system. With this approach any additional influences of gravity on the particle system or the DLS measurements can be excluded allowing to solely focus on the influence of gravity on the agglomeration process.

To finally ensure that the reference system indeed showed no agglomeration, the used oleylamine-capped gold nanoparticles need to be stable in the relevant temperature range from 70 °C to 10 °C in tetradecane. To demonstrate the corresponding stability, SAXS and DLS measurements were performed. SAXS data were recorded at 70 °C and 10 °C and are shown in **Figure 19**. At both temperatures, a core diameter of 7.8 nm was found showing no signs of a structure factor, which demonstrates that the nanoparticles were stable during the temperature change from 70 °C to 10 °C and that the particles do not agglomerate in the used temperature range.

Additionally, DLS measurements were performed from 60 °C to 5 °C in 5 K intervals to ensure that the hydrodynamic diameter also stays constant in this temperature range. The resulting hydrodynamic diameters are shown in **Figure 20**. For each measurement the temperature and the corresponding viscosities and refractive indices were used to calculate the corresponding hydrodynamic diameters, see **Chapter 2.3.1**. Over all measured temperatures an average hydrodynamic diameter of 22 nm was found with a standard deviation of 3 nm. Those findings demonstrate that the hydrodynamic diameter of the particles stays constant in the measured temperature range. Some small variabilities during the cooling of the sample could be observed, they were likely the result of the uncertainties of the temperature dependent viscosity and refractive index of the solvent. In this temperature range, values for the viscosity and the refractive index of tetradecane had to be extrapolated from literature, see **Chapter 2.3.1**.
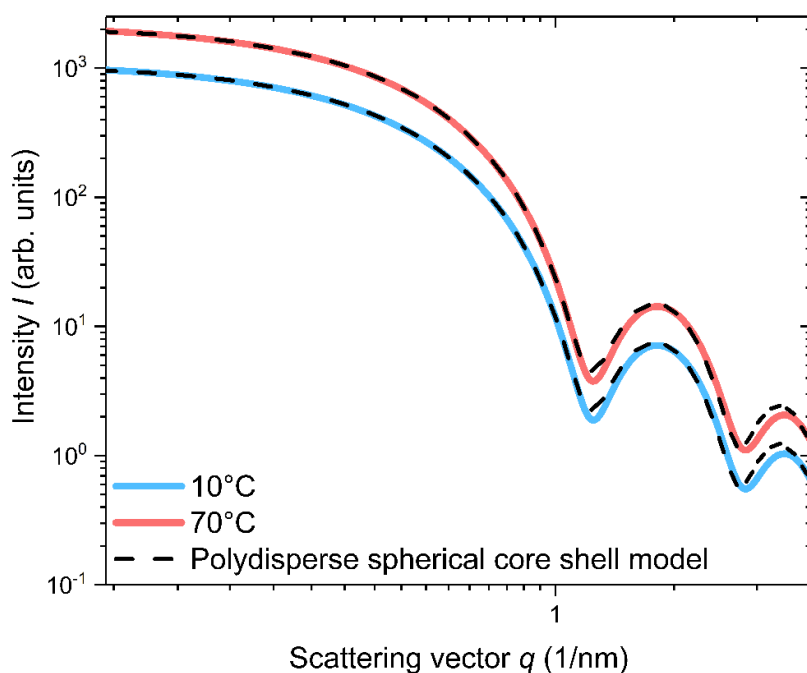
Figure 19: Recorded SAXS data (colored, solid lines) and corresponding fits (black, dashed lines) of oleylamine-capped gold nanoparticles in tetradecane. The measurements were performed at 70 °C and 10 °C. The data measured at 70 °C were multiplied by a factor of 2 to improve the display and the comparison of the two measurements. The data were analyzed using a polydisperse spherical core shell model, **see Equation (17).** From Pyttlik *et al.*, **2022.**[196]
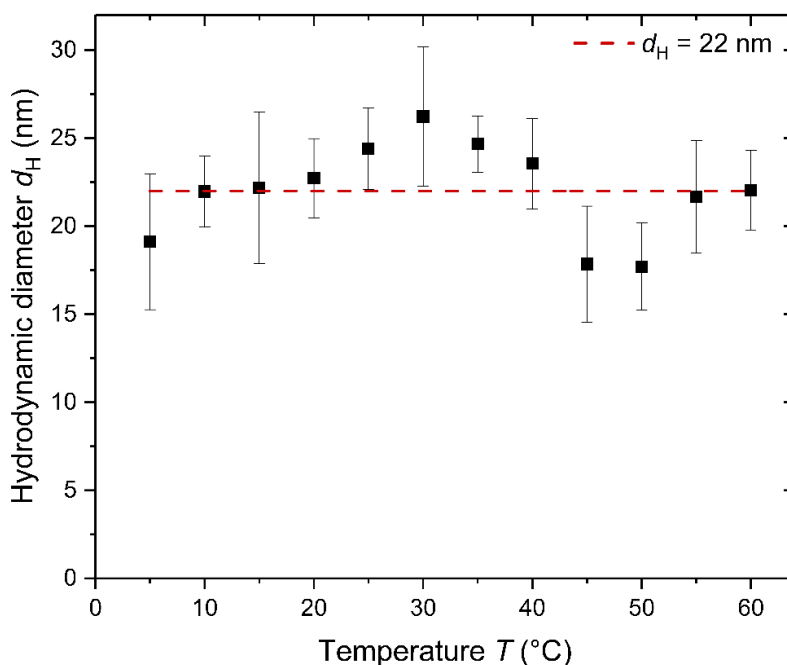
Figure 20: Hydrodynamic diameter d_H of oleylamine-capped gold nanoparticles in tetradecane over temperature. The sample was heated to 60 °C and cooled to 5 °C. Measurements were performed at 5 °C intervals. Each measurement was repeated three times and the mean average, and the standard deviation are shown. Over all temperatures (60 °C to 5 °C) an average hydrodynamic diameter of d_H = 22 nm (± 3 nm) was found. From Pyttlik *et al.*, **2022.**[196]

### 3.2.3 Determination of the temperature inside the measurement cell

In order to interpret DLS measurements, the exact temperature at the time of measurement has to be known. DLS initially measures the mean residence times τ_{Diff} of the particles in a scattering volume. The hydrodynamic diameter d_H of the particles is subsequently calculated via the Stokes-Einstein relation by using the temperature dependent viscosity and refractive index of the solvent, see **Chapter 2.3.1**. It has to be considered that after inducing the agglomeration by rapid cooling of the sample, the temperature changes during the subsequent agglomeration process. Consequently, to be able to calculate the hydrodynamic diameter of the growing agglomerates, the temperature at which each single autocorrelation function was recorded needs to be known.

In a first attempt, we measured the temperature inside the measurement cell by using a thermocouple type K. Experiments were performed to evaluate the reliability of the temperature determination. First, three measurements were recorded with pure tetradecane, and the thermocouple was placed close to the scattering volume at the bottom of the cuvette. Afterwards, three measurements were performed with the reference gold nanoparticle dispersion on ground and one in microgravity. To enable simultaneous DLS measurements of the gold nanoparticles, the thermocouple was placed sufficiently above the measurement volume. Gold nanoparticles with a hydrodynamic diameter of 21 nm (± 1 nm) and a concentration of 0.72 mg mL^{-1} were used. For each measurement, the sample was heated up to 70 °C inside the heating stage and injected into the pre-cooled measurement cell (10 °C) by using a syringe pump (see **Chapter 3.1**). As shown in **Figure 21**, the average temperatures showed a broad standard deviation and varied between experiments by an average of approximately 10 K. These uncertainties of the temperature measurements might have occurred due to slight variations of the thermocouple placement and the liquid flow during the injection of the sample inside the cuvette. However, it is difficult to improve control of these parameters impeding the direct temperature measurement of the measurement volume.

It was shown that the temperature measurement in microgravity was in good agreement with the measurement performed on ground, indicating a similar temperature development on ground and in microgravity. With the temperature measured in tetradecane and in the particle dispersion on ground and in microgravity, an average temperature profile was calculated and

used to determine the hydrodynamic diameter of the reference gold nanoparticle samples during the temperature drop. The performed DLS experiments are described in **Chapter 3.2.4**. The used temperature profile and the corresponding dynamic viscosities and refractive indices of tetradecane are summarized in **Table 1**. The measured mean residence times of the referenced system (measurements described in **Chapter 3.2.4**) and the corresponding calculated hydrodynamic diameters are also listed in **Table 1.** A comparison of the hydrodynamic diameter during the temperature drop with the obtained hydrodynamic diameter at a constant temperature (20 °C) on ground (see **Figure 22**) shows that the calculated apparent hydrodynamic diameters during the temperature drop were significantly smaller than the hydrodynamic diameters obtained at the constant temperature.
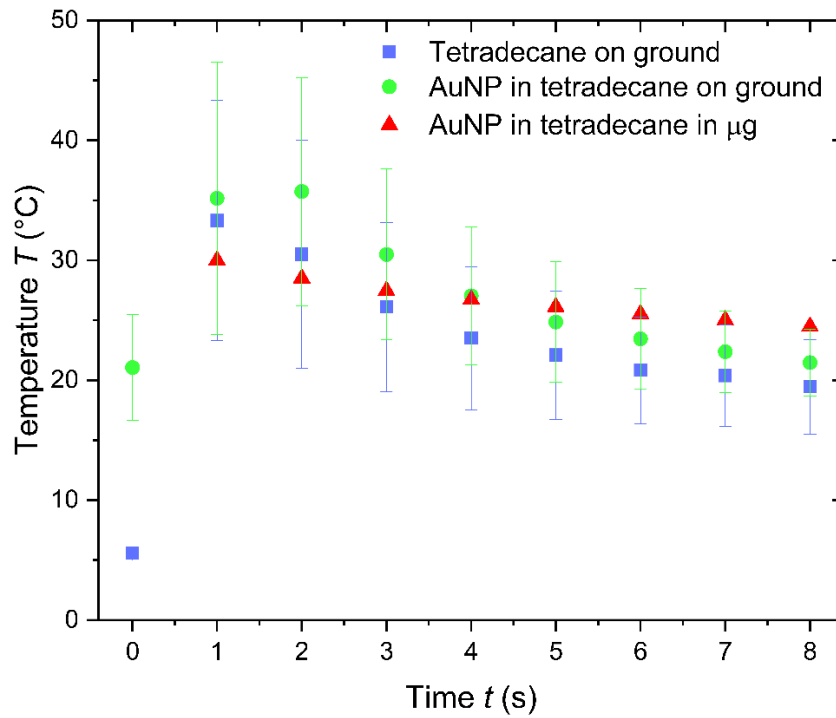
Figure 21: Measured temperatures (*T*) over time (*t*) inside the measurement cell. Tetradecane and the gold nanoparticle suspension were heated to 70 °C inside the heating stage and injected into the pre-cooled measurement cell (10 °C). On ground three measurements with tetradecane and three measurements with the gold nanoparticle dispersion were performed. The average temperatures and their standard deviations are shown. In microgravity one measurement with the gold nanoparticle suspension was performed. From Pyttlik *et al.*, **2022**.[196]

Table 1: Time-dependent (t) mean residence time (τ_{Diff}) of gold nanoparticles after a temperature drop (70 °C to 10 °C) according to DLS measurement performed in **Chapter 3.2.4**. The apparent hydrodynamic diameter of the particles (d_H) was calculated assuming the following time-dependent temperature (T) of the sample and the viscosity (η), and refractive index (n) of tetradecane. From Pyttlik *et al.*, **2022**.[196]

t (s)	τ_{Diff} (ms)	d_H (nm)	T (°C)	η (mPas s)	n
1	0.08	8	30	1.89	1.4235
2	0.13	12	29	1.92	1.4236
3	0.16	13	25	2.08	1.4254
4	0.16	13	23	2.17	1.4263
5	0.18	13	21	2.27	1.4272
6	0.18	13	20	2.32	1.4276
7	0.18	13	20	2.32	1.4276
8	0.19	13	19	2.37	1.4281
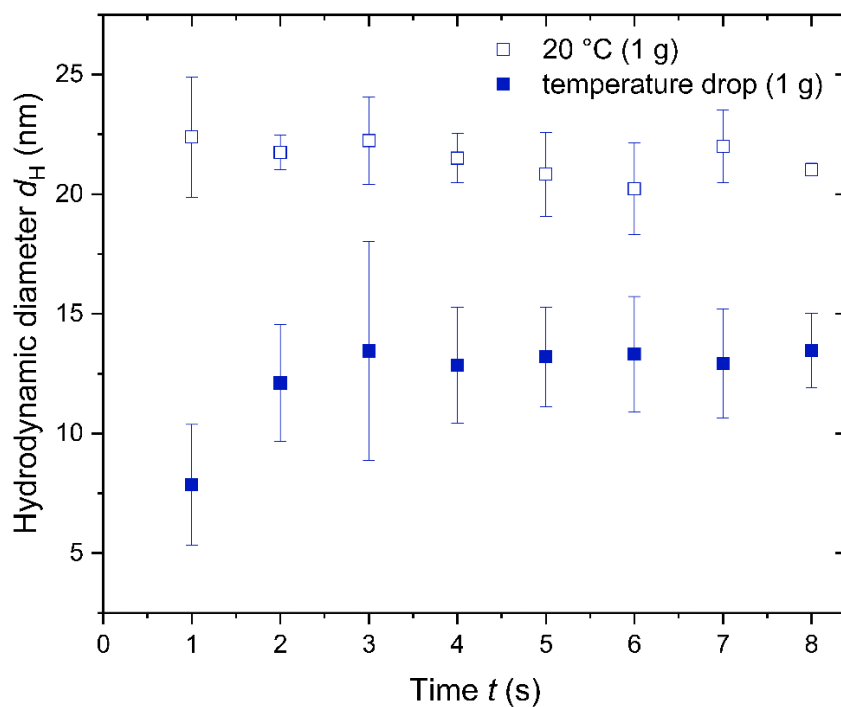
Figure 22: Hydrodynamic diameter of d_H over time t of oleylamine-capped gold nanoparticles in tetradecane with a core diameter of d_{Core} = 7.8 nm at a constant temperature (20 °C) and during a temperature drop (70 °C to 10 °C). Each measurement was repeated three times, the mean average and the standard deviation are shown. From Pyttlik *et al.*, **2022**.[196]

In the previous **Chapter 3.2.3** it was demonstrated that changing the temperature does not influence the hydrodynamic diameter of the particles (see **Figure 20**), so the hydrodynamic diameters measured at a constant temperature of 20 °C and during a temperature drop were expected to be identical. It is worth mentioning, that the stability of the hydrodynamic diameter of the reference system at different temperatures was investigated by placing the sample inside the measurement cell and slowly cooling/heating the sample using the integrated Peltier element of the measurement cell. Here we tried to measure the temperature inside the measurement cell during the temperature drop.

An important difference by accomplishing the rapid temperature drop compared to the slow cooling of the sample was that the hot sample was injected into the precooled measurement cell by using the syringe pump. To exclude a change of the hydrodynamic diameter due to the rapid injection of the sample, additional experiments were performed. The reference system was injected into the measurement cell at room temperature to be able to exclude any influence of the liquid flow of the sample on the DLS measurements. Gold nanoparticles with a core diameter of 7.8 nm, capped with oleylamine in tetradecane were measured at a constant temperature (20 °C) and measured after the sample was injected from the heating stage into the measurement cell by a syringe pump at room temperature (25 °C). As shown in **Figure 23**, the measured mean residence times τ_{Diff} and the resulting hydrodynamic diameters were in good agreement confirming that sample injection had no influence on the hydrodynamic diameter of the sample.
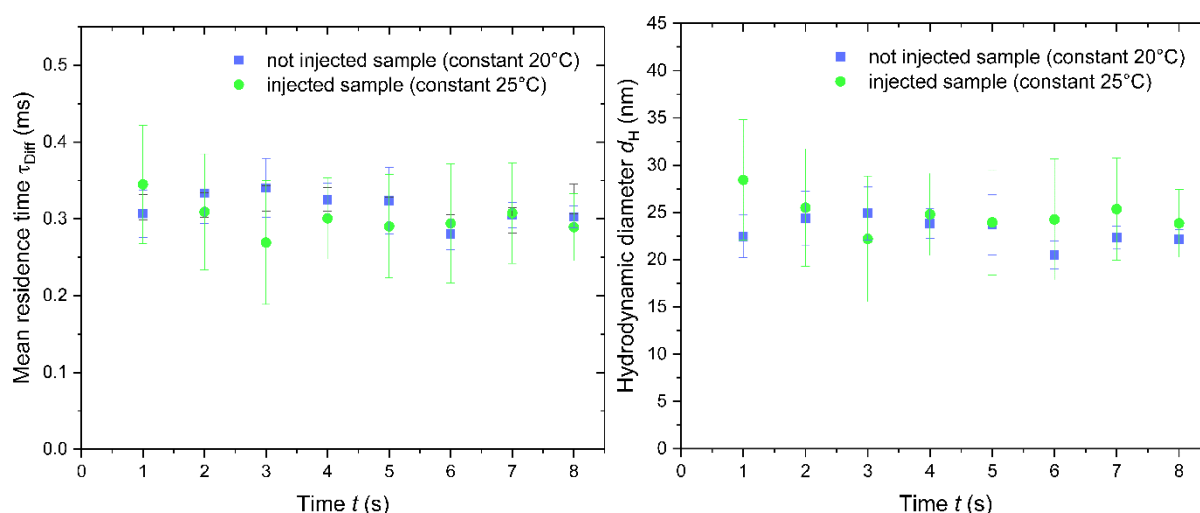
Figure 23: Mean residence time τ_{Diff} and hydrodynamic diameter d_H over time of gold nanoparticles. A non-injected sample at a constant temperature (20 °C) and an injected sample at room temperature (25 °C). Each measurement was repeated three times and the mean average, and their standard deviation are shown. From Pyttlik *et al.*, **2022**.[196]

This finally supports the conclusion that the smaller hydrodynamic diameters shown in **Figure 22** were caused by unreliable temperature measurements with the thermocouple, which could not represent the actual temperatures inside the measurement volume during the temperature drop.

To enhance the accuracy of the used temperature data, a different approach was chosen. Since it was proven that neither changing the temperature nor injecting the sample inside the measurement cell by using the syringe pump (see **Figure 22** and **Figure 23**) affected the hydrodynamic diameter of the particles, it can be assumed that the hydrodynamic diameter of the reference system stays also constant during the rapid temperature drop. Consequently, the gold nanoparticles can be exploited as a probe to determine the exact temperature, basically using them as a thermometer. By measuring their mean residence times τ_{Diff} during the temperature drop, the corresponding temperatures were calculated by using their already known hydrodynamic diameter and the Stokes-Einstein relation (see **Equation (32)**). Considering the temperature dependency of the refractive index and the viscosity of the solvent (see **Equation (33)** and **Equation (34)**), **Equation (32)** was solved numerically using the software Mathematica 11. The resulting temperatures and the corresponding uncertainties are listed in **Table 2**. During the first second, the obtained temperature was unexpectedly high and showed a high uncertainty. This indicates, that the DLS measurements with a temperature drop were affected by the convection caused by the rapid temperature drop. Considering that the main focus of this work was the investigation of the agglomeration process of gold nanoparticles under microgravity during the agglomeration process, a change of the hydrodynamic diameter in the order of one or two magnitudes was expected. The obtained temperatures showed a considerable uncertainty, but are still smaller than the expected large change of the hydrodynamic diameter. Consequently, the observation of the agglomeration process during the temperature drop was possible and will be described in the following chapters.

Table 2: Time dependent temperatures (*T*) measured using gold nanoparticles as thermometer inside the measurement volume during the temperature drop. A constant hydrodynamic diameter of 22 nm was assumed. The corresponding viscosity and refractive index for tetradecane are given. From Pyttlik *et al.*, **2022**.[196]

| *t* (s)	*T* (°C)	η (mPas s)	*n*
1	94 (± 26)	0.73	1.3948
2	62 (± 12)	1.11	1.4090
3	53 (± 21)	1.27	1.4130
4	51 (± 10)	1.31	1.4139
5	47 (± 9)	1.39	1.4156
6	45 (± 9)	1.44	1.4165
7	46 (± 9)	1.42	1.4161
8	43 (± 6)	1.49	1.4174

3.2.4 Ground experiments with the reference system

DLS measurements were carried out with the reference system on ground and later compared to the measurement performed in microgravity to investigate any influence of microgravity on the instrumental set-up or the DLS measurements.

Gold nanoparticles with a core diameter of d_{Core} = 7.8 nm, capped with oleylamine in tetradecane were used. The dispersion had a gold concentration of c = 0.72 mg mL^{-1}, corresponding to a particle concentration of 1.5 x 10^{14} mL^{-1}. The same sample was later used to perform DLS measurements under microgravity conditions. Measurements were performed at a constant temperature of *T* = 20 °C as well as with a temperature drop. During each DLS measurement, eight consecutive autocorrelation functions with an integration time of 1 s were recorded. Each measurement was repeated three times at 20 °C and three times with a temperature drop (70 °C to 10 °C). Selected autocorrelation functions and the corresponding fits are shown in **Figure 24** and **Figure 25**. All recorded autocorrelation functions are shown in the appendix (see **Figure 55** and **Figure 56**).
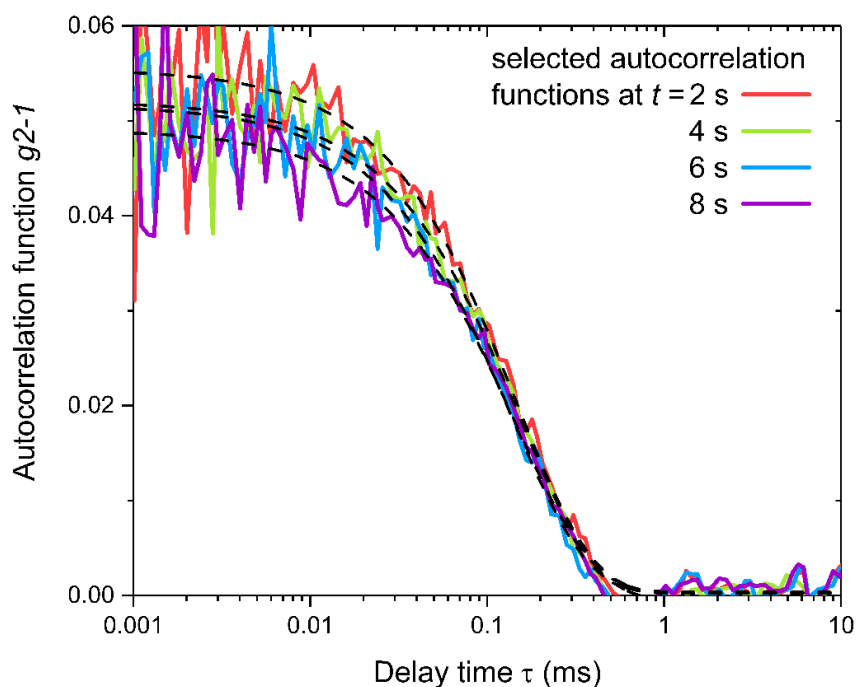
Figure 24: Selected autocorrelation functions (colored, solid lines) and corresponding fits (black, dashed line) with an integration time of 1 s of oleylamine-capped gold nanoparticles in tetradecane. The dispersion had a gold concentration of c = 0.72 mg mL^{-1} (± 0.03 mg mL^{-1}). The measurement was performed at a constant temperature of T = 20 °C on ground (1 g). From Pyttlik *et al.*, **2022**.[196]
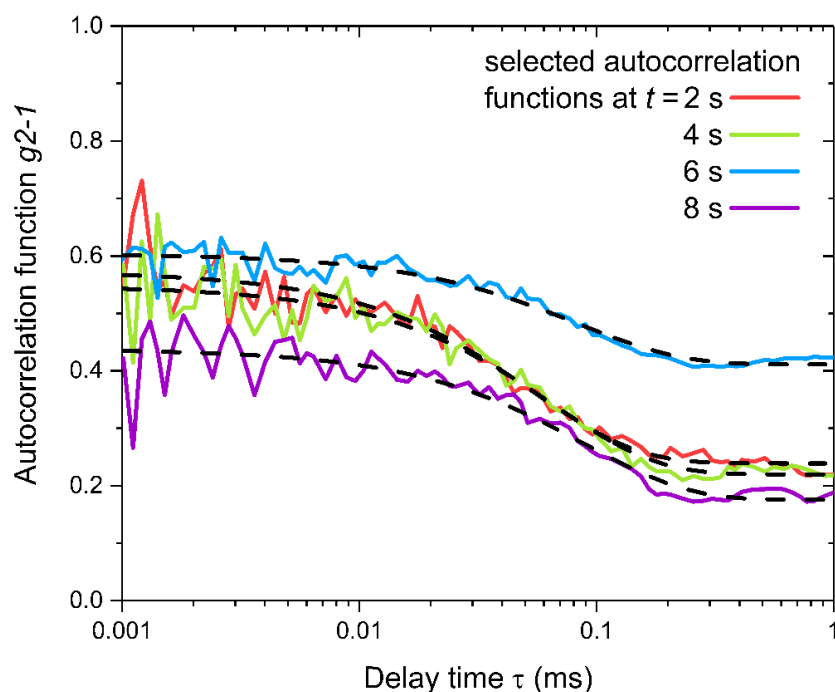
**Figure 25:** Selected autocorrelation functions (colored, solid lines) and corresponding fits (black, dashed line) with an integration time of 1 s of oleylamine-capped gold nanoparticles in tetradecane. The dispersion had a gold concentration of c = 0.72 mg mL^{-1} (± 0.03 mg mL^{-1}). The measurement was performed with a rapid temperature drop (70 °C to 10 °C) on ground (1 g). From Pyttlik *et al.*, **2022**.[196]
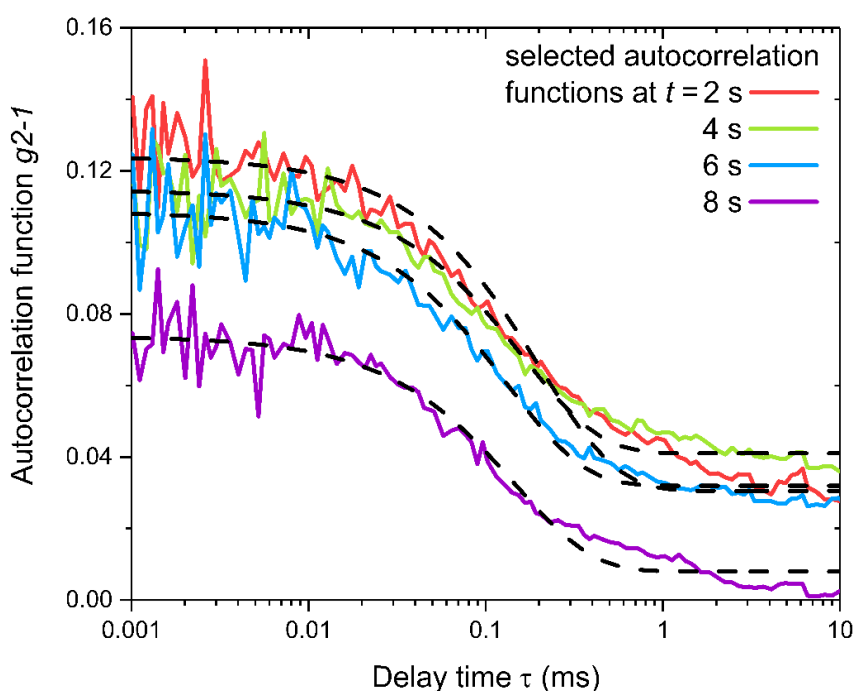
The autocorrelation functions were analyzed by fitting a single exponential decay (see **Equation (30)**) and a good agreement between the experimental data and the fit was demonstrated (see **Figure 24** and **Figure 25**). At a constant temperature of 20 °C, an averaged mean residence time of τ_{Diff} = 0.29 ms (± 0.01 ms) corresponding to a hydrodynamic diameter of d_H = 21 nm (± 1 nm) was found. During the temperature gradient, the obtained mean residence times τ_{Diff} were increasing, as expected for a cooling sample, see **Figure 26**. Overall, it was shown that it was possible to record reliable autocorrelation functions with an integration time of only 1 s, not only at a constant temperature but also during a rapid temperature drop induced by the liquid handling system. In **Chapter 3.2.5**, the test of the instrumental set-up under microgravity conditions in the drop tower at the ZARM Institute (Center of Applied Space Technology and Microgravity) will be described.
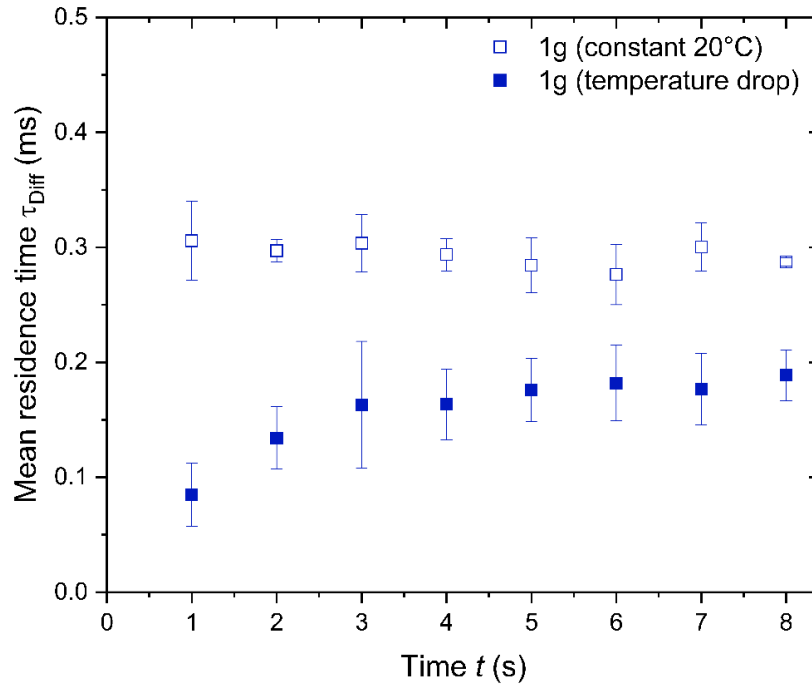
Figure 26: Mean residence time τ_{Diff} over time t of oleylamine-capped gold nanoparticles with a core diameter of d_{Core} = 7.8 nm in tetradecane at a constant temperature (20 °C) and with a temperature drop (70 °C to 10 °C). Each measurement was performed on ground and repeated three times and the average mean residence times τ_{Diff} and their standard deviation are shown. From Pyttlik *et al.*, **2022**.[196]

3.2.5 Microgravity experiments with the reference system

After the experimental set-up was proven to be able to record reliable DLS measurements even with a temperature drop, experiments were finally repeated under microgravity conditions. Oleylamine-capped gold nanoparticles in tetradecane with a core diameter of d_{Core} = 7.8 nm and a hydrodynamic diameter of d_H = 21 nm (± 1 nm) were used. The dispersion had a gold concentration of c = 0.72 mg mL^{-1}, corresponding to a particle concentration of 1.5 x 10^{14} mL^{-1}. Measurements were performed at 20 °C and during a temperature drop (70 °C to 10 °C). The experiments were carried out by performing catapult launches at the drop tower at the ZARM Institute. All parameters were identical with the ground experiments, described in **Chapter 3.2.4**. One DLS measurement was performed at a constant temperature of T = 20 °C, and two experiments were performed with a temperature gradient (70 °C to 10 °C). Selected autocorrelation functions are shown in **Figure 27** and **Figure 28**. All autocorrelation functions are shown in the appendix (see **Figure 57** and **Figure 58**).

Figure 27: Selected autocorrelation functions (colored, solid lines) and corresponding fits (black, dashed line) with an integration time of 1 s of oleylamine-capped gold nanoparticles in tetradecane. DLS measurements were performed at a constant temperature of T = 20 °C in microgravity (µ g) by performing a catapult launch. The dispersion had a gold concentration of c = 0.72 mg mL^{-1} (± 0.03 mg mL^{-1}). From Pyttlik *et al.*, **2022**.[196]
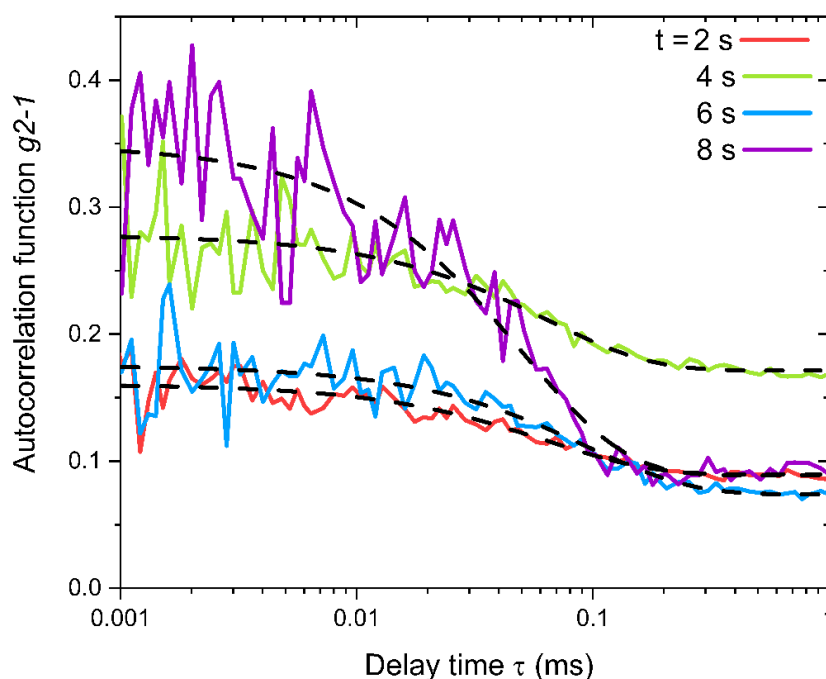
Figure 28: Selected autocorrelation functions (colored, solid lines) and fits (black, dashed line) with an integration time of 1 s of oleylamine-capped gold nanoparticles in tetradecane. DLS measurements were performed with a rapid temperature drop (70 °C to 10 °C) in microgravity (µ g) by performing a catapult launch. The dispersion had a gold concentration of $c = 0.72$ mg mL^{-1} (± 0.03 mg mL^{-1}). From Pyttlik *et al.*, **2022**.[196]

A reduced intercept and thus a reduced plateau value at fast correlation times of the autocorrelation compared to the ones recorded on ground were noticeable and were probably caused by slight misalignment of the optics during the catapult launch. The autocorrelation functions were analyzed using a single exponential decay (see **Equation (30)**) and a good agreement between the experimental data and the fit was observed (see **Figure 27** and **Figure 28**). At a constant temperature of 20 °C, the mean residence times τ_{Diff} on the ground and in microgravity were in good agreement, see **Figure 29**. With a temperature drop, the obtained mean residence times τ_{Diff} on the ground and in microgravity were also in good agreement, and increasing as expected for a cooling sample. It is worth mentioning that the mean residence times τ_{Diff} during a temperature drop experiment were lower than at a constant temperature of 20 °C, even at the end of the experiment after 8 s since the temperature inside the cuvette never drops below 37 °C, see **Table 2**.
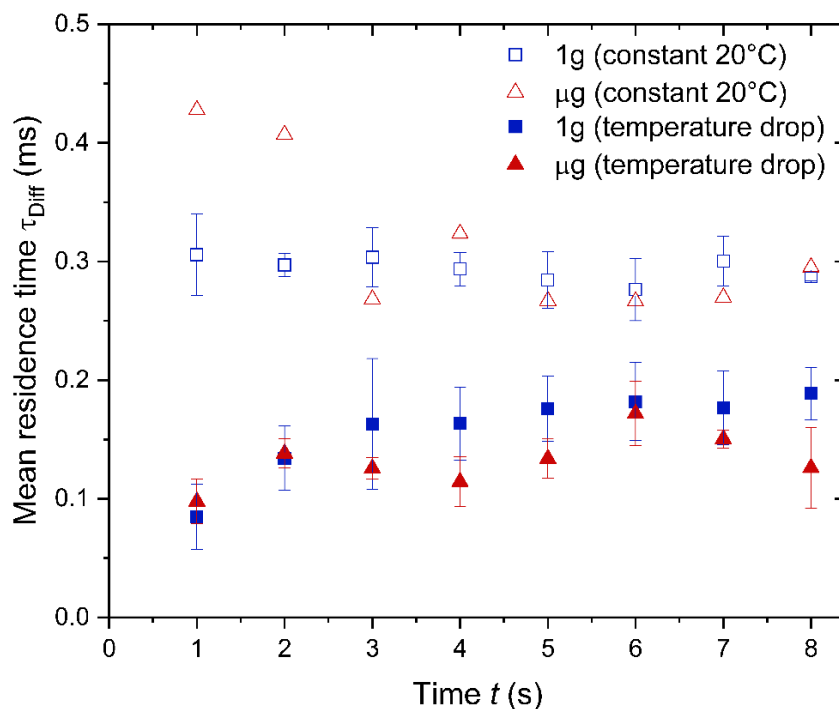
Figure 29: Mean residence times τ_{Diff} over time t of oleylamine-capped gold nanoparticles in tetradecane. Three experiments were performed on the ground at a constant temperature of 20 °C and with a temperature drop (70 °C to 10 °C), the average mean residence times τ_{Diff} and the standard deviation are shown. One experiment was performed in microgravity with a constant temperature of 20 °C. Two experiments were performed in microgravity with a temperature drop (70 °C to 10 °C), the average mean residence times τ_{Diff} and their standard deviation are shown. From Pyttlik *et al.*, **2022**.[196]

At a constant temperature, a mean residence time of τ_{Diff} = 0.31 ms (± 0.07 ms) corresponding to a hydrodynamic diameter of d_H = 23 nm (± 5 nm) was found, showing a good agreement between the measurements in microgravity and on ground. Experiments with a temperature drop were repeated twice and mean average times between 0.10 ms and 0.13 ms were found. The corresponding hydrodynamic diameters were determined using the temperatures calculated in **Table 2** and are shown in summary in **Table 3**. The uncertainties of the hydrodynamic diameter d_H were calculated by error propagation considering the temperature uncertainties in **Equation (32)**. A comparison with the hydrodynamic diameters obtained at a constant temperature in microgravity and on ground showed that they were in good agreement (see **Figure 30**), proving the possibility to record reliable autocorrelation functions in microgravity, after a catapult launch was performed and during a temperature drop.

Table 3: Time-dependent mean residence times τ_{Diff} of oleylamine-capped gold nanoparticles in tetradecane in microgravity during a temperature drop. The corresponding apparent hydrodynamic diameters d_H are calculated using the temperature evolution T, the viscosity η, and the refractive index n of the solvent (see **Table 2**) From Pyttlik *et al.*, **2022**.[196]

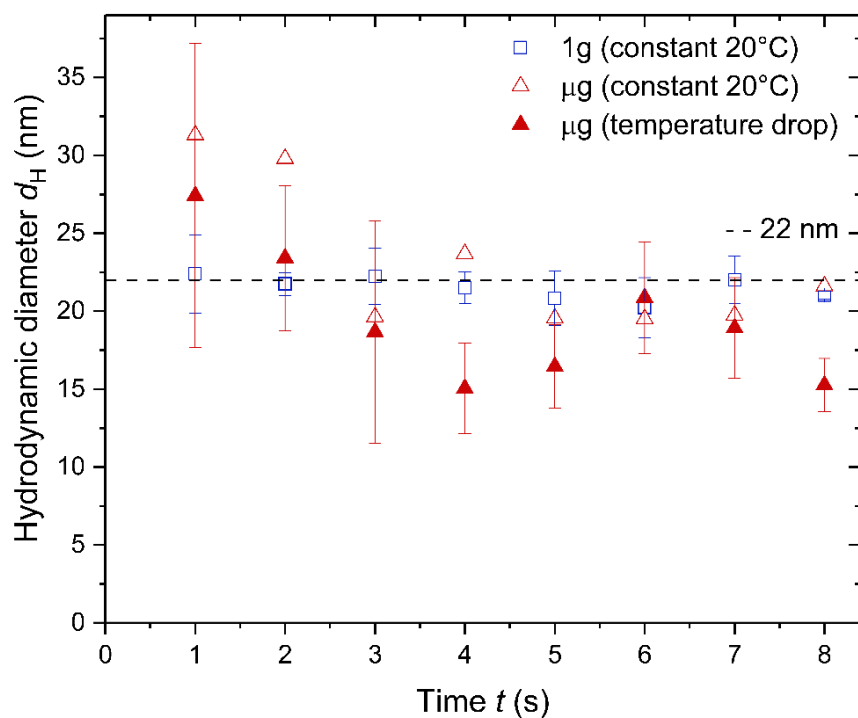| t (s)	τ_{Diff} (ms)	d_H (nm)	T (°C)	η (mPas s)	n
1	0.10	27 (± 10)	94 (± 26)	0.73	1.3948
2	0.14	23 (± 5)	62 (± 13)	1.11	1.4090
3	0.13	19 (± 7)	53 (± 21)	1.27	1.4130
4	0.11	15 (± 3)	51 (± 10)	1.31	1.4139
5	0.13	16 (± 3)	47 (± 9)	1.39	1.4156
6	0.17	21 (± 4)	45 (± 9)	1.44	1.4165
7	0.15	19 (± 3)	46 (± 9)	1.42	1.4161
8	0.13	15 (± 2)	43 (± 6)	1.49	1.4174

Figure 30: Hydrodynamic diameter d_H over time t of oleylamine-capped gold nanoparticles in tetradecane. Three experiments were performed on the ground at a constant temperature of 20 °C. The average hydrodynamic diameter and the standard deviation are shown. One experiment was performed in microgravity with a constant temperature of 20 °C. Two experiments in microgravity with a temperature drop (70 °C to 10 °C) were performed, the average hydrodynamic diameter and corresponding uncertainties estimated by error propagation are shown. At d_H = 22 nm a dashed blacked line is shown to guide the eye. From Pyttlik *et al.*, **2022**.[196]

3.3   Agglomerating system

The results of the following chapter have been published in the course of this project in "Microgravity Removes Reaction Limits from Nonpolar Nanoparticle Agglomeration" by Pyttlik, Kuttich and Kraus in *Small* in **2022**.[274]

To investigate the effect of microgravity on the agglomeration process of gold nanoparticles, their agglomeration process was followed by DLS measurements on ground and in microgravity. As agglomerating system, hexadecanethiol-capped gold nanoparticles in tetradecane were used. By performing a drop experiment, microgravity duration of 4.7 s allows the recording of 4 consecutive autocorrelation functions. A catapult launch extended microgravity to 9.3 s allowing the record of 8 consecutive autocorrelation functions. The gold nanoparticles had a core diameter of d_{Core} = 7.8 nm (± 0.5 nm) and a hydrodynamic diameter of d_H =13 nm (±1 nm). It is worth noticing that the hydrodynamic diameter of the hexadecanethiol-capped gold nanoparticles was smaller than the hydrodynamic diameter of the oleylamine-capped gold nanoparticles, even though both ligands had a similar ligand length of 2 nm. Due to the strong bonding of the thiol-group on the gold surface, it is assumed that only a single layer shell is formed,[275,276] in contrast to the formation of oleylamine multilayers, see **Chapter 3.2.2**. Gold nanoparticles with two different concentrations were investigated to study the effect of the concentration on the agglomeration of the particles, a low particle concentration (c = 1.03 ± 0.12 mg mL^{-1} on ground and c = 0.86 ± 0.16 mg mL^{-1} in microgravity) and a high particle concentration (c = 2.75 ± 0.04 mg mL^{-1} on ground and c = 3.27 ± 0.79 mg mL^{-1} in microgravity) were used.

3.3.1 Determination of the agglomeration temperature

As prerequisite to evaluate data of the agglomerating system, the exact agglomeration temperature was determined. The agglomeration temperature of the hexadecanethiol-capped gold nanoparticles with a core diameter of d_{Core} = 7.8 nm (± 0.5 nm) and a hydrodynamic diameter of d_H = 13 nm (± 1 nm) in tetradecane was determined by SAXS and DLS measurements. For SAXS measurements, the sample was first heated to 80 °C, then cooled to 10 °C, and subsequently reheated to 80 °C. Scattering data were recorded every 5 K (selected scattering data are shown in **Figure 31**). All recorded scattering data are shown in

Figure 53 (appendix). At 60 °C, a structure peak can be seen at a scattering vector of $\vec{q}$ = 0.07 Å^{-1} indicating the onset of the particle agglomeration. The agglomeration fraction χ_{Agglo} was determined as described in **Chapter 2.2**.

DLS measurements were recorded at every 5 K between 70 °C and 10 °C, and every measurement was repeated two times. The averaged hydrodynamic diameter and the agglomeration fraction are shown in **Figure 32**. At 70 °C, the nanoparticles were completely deagglomerated and a hydrodynamic diameter of d_{H} = 13 nm (± 1 nm) was found. An increasing hydrodynamic diameter and agglomeration fraction was found at 60 °C, determining an agglomeration temperature of T_{Agglo} = 60 °C of the gold nanoparticle sample (see **Figure 31**). The agglomeration fraction of the nanoparticles increased during the cooling of the sample, until the particles were completely agglomerated (χ_{Agglo} = 1) and decreased as soon as the sample was reheated again, until the particles were completely deagglomerated (χ_{Agglo} = 0).[97] To avoid any premature agglomeration of the nanoparticles before the agglomeration experiments, the sample was heated to 70 °C inside the aluminum block before the sample was injected into the pre-cooled measurement cell (see **Figure 12**) to induce agglomeration.
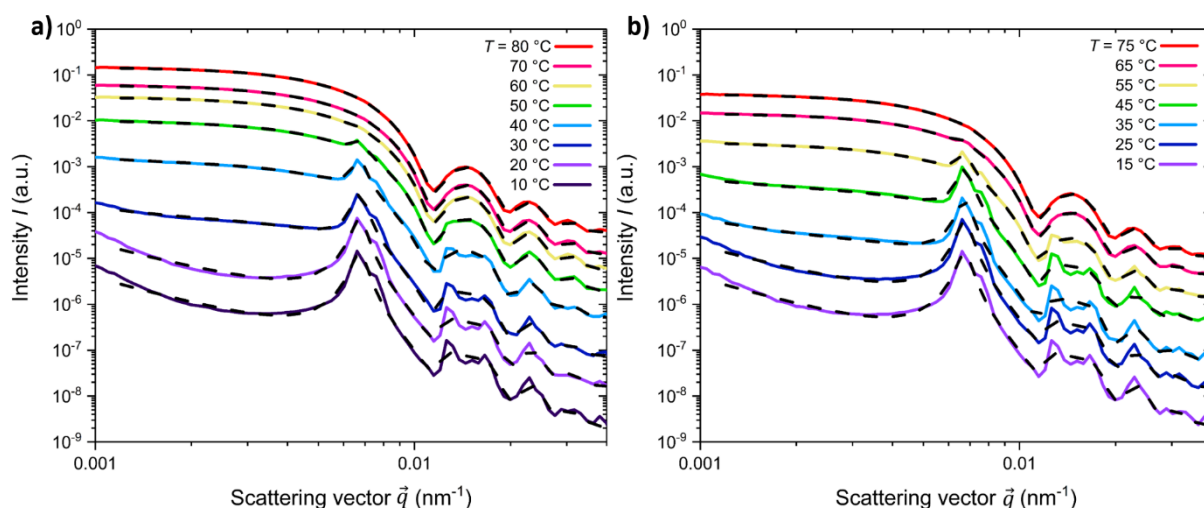
Figure 31: Selected scattering data (colored, solid lines) of hexadecanethiol-capped gold nanoparticles in tetradecane at different temperatures and the corresponding fits (black, dashed line), see **Chapter 2.2**. The particles had a core diameter of 7.8 nm (± 0.5 nm). The curves are shifted vertically to avoid overlapping of the data and improve readability. a) Evolution of scattering intensity during cooling from 80 °C to 10 °C in steps of 5 K. b) Evolution of scattering intensity during reheating from 10 °C to 80 °C in steps of 5 K. Published in the course of this project in "Microgravity Removes Reaction Limits from Nonpolar Nanoparticle Agglomeration" by Pyttlik, Kuttich and Kraus in *Small*, in **2022**.[274]
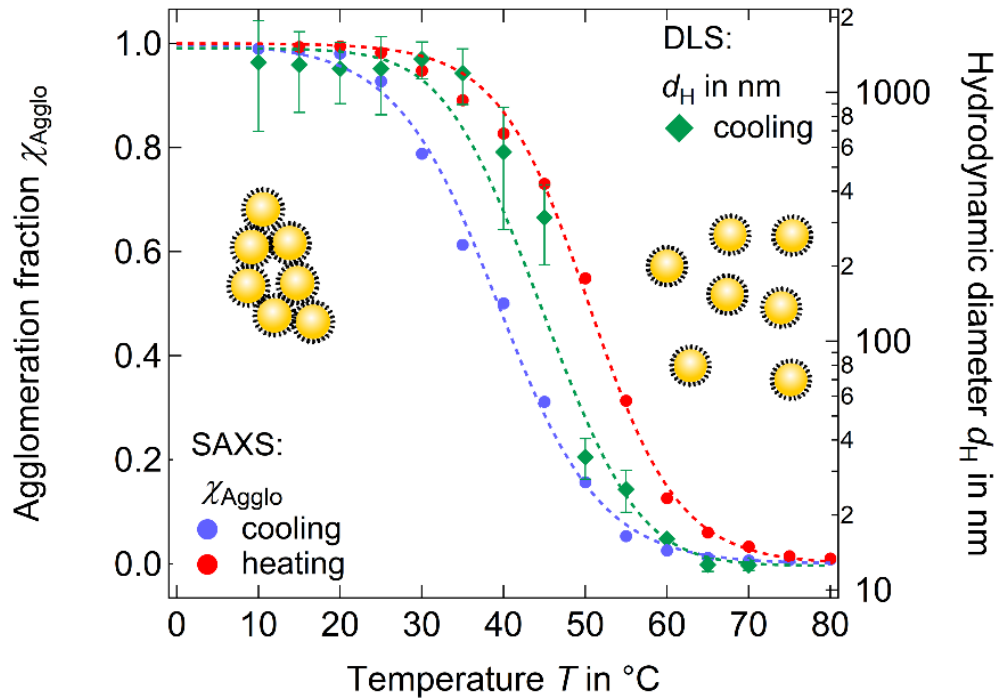
Figure 32: Agglomeration χ_{Agglo} fraction (left axis) and hydrodynamic diameter d_H (right axis) of hexadecanethiol-capped gold nanoparticles in tetradecane. The agglomeration fraction was obtained from SAXS measurements by recording data during the cooling of the nanoparticles from 80 °C to 10 °C and reheating them to 80 °C. DLS measurements were performed during the cooling of the nanoparticles from 70 °C to 10 °C. DLS measurements were repeated two times, the averaged hydrodynamic diameters d_H and the corresponding standard deviations are shown. Dashed lines are inserted to guide the eye. From Pyttlik *et al.*, **2022**.[274]

3.3.2 Ground experiments with the agglomerating system

DLS measurements were carried out with the agglomerating system on ground and later compared to the measurement performed in microgravity to investigate the influence of microgravity on the agglomeration process of gold nanoparticles. On ground and in microgravity, experiments were performed with two different particle concentrations.

To induce the agglomeration of the gold nanoparticles, the dispersion was heated to 70 °C and injected into the hot aluminum block (70 °C) by using a syringe pump. The sample was kept in the aluminum block for 90 min to simulate identical conditions on ground, compared to the experiments in the drop tower. Afterwards, the sample was injected into the pre-cooled measurement cell. The DLS measurements were started as soon as the injection of the sample was completed. A schematic overview of the induction of the agglomeration process is shown in **Figure 33**.
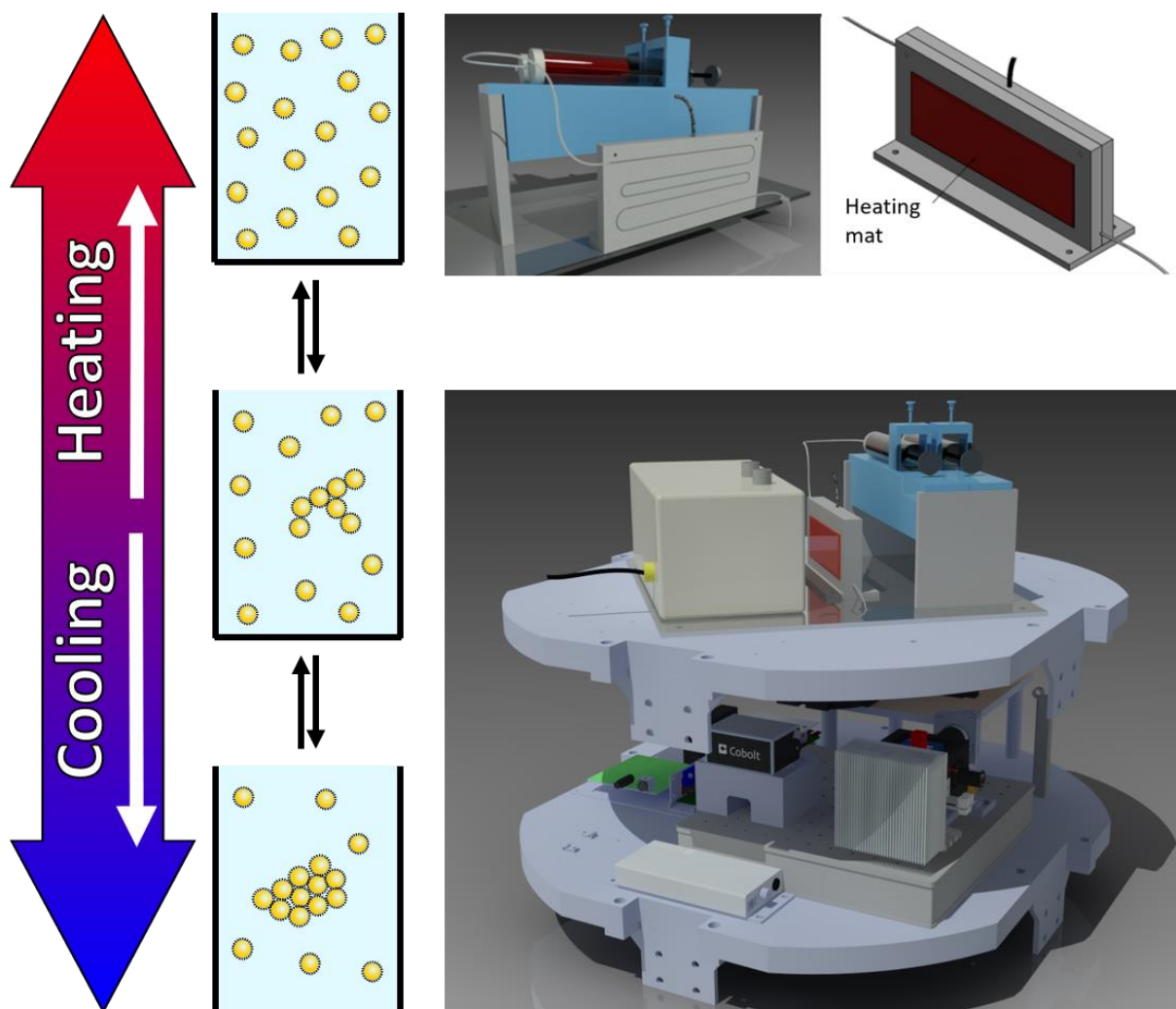
Figure 33: Schematic overview of the instrumental set-up to be able to induce the temperature dependent agglomeration process of gold nanoparticles.

Gold nanoparticles with a core diameter of d_{Core} = 7.8 nm, capped with hexadecanethiol in tetradecane were used. One dispersion with a gold concentration of c = 1.03 mg mL^{-1}, corresponding to a particle concentration of 2.12×10^{14} mL^{-1}, and another dispersion with a gold concentration of c = 2.75 mg mL^{-1}, corresponding to a particle concentration of 5.66×10^{14} mL^{-1}, was used. Measurements were performed with a temperature drop (70 °C to 10 °C). Agglomerating experiments with the lower gold concentration were repeated three times, and two times with the higher concentration.

During each DLS measurement, eight consecutive autocorrelation functions, with an integration time of 1 s were recorded. The recorded autocorrelation functions of one measurement for each used particle concentration are shown in **Figure 34**. To improve the readability of the data, the autocorrelation functions recorded after t = 2 s are shifted along

the y-axis. All recorded autocorrelation functions are shown in the appendix (see **Figure 59** and **Figure 60**). To analyze the recorded data, the approach introduced by Weitz *et al.* was followed. They used a single mono-exponential function to describe the optical scattering of an agglomerating system, showing that the attractive interactions between the agglomerating particles and the growth of the agglomerates during the integration time can be neglected in the data analysis, and reliable estimates of the averaged agglomerate sizes were obtained.[277,278] Autocorrelation functions recorded on ground are well described by **Equation (30)**. The data obtained finally demonstrate that it was possible to follow the agglomeration process by DLS measurements by recording reliable autocorrelation functions with an integration time of only 1 s during a rapid temperature drop induced by the liquid handling system. The obtained mean residence times τ_{Diff} were used to calculate the hydrodynamic diameter d_H by using the calculated temperatures for the temperature drop according to **Table 2**. The results are summarized in **Table 4** and shown in **Figure 35**.
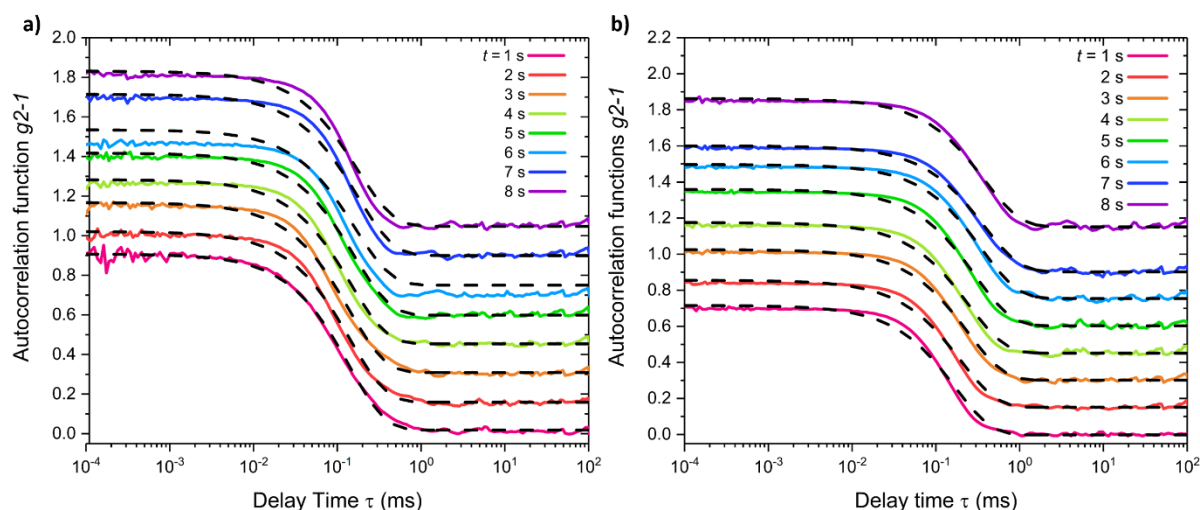
Figure 34: Autocorrelation functions (colored, solid lines) and the corresponding fits (black, dashed lines) recorded during the agglomeration of hexadecanethiol-capped gold nanoparticles in tetradecane on ground with a temperature drop (70 °C to 10 °C). The autocorrelation functions recorded after $t = 2$ s are shifted along the y-axis to improve readability. a) At a gold concentration of $c = 1.03$ mg mL^{-1} ($\pm$ 0.12 mg mL^{-1}). b) At a gold concentration of $c = 2.75$ mg mL^{-1} ($\pm$ 0.04 mg mL^{-1}). Modified from Pyttlik *et al.*, **2022**.[274]

Table 4: Time-dependent mean residence times τ_{Diff} and the corresponding apparent hydrodynamic diameters d_H of the gold nanoparticles during the agglomeration process of hexadecanethiol-capped gold nanoparticles in tetradecane on ground (1 g). The agglomeration process was initiated by rapid cooling of the sample (from 70 °C to 10 °C). From Pyttlik *et al.*, **2022.**[274]

c (mg mL⁻¹)	τ_{Diff} (ms)		d_H (nm)	
	1.03 (± 0.12)	2.75 (± 0.04)	1.03 (± 0.12)	2.75 (± 0.04)
t (s)				
1	0.30 (± 0.03)	0.51 (± 0.24)	83 (± 30.9)	139 (± 81.3)
2	0.32 (± 0.03)	0.40 (± 0.01)	53 (± 12.0)	66 (± 13.2)
3	0.32 (± 0.04)	0.39 (± 0.13)	46 (± 18.6)	56 (± 28.1)
4	0.32 (± 0.03)	0.42 (± 0.10)	43 (± 9.2)	58 (± 17.9)
5	0.34 (± 0.03)	0.51 (± 0.11)	43 (± 7.8)	65 (± 17.7)
6	0.34 (± 0.01)	0.61 (± 0.14)	42 (± 7.3)	75 (± 21.1)
7	0.36 (± 0.01)	0.67 (± 0.11)	46 (± 8.0)	85 (± 19.7)
8	0.35 (± 0.01)	0.71 (± 0.07)	41 (± 4.7)	83 (± 12.3)
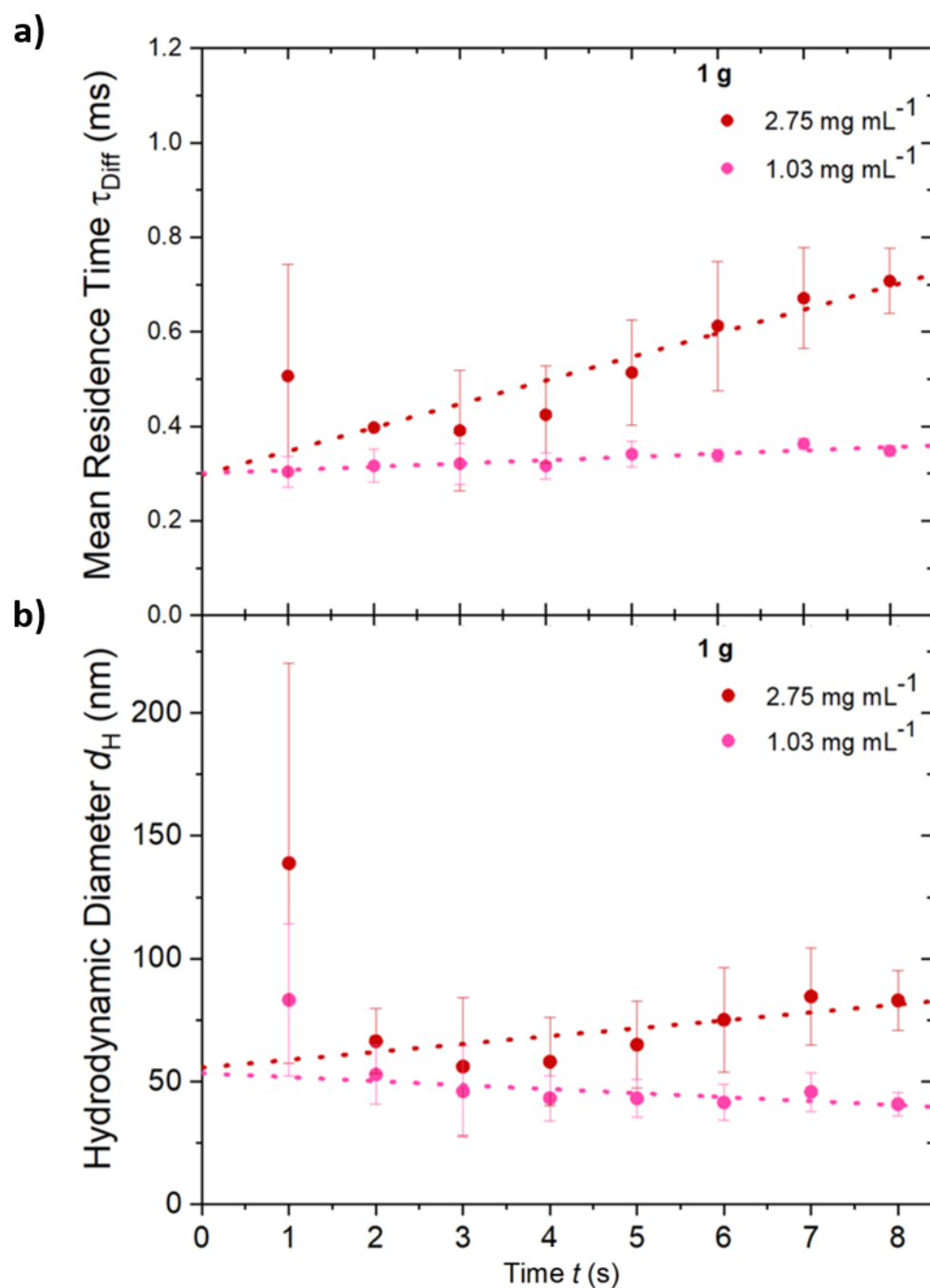
Figure 35: a) Comparison of averaged mean residence times τ_{Diff} and the corresponding standard deviations of hexadecanethiol-capped gold nanoparticles in tetradecane during the agglomeration process of the particles. b) Comparison of averaged apparent hydrodynamic diameter d_H and the corresponding error standard deviations of hexadecanethiol-capped gold nanoparticles in tetradecane during the agglomeration process of the particles. The agglomeration was induced by rapid cooling of the sample (70 °C to 10 °C). Modified from Pyttlik *et al.*, **2022**.[274]

For the measurements at t = 1 s (see **Table 4**), the largest mean residence times and thus the largest hydrodynamic diameters were found for both concentrations. Furthermore, in both cases large standard deviations were observed. However, for a cooling and agglomerating system the smallest mean residence times and hydrodynamic diameters were expected for the first measurements. We attribute these unexpected findings to convection forces directly after injecting the hot sample into the precooled measurement, cell preventing the collection of reliable data at these particular data points. Consequently, data collected at t = 1 s were not considered for any of the following discussions.

For the low particle concentration measurements (c = 1.03 mg mL^{-1}), the size of the agglomerates stayed almost constant during the observation period (t = 2 s - 8 s). The averaged hydrodynamic diameter was determined as d_H = 41 nm (± 4.7 nm). Two differences were observed for the measurements with increasing the concentration by a factor of 2.7 (c = 2.75 mg mL^{-1}). First, during the observation time a constant growth of the agglomerates could be observed instead of constant sizes determined during the low concentration experiments, see **Figure 35**. Second, the size of the observed agglomerates was approximately doubled. At t = 8 s a hydrodynamic diameter of d_H = 83 nm (± 12.3 nm) was found.

3.3.3 Microgravity experiments with the agglomerating system

To investigate the influence of gravity on the agglomeration of gold nanoparticles, the agglomeration process of hexadecanethiol-capped gold nanoparticles in tetradecane was followed by DLS measurements. In analogy to the ground experiments, measurements were performed with two different particle concentrations. Microgravity conditions were realized in the drop tower in Bremen by performing a catapult launch or a simple drop experiment.

For following the agglomeration of the gold nanoparticles in microgravity, the instrumental set-up was integrated into the drop tower capsule, see **Figure 13**. To induce the agglomeration of the system the same moment the instrumental set-up enters microgravity, the dispersion was first heated to 70 °C and injected into the hot aluminum block (preheated to 70 °C) by using a syringe pump. The sample was kept in the aluminum block for 90 min, until the drop capsule was placed inside the drop tower and the tower was completely evacuated. Afterwards, the sample was injected into the pre-cooled measurement cell. As soon as the injection of the sample was completed, the capsule entered microgravity and the DLS

measurements were started. A schematic overview of the induction of the agglomeration process is shown in **Figure 33**.

3.3.3.1 Microgravity experiments with the agglomerating system after a catapult launch

First experiments in microgravity were performed with a catapult launch, providing a microgravity duration of 9.1 s. Considering the delay time of 100 ms between the recording of the single autocorrelation functions, 8 consecutive autocorrelation functions with an integration time of 1 s could be recorded.

Gold nanoparticles with a core diameter of d_{Core} = 7.8 nm, capped with hexadecanethiol in tetradecane were used for the microgravity experiments. Again, two dispersions with different concentrations were investigated. For the lower concentrated sample, the concentration was c = 0.86 mg mL^{-1}, corresponding to a particle concentration of 1.62x10^{14} mL^{-1}. Secondly, a dispersion with a gold concentration of c = 3.27 mg mL^{-1}, corresponding to a particle concentration of 6.16x10^{14} mL^{-1} was used. Measurements were performed with a temperature drop (70 °C to 10 °C). Agglomerating experiments with the lower gold concentration were repeated four times and two times with the higher concentration.

During each DLS measurement, eight consecutive autocorrelation functions with an integration time of 1 s were recorded. The recorded autocorrelation functions of one measurement for each used particle concentration are shown in **Figure 36**. To improve the readability of the data, the autocorrelation functions recorded after t = 2 s are shifted along the y-axis. All recorded autocorrelation functions are shown in the appendix (see **Figure 61** and **Figure 62**). To analyze the recorded data, the approach introduced by Weitz *et al.* was followed. They used a single mono-exponential function to describe the optical scattering of an agglomerating system.[277,278] Autocorrelation functions recorded in microgravity after a catapult launch after t = 2 s are well described by **Equation (30)**. At t = 1 s, the influence on the catapult launch could be clearly observed during the measurement, as can be seen at the compromised shape of the autocorrelation function at t = 1 s (see **Figure 36**). Consequently, no accurate mean residence time τ_{Diff} could be obtained for t = 1 s. The obtained mean residence times τ_{Diff} were used to calculate the hydrodynamic diameter d_H by using the

calculated temperatures for the temperature drop according to **Table 2**. The results are summarized in **Table 5** and shown in **Figure 37**.
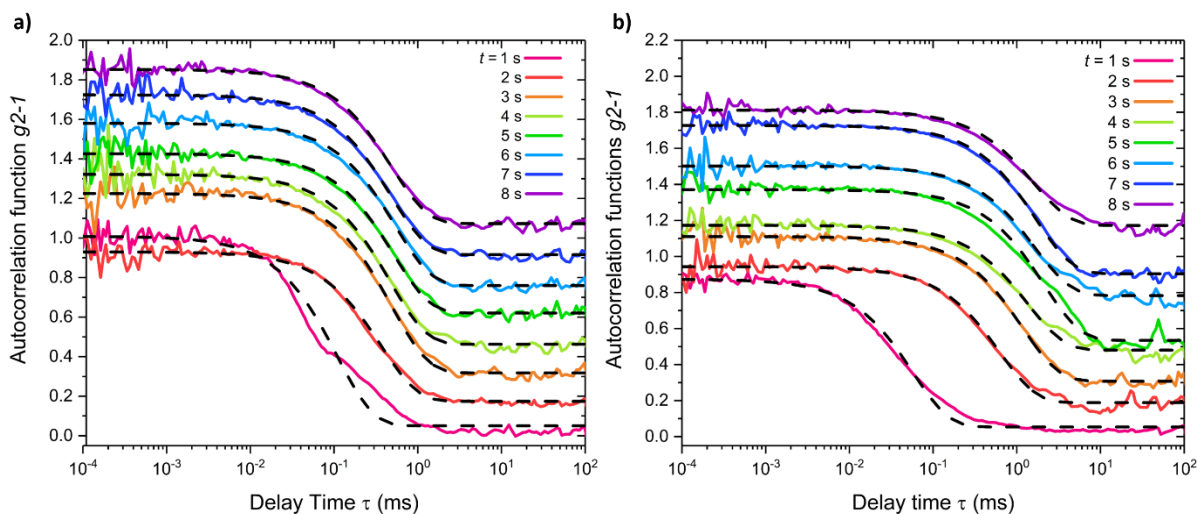
Figure 36: Autocorrelation functions (colored, solid lines) and the corresponding fits (black, dashed lines) recorded during the agglomeration of hexadecanethiol-capped gold nanoparticles in tetradecane in microgravity with a temperature drop (70 °C to 10 °C) after a catapult launch. The autocorrelation functions recorded after $t = 2$ s are shifted along the y-axis to improve readability. a) At a gold concentration of $c = 0.86$ mg mL^{-1} ($\pm$ 0.16 mg mL^{-1}). b) At a gold concentration of $c = 3.27$ mg mL^{-1} ($\pm$ 0.79 mg mL^{-1}). Modified from Pyttlik *et al.*, **2022**.[274]

Table 5: Time-dependent mean residence times τ_{Diff} and the corresponding apparent hydrodynamic diameters d_H of the gold nanoparticles during the agglomeration process of hexadecanethiol-capped gold nanoparticles in tetradecane in microgravity (μ g), after a catapult launch. The agglomeration process was initiated by rapid cooling of the sample (from 70 °C to 10 °C). From Pyttlik *et al.*, **2022**.[274]

c (mg mL^{-1})	τ_{Diff} (ms)		d_H (nm)	
	0.86 (± 0.16)	3.27 (± 0.79)	0.86 (± 0.16)	3.27 (± 0.79)
t (s)				
1	0.19 (± 0.009)	0.21 (± 0.14)	52 (± 29.9)	58 (± 43.3)
2	0.67 (± 0.14)	1.53 (± 0.37)	111 (± 32.0)	255 (± 80.5)
3	1.04 (± 0.21)	2.68 (± 0.45)	149 (± 64.2)	385 (± 160.4)
4	1.32 (± 0.27)	3.18 (± 0.63)	181 (± 50.8)	434 (± 120.1)
5	1.33 (± 0.28)	3.84 (± 0.60)	168 (± 44.5)	485 (± 109.7)
6	1.33 (± 0.20)	3.48 (± 0.22)	163 (± 37.3)	427 (± 77.9)
7	1.10 (± 0.30)	3.06 (± 0.49)	139 (± 44.8)	385 (± 90.1)
8	0.84 (± 0.36)	3.22 (± 0.04)	98 (± 43.4)	377 (± 42.4)
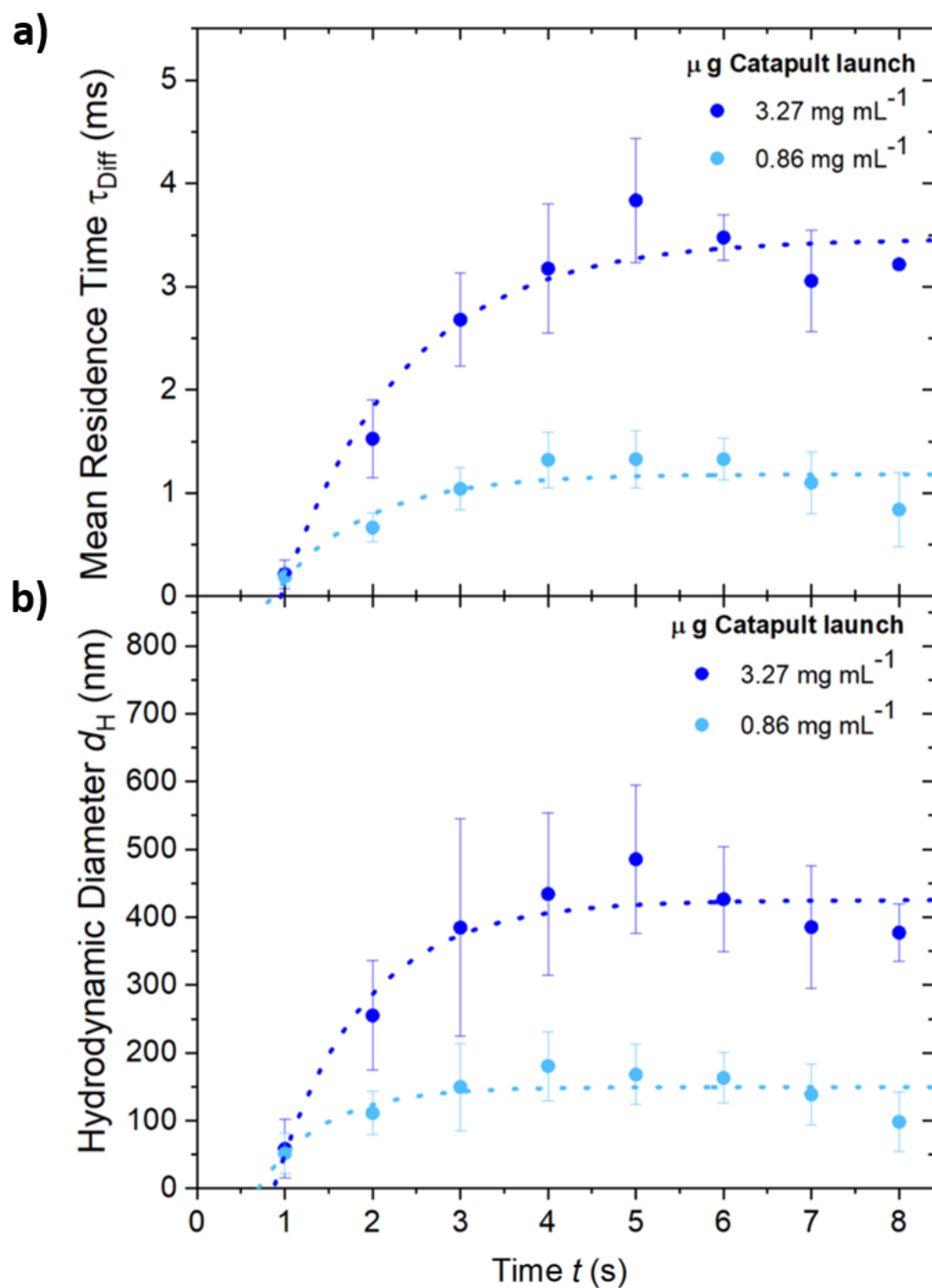
Figure 37: a) Comparison of averaged mean residence times τ_{Diff} and the corresponding standard deviations of hexadecanethiol-capped gold nanoparticles in tetradecane during the agglomeration process of the particles. b) Comparison of averaged apparent hydrodynamic diameter d_H and the corresponding error propagation of hexadecanethiol-capped gold nanoparticles in tetradecane during the agglomeration process of the particles. The agglomeration was induced by rapid cooling of the sample (70 °C to 10 °C). Modified from Pyttlik *et al.*, **2022**.[274]

In microgravity, for both concentrations ($c = 0.86$ mg mL^{-1} and $c = 3.27$ mg mL^{-1}) a growth could be monitored during the first four seconds of the measurement period before the size of the agglomerates stagnated. For the measurements with lower particle concentration significantly smaller agglomerates ($d_H = 98$ nm ($\pm$ 43.4nm) at t = 8 s) were observed compared to the high concentration experiments ($d_H = 377$ nm ($\pm$ 42.4nm) at t = 8 s). Generally, by increasing the particle concentration by a factor of 3.8 the size of the agglomerates also increased by a factor of 3.8.

3.3.3.2 Microgravity experiments with the agglomerating system after a drop

To investigate if the catapult launch has an influence on the agglomeration process of gold nanoparticles, the agglomeration was followed during a simple drop experiment. During the catapult launch, the experimental set-up was accelerated by approximately 30 g.[266] To ensure that this impact did not influence the recorded measurements, the experiment was repeated by performing a drop experiment, where the experimental set-up was slowly pulled up to the top of the tower and gently released. Additionally, this experiment should substantiate the assumption that the compromised shape of the autocorrelation function for the measurements at $t = 1$ s observed for the launch experiments can be attributed to physical impact of the catapult launch (compare **Chapter 3.3.3.1** and **Figure 36**). In analogy to the launch experiments, the agglomeration and measurement process was initiated via the liquid handling system. The drop capsule was released after the liquid injection was finalized and the recording of the DLS measurements started. A drop experiment provides a microgravity duration of 4.7 s. Considering the delay time between the recording of single autocorrelation functions of 100 ms, four consecutive autocorrelation functions with an integration time of 1 s were recorded.

Gold nanoparticles with a core diameter of $d_{Core} = 7.8$ nm, capped with hexadecanethiol in tetradecane were used. The dispersion had a gold concentration of $c = 2.67$ mg mL^{-1} (particle concentration of 5.03×10^{14} mL^{-1}) and the measurement was performed with the temperature drop of 70 °C to 10 °C. During the DLS measurement, four consecutive autocorrelation functions, with an integration time of 1 s, were recorded. The recorded autocorrelation functions are shown in **Figure 38**. To improve the readability of the data, the autocorrelation functions recorded after $t = 2$ s are shifted along the y-axis. The original recorded

autocorrelation functions are shown in the appendix (see **Figure 63**). To analyze the recorded data, the approach introduced by Weitz *et al.* was followed. They used a single mono-exponential function to describe the optical scattering of an agglomerating system.[277,278] Autocorrelation functions recorded in microgravity after a drop are well described by **Equation (30)**. The obtained mean residence times τ_{Diff} were used to calculate the hydrodynamic diameter d_H by using the calculated temperatures for the temperature drop according to **Table 2**. The results are summarized in **Table 5** and shown in **Figure 39**. It can be clearly seen that the measurement at $t = 1$ s is unperturbed during the drop experiment, indeed speaking for physical stresses of the launch acceleration as source of compromised autocorrelation functions during the launch experiments (compare **Chapter 3.3.1** and **Figure 36**). Overall, it was shown that the obtained mean residence times and hydrodynamic diameter observed after a catapult launch were in good agreement with what was observed during the drop experiment. These findings clearly indicate that the catapult launch only influenced the recording of the autocorrelation function at $t = 1$ s, while the other measurements were not impacted.
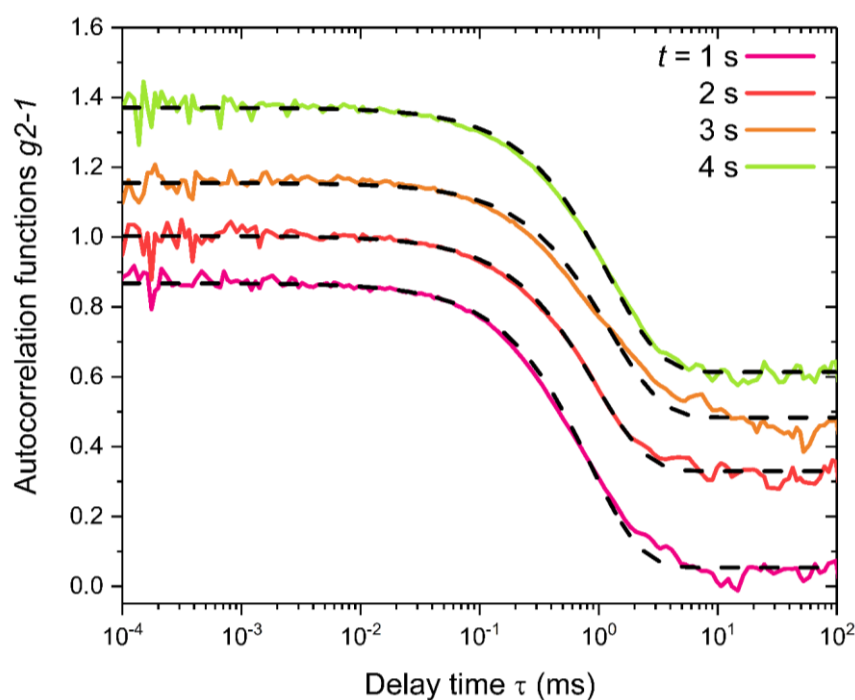
Figure 38: Autocorrelation functions (colored, solid lines) and the corresponding fits (black, dashed lines) recorded during the agglomeration process of hexadecanethiol-capped gold nanoparticles in tetradecane in microgravity by performing a drop experiment. A sample with a gold concentration of $c = 2.67$ mg mL^{-1} was used. The autocorrelation functions recorded at $t = 2$ s, 3 s and 4 s are shifted along the y-axis to improve readability. Modified from Pyttlik *et al.*, **2022**.[274]

Table 6: Time-dependent mean residence times τ_{Diff} and the corresponding apparent hydrodynamic diameters d_H of the gold nanoparticles during the agglomeration process of hexadecanethiol-capped gold nanoparticles in tetradecane in microgravity (µ g), after a drop. The agglomeration process was initiated by rapid cooling of the sample (from 70 °C to 10 °C). From Pyttlik *et al.*, **2022**.[274]

	τ_{Diff} (ms)			d_H (nm)		
	catapult launch		*drop*	*catapult launch*		*drop*
c (mg mL^{-1})	0.86 (± 0.16)	3.27 (± 0.79)	2.67	0.86 (± 0.16)	3.27 (± 0.79)	2.67
t (s)						
1	0.19 (± 0.009)	0.21 (± 0.14)	1.68 (± 0.03)	52 (± 29.9)	58 (± 43.3)	416 (± 164.0)
2	0.67 (± 0.14)	1.53 (± 0.37)	1.89 (± 0.04)	111 (± 32.0)	255 (± 80.5)	316 (± 63.4)
3	1.04 (± 0.21)	2.68 (± 0.45)	2.51 (± 0.07)	149 (± 64.2)	385 (± 160.4)	360 (± 137.7)
4	1.32 (± 0.27)	3.18 (± 0.63)	2.43 (± 0.05)	181 (± 50.8)	434 (± 120.1)	332 (± 64.4)
5	1.33 (± 0.28)	3.84 (± 0.60)	/	168 (± 44.5)	485 (± 109.7)	/
6	1.33 (± 0.20)	3.48 (± 0.22)	/	163 (± 37.3)	427 (± 77.9)	/
7	1.10 (± 0.30)	3.06 (± 0.49)	/	139 (± 44.8)	385 (± 90.1)	/
8	0.84 (± 0.36)	3.22 (± 0.04)	/	98 (± 43.4)	377 (± 42.4)	/

Figure 39: a) Comparison of averaged mean residence times τ_{Diff} and the corresponding standard deviations of hexadecanethiol-capped gold nanoparticles in tetradecane during the agglomeration process of the particles. b) Comparison of averaged apparent hydrodynamic diameter d_H and the corresponding error propagation of hexadecanethiol-capped gold nanoparticles in tetradecane during the agglomeration process of the particles. The agglomeration was induced by rapid cooling of the sample (70 °C to 10 °C). Modified from Pyttlik et al., **2022**.[274]

3.3.4 Interpretation of the gravitational influence on agglomeration

In summary, we were able to show that the set-up developed during this project indeed allows to study the agglomeration process of gold nanoparticles in microgravity for the first time by collecting valid DLS data in the ZARM drop tower in Bremen. Agglomeration of thiol-capped gold nanoparticles was induced with the designed liquid handling system, and analogous data was recorded on ground and in microgravity. In both cases, dispersions with two particle concentrations were studied for comparison.

On ground, samples with a concentration $c = 1.03$ mg mL^{-1} (± 0.12 mg mL^{-1}) and $c = 2.75$ mg mL^{-1} (± 0.04 mg mL^{-1}) were analyzed. Corresponding microgravity measurements were carried out with $c = 0.86$ mg mL^{-1} (± 0.16 mg mL^{-1}) and $c = 3.27$ mg mL^{-1} (± 0.79 mg mL^{-1}). Slight deviations in the particle concentration date back to the sample injection process. During the injection of the hot sample from the aluminum block into the pre-cooled measurement cell, the sample had to pass room temperature warm plastic tubes resulting in an uncontrolled sticking of the particles inside the tube. This effect impeded a precise control of the particle concentration inside the measurement cell. Consequently, it was impossible to guarantee exactly identical particle concentrations on ground and in microgravity. However, the particle concentration was sufficiently similar to provide comparable data for ground and microgravity experiments.

A catapult launch provides a microgravity interval of 9.1 seconds, which was sufficient to record 8 autocorrelation functions. On ground and when performing a catapult launch, the first recorded sets of data at $t = 1$ s were not evaluable. On ground, this measurement was indicating shrinking agglomerates, which is not plausible. Additionally, large standard deviations were observed for that measurement at $t = 1$ s. We attributed both those effects on ground to convection induced by the liquid handling system that disturbs reliable data collection. On the other hand, in microgravity, compromised autocorrelation functions during the launch experiments were found at $t = 1$ s when performing a catapult launch, presumably due to acceleration forces. To test both hypotheses, a simple drop experiment was performed in microgravity. During that experiment, neither the convection forces assumed to disturb the ground measurement, nor the acceleration forces of the catapult launch were present. Indeed, at $t = 1$ s the autocorrelation function and the fit during the drop experiment were perfectly aligned.

3. Results and Discussions

A comparison of the recorded autocorrelation functions recorded on ground and in microgravity is shown in **Figure 40**. To improve the display of the autocorrelation functions, the functions recorded after $t = 2$ s are shifted along the y-axis.
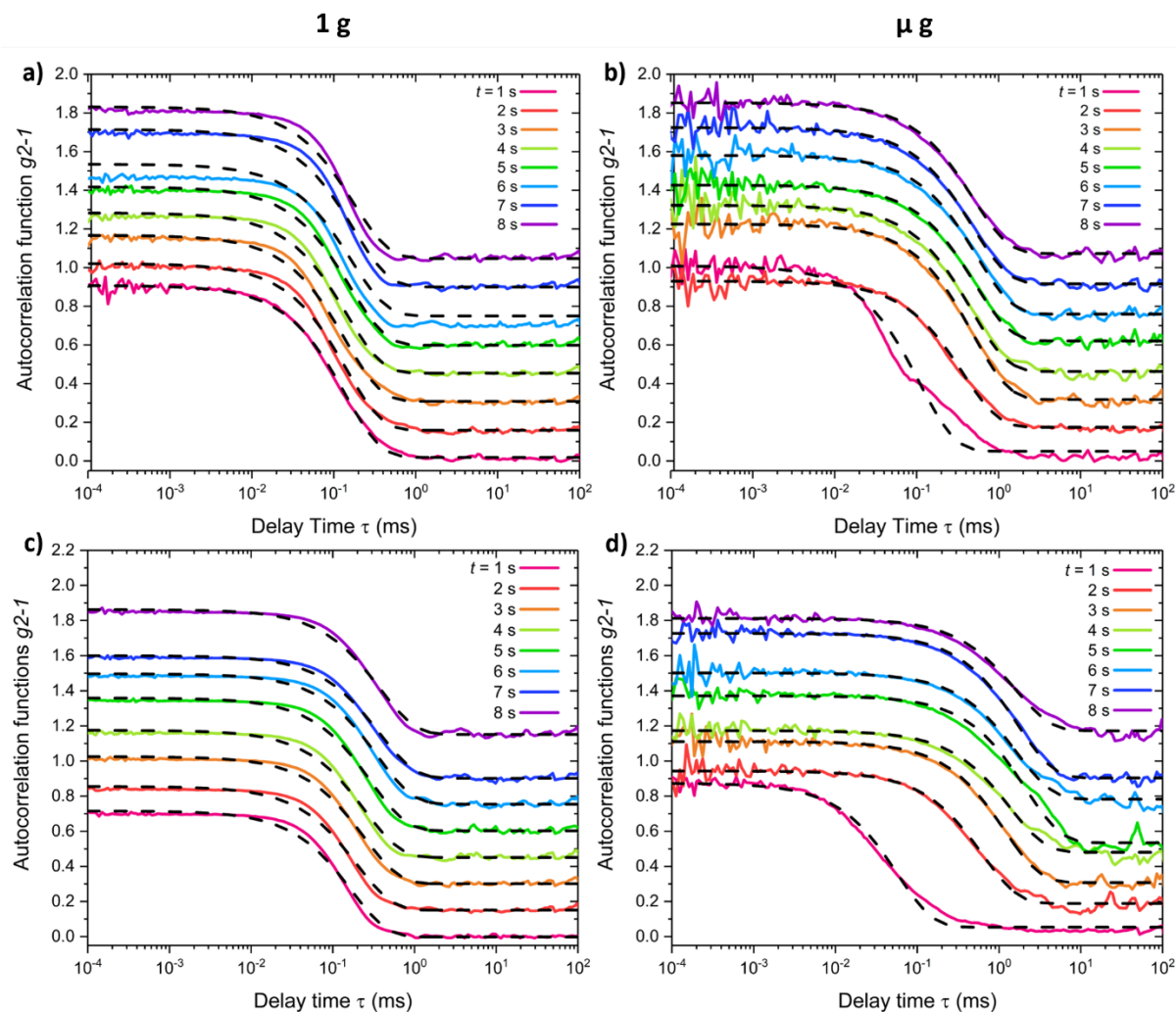
Figure 40: Autocorrelation functions (colored, solid lines) and the corresponding fits (black, dashed lines) recorded during the agglomeration process of hexadecanethiol-capped gold nanoparticles in tetradecane. The autocorrelation functions recorded after $t = 2$ s, are shifted along the y-axis to improve readability. a) Measurements on ground at a gold concentration of $c = 1.03$ mg mL-1 (± 0.12 mg mL-1). b) Measurements in microgravity at a gold concentration of $c = 0.86$ mg mL-1 (± 0.16 mg mL-1). c) Measurements on ground at a gold concentration of c = 2.75 mg mL-1 (± 0.04 mg mL-1). d) Measurements in microgravity at a gold concentration of c = 3.27 mg mL-1 (± 0.79 mg mL-1). Modified from Pyttlik *et al.*, **2022**.[274]

Both, on ground and in microgravity, the recorded autocorrelation functions can be described by using **Equation (30)**. A comparison of the used fit function shows a perfect match for the data recorded in microgravity, whereas on ground a more stretched mono-exponential fit was

found (see **Figure 40**). These findings indicate the formation of more uniform agglomerates with a more monodisperse size distribution in microgravity compared to those formed on ground.

A direct comparison of selected autocorrelation functions on ground and in microgravity is shown in **Figure 41**. The decay of the autocorrelation functions recorded in microgravity was slower, indicating larger mean residence times τ_{Diff}, slower diffusion of the particles, and larger hydrodynamic diameters. The obtained corresponding hydrodynamic diameters are analyzed and discussed in **Chapter 3.2.3**.

Fitting the recorded autocorrelation functions with **Equation (30)** yielded the average mean residence times τ_{Diff}. **Equation (32)** provides the corresponding apparent hydrodynamic diameters d_H for temperatures T, refractive indices n, and dynamic viscosities η summarized in **Table 2**. The mean residence times τ_{Diff} obtained on ground and in microgravity are summarized in **Table 7** and the corresponding apparent hydrodynamic diameters d_H are displayed in **Table 8**. A comparison is shown in **Figure 42**.
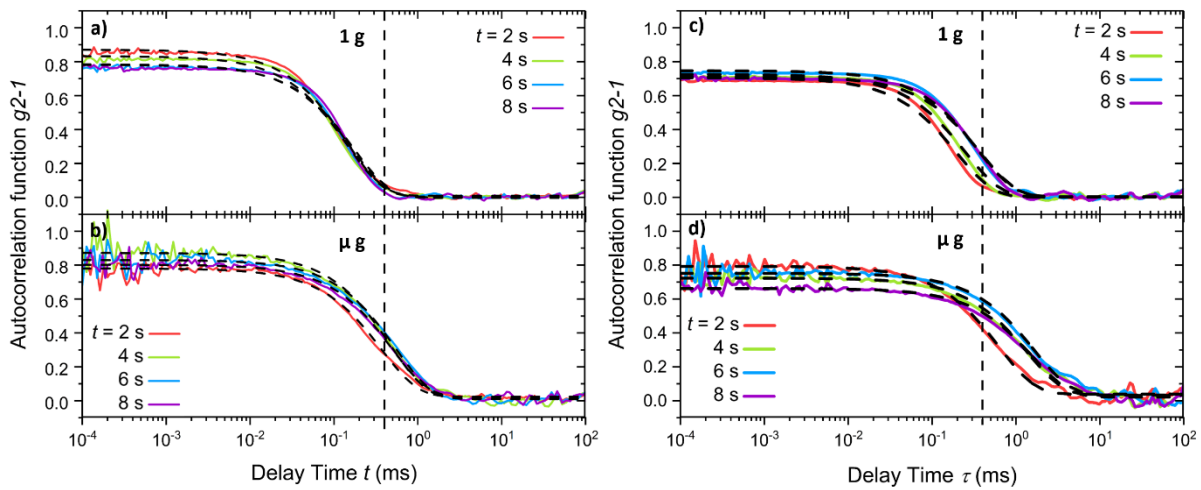

Figure 41: Selected autocorrelation functions (colored, solid lines) and corresponding fits (black, dashed lines) recorded during the agglomeration process of hexadecanethiol-capped gold nanoparticles in tetradecane. a) Measurements on ground at a gold concentration of $c = 1.03$ mg mL-1 (± 0.12 mg mL-1). b) Measurements in microgravity at a gold concentration of $c = 0.86$ mg mL-1 (± 0.16 mg mL-1). c) Measurements on ground at a gold concentration of $c = 2.75$ mg mL^{-1} (± 0.04 mg mL^{-1}). d) Measurements in microgravity at a gold concentration of $c = 3.27$ mg mL^{-1} (± 0.79 mg mL^{-1}). Modified from Pyttlik *et al.*, **2022**.[274]

Table 7: Time-dependent mean residence times τ_{Diff} of the gold nanoparticles during the agglomeration process of hexadecanethiol-capped gold nanoparticles in tetradecane on the ground (1 g) and in microgravity (μ g) after a catapult launch and after a drop. The agglomeration process was initiated by rapid cooling of the sample (from 70 °C to 10 °C). Modified from Pyttlik et al., **2022**.[274]

	τ_{Diff} **(ms)**		τ_{Diff} **(ms)**		
	on ground		*catapult launch*		*drop*
c **(mg mL^{-1})**	1.03 (± 0.12)	2.75 (± 0.04)	0.86 (± 0.16)	3.27 (± 0.79)	2.67
t **(s)**					
1	0.30 (± 0.03)	0.51 (± 0.24)	52 (± 29.9)	58 (± 43.3)	416 (± 164.0)
2	0.32 (± 0.03)	0.40 (± 0.01)	111 (± 32.0)	255 (± 80.5)	316 (± 63.4)
3	0.32 (± 0.04)	0.39 (± 0.13)	149 (± 64.2)	385 (± 160.4)	360 (± 137.7)
4	0.32 (± 0.03)	0.42 (± 0.10)	181 (± 50.8)	434 (± 120.1)	332 (± 64.4)
5	0.34 (± 0.03)	0.51 (± 0.11)	168 (± 44.5)	485 (± 109.7)	/
6	0.34 (± 0.01)	0.61 (± 0.14)	163 (± 37.3)	427 (± 77.9)	/
7	0.36 (± 0.01)	0.67 (± 0.11)	139 (± 44.8)	385 (± 90.1)	/
8	0.35 (± 0.01)	0.71 (± 0.07)	98 (± 43.4)	377 (± 42.4)	/

Table 8: Apparent hydrodynamic diameters d_H of the gold nanoparticles during the agglomeration process of hexadecanethiol-capped gold nanoparticles in tetradecane on the ground (1 g) and in microgravity (µ g) after a catapult launch and after a drop. The agglomeration process was initiated by rapid cooling of the sample (from 70 °C to 10 °C). Modified from Pyttlik et al., **2022**.[274]

	d_H (nm)		d_H (nm)		
	on ground		catapult launch		drop
c (mg mL^{-1})	1.03 (± 0.12)	2.75 (± 0.04)	0.86 (± 0.16)	3.27 (± 0.79)	2.67
t (s)					
1	83 (± 30.9)	139 (± 81.3)	52 (± 29.9)	58 (± 43.3)	416 (± 164.0)
2	53 (± 12.0)	66 (± 13.2)	111 (± 32.0)	255 (± 80.5)	316 (± 63.4)
3	46 (± 18.6)	56 (± 28.1)	149 (± 64.2)	385 (± 160.4)	360 (± 137.7)
4	43 (± 9.2)	58 (± 17.9)	181 (± 50.8)	434 (± 120.1)	332 (± 64.4)
5	43 (± 7.8)	65 (± 17.7)	168 (± 44.5)	485 (± 109.7)	/
6	42 (± 7.3)	75 (± 21.1)	163 (± 37.3)	427 (± 77.9)	/
7	46 (± 8.0)	85 (± 19.7)	139 (± 44.8)	385 (± 90.1)	/
8	41 (± 4.7)	83 (± 12.3)	98 (± 43.4)	377 (± 42.4)	/
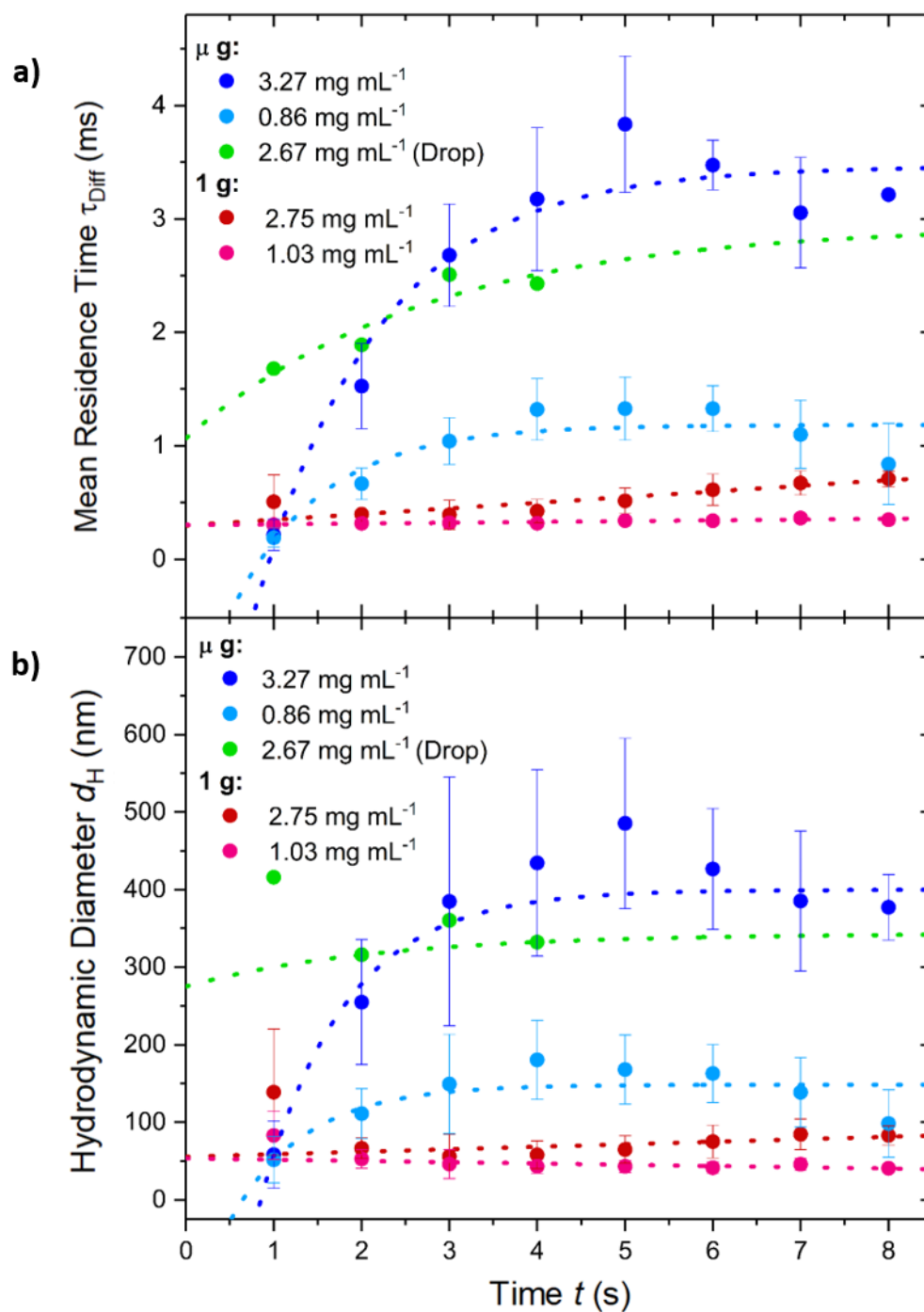
Figure 42: (a) Comparison of averaged mean residence times τ_{Diff} and the corresponding standard deviations of hexadecanethiol-capped gold nanoparticles in tetradecane during the agglomeration process of the particles. (b) Comparison of averaged apparent hydrodynamic diameter d_H and the corresponding error propagation of hexadecanethiol-capped gold nanoparticles in tetradecane during the agglomeration process of the particles. The agglomeration was induced by rapid cooling of the sample (70 °C to 10 °C). Experiments were performed with different concentrations on ground (1 g) and in microgravity (μ g) by catapult launches and by a drop. The dashed lines serve as guidance for the eye to highlight the trend of the growth of the agglomerates. From Pyttlik *et al.,* **2022**.[274]

Besides the more monodisperse size distribution, it was shown that the obtained mean residence times τ_{Diff} and the apparent hydrodynamic diameter d_H of the agglomerates found in microgravity are consistently larger than on ground. Additionally, a more prominent effect of the concentration on τ_{Diff} was found in microgravity. While on ground increasing the gold concentration by a factor of 2.7 doubled τ_{Diff} at $t = 8$ s, in microgravity an increase of the gold concentration by a factor of 3.8 lead to an increase of τ_{Diff} by a factor of 3.8 at $t = 8$ s. It is worth noticing that the error propagations of the hydrodynamic diameters are larger than the standard deviations of the mean residence times due to the uncertainties of the temperature calculations used for the calculations of the hydrodynamic diameters. But even considering these large uncertainties, the difference between the hydrodynamic diameters obtained on ground and in microgravity is sufficiently large to clearly indicate valid increased agglomerate sizes in μg. The main differences that changed during the agglomeration process when comparing terrestrial conditions to microgravity were the absence of sedimentation and convection (compare also **Chapter 2.4.1**). For conventional crystallization and colloids in general it has been reported that elimination of bouncy driven forces can cause more homogeneous as well as larger aggregates.[226,228,77,229]

To verify if agglomerates indeed grew larger in microgravity than on ground, the sedimentation of larger particles on ground needed to be excluded. For that purpose, the sedimentation and the diffusion of the particles are theoretically compared in **Chapter 7.1**. Even if agglomerates with a hydrodynamic diameter of $d_H = 800$ nm would have formed, the diffusion of the particles would still be much faster than sedimentation of the particles. Consequently, even agglomerates much larger than the agglomerates formed on ground would have been detectable with DLS measurements and would not have been able to leave the measurement volume.

A more likely explanation of the difference between the observations made on ground and in microgravity is the transition from a reaction-limited aggregation (RLA) of the particles on ground, to a diffusion-limited aggregation (DLA) in microgravity. For other particle systems, a purely diffusive behavior has already been reported in microgravity. Potenza *et al.* concluded in their microgravity study of fluorinated latex particles,[205] that terrestrial conditions are largely affected by sedimentation, leading to rection controlled behavior. The authors demonstrate that in microgravity all measurements reflect diffusion controlled behavior.[205]

Also Mazzoni and Potenza *et al.* found in their study of Teflon colloidal particles that microgravity conditions are required to obtain diffusion limited growth.[78]

During diffusion-limited aggregation, the mass transport of the nanoparticles to the growing agglomerates is the rate determining step of the agglomeration,[279] indicating the aggregation rate is equal to the diffusion rate of the particles and thus independent from the chemical or physical properties of the colloidal system.[279] This results in the identical fractal dimensions of $D_f \approx 1.7 - 1.8$.[280] During the ideal diffusion-limited aggregation (DLA), particles stick after the first collision, resulting in a sticking probability $P = 1$.[205] So particles stick at random positions, leading to the formation of more open agglomerates, where only a few particles have multiple neighbors.[281] The sticking probability of 100% means that the particles are bound strongly indicating the agglomerates do not rearrange or age with time. Agglomerates formed by DLA do not only tend to be larger, but also tend to form more rapidly (assuming similar reaction conditions, for example identical initial particle concentrations and temperatures).[282,283]

In contrast, during a reaction limited aggregation, the growth of the agglomerates is the rate determining step.[279] During reaction-limited aggregation (RLA), particles colloid several times, before they stick together. Each particle is more likely to have multiple neighbors and denser agglomerates are formed. Additionally, the growth rate of the agglomerates depend on the mobility of the particles and their density.[284] The individual particles of the agglomerates formed by RLA still have their mobility, thus the particles might move and the agglomerates might restructure and age. The formed agglomerates become even denser to maximize the number of neighbors of each individual particle and minimize the surface energy of the agglomerates,[284,281] leading to a much higher fractal dimension $D_f < 3$,[280] resulting in a lower radius of gyration.

On ground, it is unlikely to observe a diffusion-limited agglomeration since sedimentation and convection influence the mass transport during the agglomeration process and are hard to prevent. Since convection and sedimentation are reduced in microgravity, a transition from a reaction-limited agglomeration to a diffusion-limited agglomeration is plausible, possibly explaining the formation of larger, more monodisperse agglomerates in microgravity.[205] A schematic illustration of the effect of gravity on the final size and structure of the agglomerates is shown in **Figure 43**.[274]
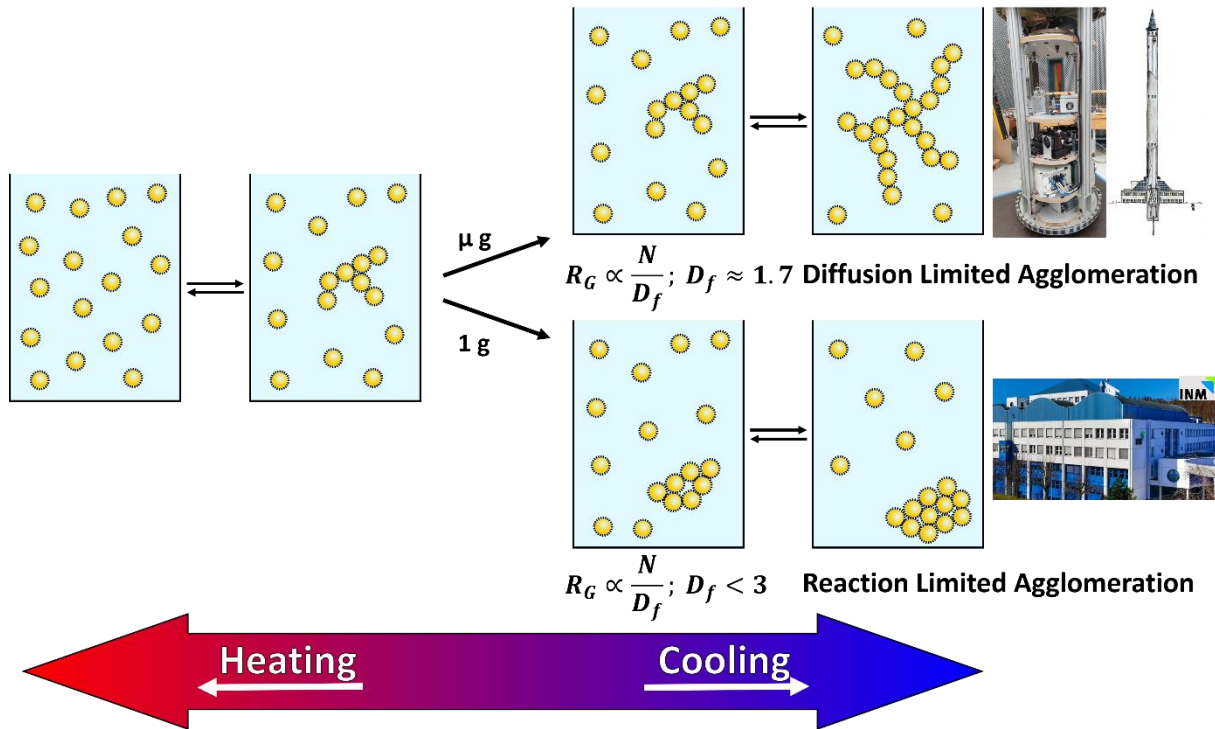
Figure 43: Schematic illustration of the difference between a diffusion- and reaction-limited agglomeration of nanoparticles on ground and in microgravity. Pyttlik *et al.*, **2022**.[274]

The influence of gravity on the convection can be quantified by comparing the Rayleigh number (*Ra*) of the system on ground and in microgravity, see **Chapter 7.2**. The Rayleigh number is a dimensionless number to describe the convection in a fluid.[285] On ground, a Rayleigh number of approximately $Ra \approx 10^5$ and in microgravity of $Ra \approx 10^{-1}$ was found. The strong reduction of the Rayleigh number by a factor of $\approx 10^{-6}$ indicates the strong reduction of the convection in microgravity, even with the large temperature drop during the agglomeration experiments.

For quantifying the influence of gravity on the sedimentation, the Archimedes number (*Ar*) can be taken into account. A comparison of *Ar* of the system on ground and in microgravity is discussed in **Chapter 7.2**. The Archimedes number is a dimensionless number to describe the motion of different fluids due to their different densities. It can be used to characterize the sedimentation of the particles through the medium.[286] On ground, an Archimedes number of approximately $Ar \approx 10^{-8}$ and in microgravity of $Ar \approx 10^{-14}$ was found. In microgravity the Archimedes number strongly decreased (by a factor of $\approx 10^{-6}$), demonstrating the strongly decreased sedimentation of the particles.[287] However, considering the small Archimedes number on ground, sedimentation of the particles or the agglomerates only plays a minor role

(see also **Chapter 7.1**). On ground, convection clearly is the dominant mass transport mechanism, whereas in microgravity, mass transport only occurs through diffusion.

A more diffusion-limited agglomeration in microgravity might explain the observed differences between the agglomeration on ground and in microgravity, and the more rapid formation of larger agglomerates.[74] Assuming the same number of primary particles, a reaction-limited agglomeration results in the formation of a more compact and dense structure of the agglomerates represented by a smaller hydrodynamic diameter. In contrast, a more diffusion-limited process leads to the formation of a more open and less dense structure. This is in alignment with the observation of Yamanka and Mata *et al.* who reported the more dominant growth of dendric structures in microgravity.[260]

Additionally, a diffusion-limited agglomeration leads to the formation of agglomerates with identical fractal dimension, independent from the colloidal system.[279] This results in the formation of self-similar agglomerates,[288] leading to a smaller polydispersity of the agglomerates.[279] This phenomenon explains the smaller size distribution found in microgravity compared to measurement performed on ground. Autocorrelation functions recorded on ground during the agglomeration showed a more stretched mono-exponential decay, indicating the formation of agglomerates with higher polydispersity, see **Figure 40**.

A more diffusion-limited reaction in microgravity can also explain the stronger influence of the initial particle concentration on the observed agglomerate size in microgravity than on ground. If diffusion is the only mass transport during the agglomeration process, collision of the particles only occurs by chance. By increasing the number of particles, the collision probability increases and thus the total collision numbers of the particles. Considering the sticking probability of $P = 1$ for a diffusion-limited agglomeration, every collision results in the growth of the agglomerates, showing a direct relation between the particle concentration and the size of the formed agglomerates. In contrast, during a reaction-limited agglomeration, convection is the defining mass transport which is not influenced by the particle concentration, see **Equation (54)**.

3.4   Dynamic light scattering experiments in hypergravity

The agglomeration experiments performed in microgravity showed a significant influence of gravitation on temperature-induced agglomeration of hexadecanethiol-capped gold nanoparticles in tetradecane. To substantiate the results found in microgravity, the study of the opposing approach appeared a worthwhile challenge. An attempt to investigate the agglomeration process of the system explored in microgravity under increased gravitational forces was carried out. The University of Bremen offered the possibility to perform experiments in hypergravity by utilizing a large-scale centrifuge, see **Figure 44**. With a diameter of 12.5 m, the centrifuge is able to accelerate experimental set-ups up to 30 g.[289]

Figure 44: Photograph of the large-scale centrifuge of the University of Bremen.

To follow the agglomeration process in the centrifuge, the set-up had to withstand the massive acceleration forces of the device. As our set-up proved to be very robust and collect reliable data under physically demanding conditions during the catapult launch, it appeared suitable to be tested for collecting hypergravity data. To integrate the instrumental set-up into the large-scale centrifuge, it was first integrated into the drop-tower capsule. The outer shell of the capsule had to be removed, to be able to integrate the capsule into the centrifuge,

leaving the DLS device and the liquid handling system exposed to the environment, see **Figure 45**.

Figure 45: Photograph of the instrumental set-up implemented in the large-scale centrifuge.

If particle movements are solely due to Brownian motion, the autocorrelation function can be described by using the decay time τ, the mean residence time τ_{Diff} and the constant C, see **Equation (30)**.[197]

$$g_2 - 1 = A \cdot \exp\left(-\frac{2\tau}{\tau_{Diff}}\right) + C \tag{30}$$

During centrifugation, an additional directed movement of the particles along the gravitational force is introduced, which influences the particle movement and depends on the acceleration. To describe the autocorrelation functions recorded during the centrifugation, **Equation (30)** requires to evolve to **Equation (38)**. With an additional constant B, the

scattering vector $\vec{q}$, the diffusion coefficient D_{Diff}, the sedimentation velocity v, and the laser beam width w.[290,291]

$$g_2 - 1 = A \cdot (B \cdot \exp\left(-\vec{q}^2 \cdot D_{Diff} \cdot \tau\right) \cdot \exp\left(-\frac{v^2\tau^2}{w^2}\right)$$
$$+ (1 - B) \cdot \exp\left(-\frac{v^2\tau^2}{w^2}\right))$$

(38)

The modulus of the scattering vector $\vec{q}$ is given by **Equation (25)** and depends on the wavelength of the incident laser beam λ, the scattering angle θ, and the refractive index n.[63,169]

$$|\vec{q}| = \frac{4 \cdot \pi \cdot n}{\lambda} sin\frac{\theta}{2}$$

(25)

The diffusion coefficient D_{Diff} can be described using **Equation (23)**, by using the Boltzmann Constant k_B, the temperature T, the solvent viscosity η and the hydrodynamic diameter of the particles d_H.

$$D_{Diff} = \frac{k_B \cdot T}{3 \cdot \pi \cdot \eta \cdot d_H}$$

(23)

The sedimentation velocity v can be described using **Equation (39)**, with the Earth's acceleration g, the acceleration of the centrifuge a, the density of the particle ρ_P, and the solvent ρ_S.

$$v = \frac{g \cdot a \cdot d_H^2}{18 \cdot \eta} \cdot (\rho_P - \rho_S)$$

(39)

Initially, the DLS device was tested for stability. The previously described non-agglomerating reference system, gold nanoparticles capped with oleylamine in tetradecane was used. The particles had a core diameter of d_{Core} = 7.8 nm (± 0.4 nm) and a hydrodynamic diameter of d_H = 21 nm (± 1 nm). DLS measurements were performed at room temperature. It is assumed, that the particle size stays constant at different g-levels. Considering the size of the particles, an acceleration between 5 and 25 g should not influence the movement of the particles. Since all parameters of the particle system are known, the autocorrelation functions were calculated by using **Equation (38)** and are shown in **Figure 46**. The used parameters are summarized in **Table 9**. To simplify **Equation (38),** the parameter A and B are set to 1.

According to what was reported in literature for DLS instruments, the laser beam width w was assumed to be 0.16 mm. [291]

Table 9: Parameter of the reference system, oleylamine-capped gold nanoparticles in tetradecane, to calculate the autocorrelation functions of the particles at different g-levels.

w (mm)	λ (nm)	n	Θ (°)	T (K)	g (m s^{-2})	η (mPa s)	d_H (nm)	ρ_P (g cm^{-3})	ρ_{Sol} (g cm^{-3})
0.16	635	1.429	90	298.15	9.81	2.13	21	19.32	0.7628

Autocorrelation functions were calculated for 5 g, 15 g and 25 g. As expected, the acceleration did not influence the shape of the calculated autocorrelation functions. In **Figure 46** the autocorrelation functions at 15 g and 25 g were shifted along the y-axis to show the identical shape of the functions and their identical decay.
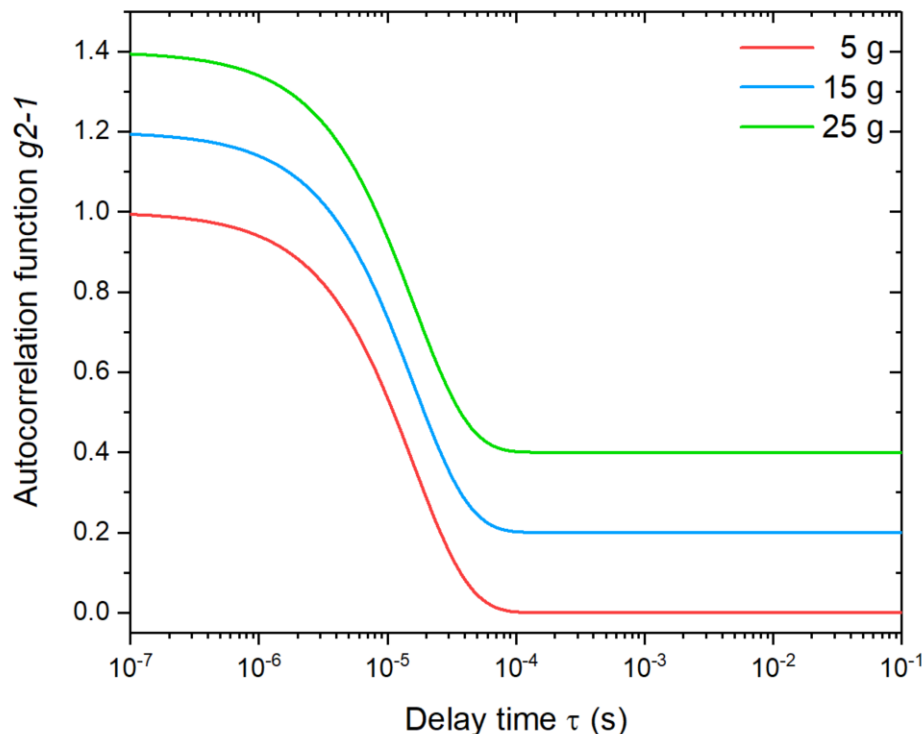
Figure 46: Calculated autocorrelation functions for oleylamine-capped gold nanoparticles in tetradecane at 5 g, 15 g and 25 g. The particles have a hydrodynamic diameter of 21 nm. The functions at 15 g and 25 g were shifted along the y-axis.

To test the DLS device for stability, the reference system was directly placed in the cuvette in the DLS instrument. The large-scale centrifuge was accelerated from 5 g up to 25 g in 2.5 g steps. After reaching the respective g level and a short stabilization period, the acceleration was kept at a constant pace for 2.5 min and a DLS measurement with an integration time of 1 s was recoded. Selected autocorrelation functions are shown in **Figure 47**.
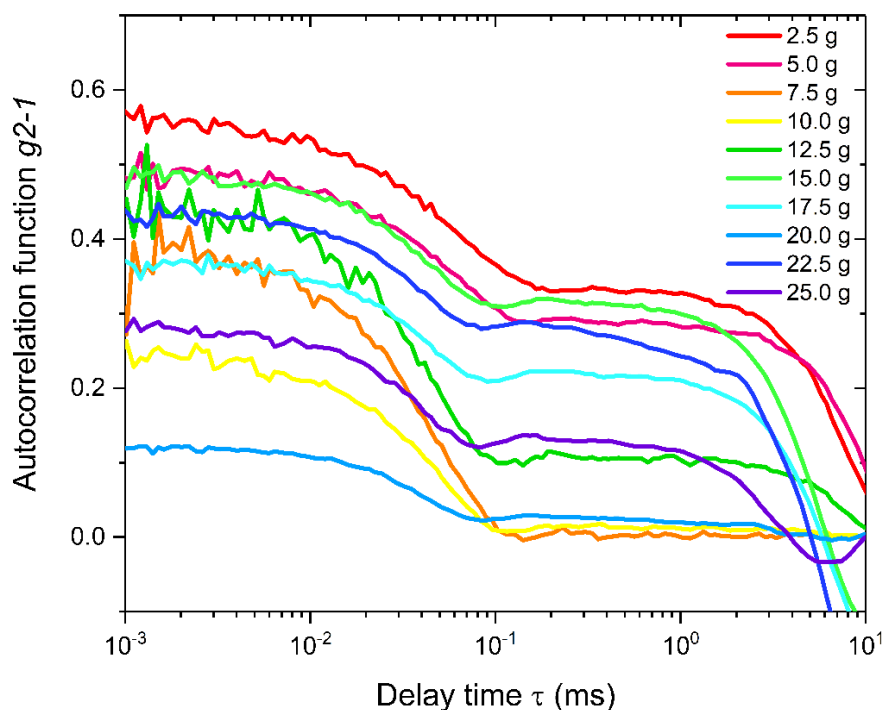
Figure 47: Selected autocorrelation functions of oleylamine-capped gold nanoparticles in tetradecane, with a core diameter of d_{Core} = 7.8 nm (± 0.4 nm) and a hydrodynamic diameter of d_H = 21 nm (± 1 nm). The autocorrelation functions were recorded at different gravitational accelerations, ranging from g =2.5 g up to 25 g.

The recorded autocorrelation functions show an unexpected mismatch at different acceleration levels, see **Figure 47.** These findings indicate that the acceleration of the centrifuge greatly influenced the recorded autocorrelation functions. Additionally, after the deceleration of the centrifuged, optical misalignment of the DLS was clearly noticeable, suggesting the autocorrelation functions may be unreliable.

As discussed above, the instrumental set-up was exposed to the environment during the measurement. This caused two major problems. First, the photo detectors of the DLS instrument are now exposed to the light of the room in which the centrifuge was placed, leading to a high background count and a poor signal-to-noise-ratio. Additionally, the

centrifugation process led to a contrary directed airflow, resulting in an undefined cooling of the whole set-up, especially at higher g-levels. The Peltier element of the measurement cell could not contradict this effect, leading to an undefined temperature of the sample during the DLS measurements.

To be able to perform experiments in hypergravity using the large-scale centrifuge, the instrumental set-up needs to be adapted. At first, the optical path of the DLS set-up has to be secured and fixated to allow DLS measurements during higher acceleration for an extended period of time. Subsequently, an adequate shell needs to be built to shield the instrumental set-up from disruptive environmental influences, as additional light and the airflow caused by the acceleration.

4 Conclusion and Outlook

Nanocomposites can outperform classical materials in certain applications, especially due to their tunability in terms of structure and properties. Rashid *et al.* conclude in their 2021 review that future research should improve tools to predict and optimize properties, and exploit inherent flexibility in design.[292] The properties of nanocomposites depend not only on the nature of the nanofillers, but also on their arrangement and distribution in the polymer matrix.[32,33,34] Agglomeration of the nanoparticles thus affects their properties. Gravity and sedimentation of the agglomerates hinder the study of their effects.

During this project, a first step towards an understanding of the agglomeration of gold nanoparticles in the absence of sedimentation and convection was realized. To the best of our knowledge, we were the first to experimentally study the agglomeration of technically important gold nanoparticles in microgravity and compared it with results on ground. For this purpose, a suitable colloidal system, an option to apply microgravity conditions and an appropriate analytical method to study the process were needed. Reliable dynamic light scattering measurements were performed in microgravity and the results were compared with the analogous agglomeration process under terrestrial conditions. In the following, we summarize the conclusion from the necessary preparatory steps, tests to prove validity of the data collected, and the outcomes of the comparison between the agglomeration processes in microgravity and normal gravity.

4.1 Particle system

One prerequisite to study agglomeration of gold nanoparticles in microgravity was to find a suitable agglomerating system. A reliable and practicable way to rapidly induce agglomeration in a reversible manner was essential to perform valid measurements in microgravity and compare the corresponding data. We decided to investigate hexdecanethiol-capped gold nanoparticles. Their colloidal stability is largely affected by temperature, and a rapid temperature drop appeared appropriate to induce the agglomeration process. Importantly, it had already been demonstrated by our group, that the system shows a completely reversible temperature dependent behaviour. Indeed, the system allowed for an exactly in time triggering of agglomeration in the course of this project. We could exploit the temperature

dependent reversibility of the agglomeration of hexadecanethiol-capped nanoparticles to collect multiple data sets and proof reproducibility.

4.2 Microgravity conditions

The drop tower facility of the ZARM Institute in Bremen was chosen as a microgravity environment. It is located conveniently in Northern Germany and could be reached by car in several hours from INM Saarbrücken. The drop tower offers the opportunity to realize microgravity conditions of 4.7 s, performing a simple drop with a special capsule. A unique opportunity to perform a catapult launch extends the microgravity interval to 9.3 s. Furthermore, the drop tower is equipped with a multi-platform drop capsule for installing the equipment required and the analytical device. The microgravity interval turned out to be sufficient to collect evaluable data, during the catapult launch as well as during a drop experiment.

4.3 Agglomeration and analytical set-up

A technical set-up suitable to rapidly induce agglomeration and subsequently collect analytical data during the microgravity interval was developed, that could be fitted into the drop tower capsule. Dynamic light scattering (DLS) has already been established as applicable in microgravity, and it features some inherent advantages. On one hand, it provides precise particle sizes without disturbing the dispersion, on the other hand, the device can be built in a simple, robust and compact way. Indeed, we were able to collect reliable DLS data with an instrument developed in collaboration with LS Instruments (Fribourg, Switzerland). The instrument was sufficiently robust to withstand the acceleration and deceleration forces during the drops and launches and multiple valid data sets were recorded. While for a simple drop experiments 4 measurements per experiment could be recorded, catapult launches allowed to collect 8 data sets per experiment.

The agglomeration process was induced via a specially designed liquid handling system, developed during this thesis at INM. Using a syringe pump, the sample dispersion was transferred through an aluminium heating block, which was heated to 70 °C (the agglomeration temperature of the sample was determined at T_{Agglo} = 60° C). Afterwards it was injected into the precooled measurement cell (T = 10°C) of the DLS instrument. The system allowed a remotely controlled and rapid start of the agglomeration process, and it was

demonstrated that the analytical measurements were neither disturbed by the sample handling nor by the physical impact of the catapult.

4.4   Reliability of the developed set-up

Test and reference measurements were carried out to ensure validity of the data. The complexity of the experimental set-up and the sample was successively increased. Initially, a basic test was performed with non-agglomerating silica nanoparticles without applying the liquid handling system. Results on ground and in microgravity were identical, proving that the DLS is in principle robust enough for the catapult launch.

Subsequently, oleylamine-capped gold nanoparticles were investigated as non-agglomerating system, mimicking the thiol-capped gold nanoparticles as closely as possible. DLS measurements with the liquid handling system and a temperature drop were performed on ground and in microgravity during a catapult launch. Comparison of the data showed no significant differences, demonstrating that the set-up developed is indeed suitable and robust enough to perform measurements in the drop tower.

4.5   Microgravity agglomeration

The agglomeration of hexadecanethiol-capped gold nanoparticles was studied in microgravity and compared with the analogous measurements performed on ground. In microgravity and on ground two different particle concentrations were studied.

On ground or during catapult launches, the first measurements (at $t = 1$ s) could not be evaluated. On ground convection and in microgravity acceleration forces from the launch compromised the recorded autocorrelation functions. The other measuring points (after $t = 2$ s), however, delivered plausible data. Performing a drop experiment ensured that all recorded autocorrelation functions could by analyzed. The recorded autocorrelation functions were fitted with **Equation (30)** to obtain the average mean residence times τ_{Diff}. The corresponding apparent hydrodynamic diameters d_H were calculated by using **Equation (32)** and the temperatures T, refractive indices n, and dynamic viscosities η which are summarized in **Table 2**. A direct comparison of the measurements performed on ground with the results observed in microgravity revealed several major differences. First, a comparison of the used fit function showed a perfect match for the data recorded in microgravity, whereas on ground

a more stretched mono-exponential fit was found. Those findings indicate the formation of more uniform agglomerates with a narrower size distribution in microgravity.

Secondly, the size of the agglomerates found in microgravity was significantly larger than those determined on ground. Importantly, this effect was more prominent for the higher concentration (3.8 times larger agglomerates) than for the lower (2 times larger agglomerates).

These observations are interpreted as a shift from a more reaction-limited agglomeration (RLA) on ground to a more diffusion-limited agglomeration (DLA) in microgravity. A transition to DLA results in a shift from slowly formed compact agglomerates with a smaller hydrodynamic diameter to the rapid formation of agglomerates with a more open structure and a larger hydrodynamic diameter. Additionally, a diffusion-limited agglomeration process is more sensible to the initial particles concentration than a reaction-limited agglomeration, which explains a stronger dependency of the hydrodynamic diameter of the formed agglomerates on the initial particle concentration in microgravity than on ground.[293]

In summary, it was shown that it is possible to follow the agglomeration process of gold nanoparticles by recording DLS measurements in microgravity after catapult launches in a drop tower. It was demonstrated for the first time that high-density nanoparticles in dispersion are distinctly affected by microgravity. A strong influence of gravity on the agglomeration mechanism was found.

4.6 Hypergravity

To complement microgravity experiments, the particle system was studied in hypergravity. Since an impressive robustness of the system applied in microgravity was proven as major part of this project, the technical set-up developed was integrated into a large-scale centrifuge available at Bremen University. Unfortunately, the outer shell of the capsule had to be removed to fit into the centrifuge exposing the setup to light and airflow. This led to a poor signal-to-noise-ratio during the DLS measurements and an undefined cooling of the cell. Additionally, optical misalignment of the DLS was observed after the experiment, suggesting the autocorrelation functions may be unreliable. The recorded autocorrelation functions showed an unexpected mismatch at different acceleration levels. Further experiments will be required to evaluate the role of hypergravity on the agglomeration process.

4.7 Outlook

This thesis has opened new venues into the study of gravitational effects on particles agglomeration. Further experiments should extend its findings. First, the experiments were only performed recoding DLS data with one single scattering angle. Multi-angle DLS would provide access to information about the shape of the formed agglomerates,[294] and dynamics of the agglomeration process.[295] By analyzing autocorrelation functions of the agglomeration process at multiple scattering angles, the dependency of the obtained mean residence times and the scattering vector reveals information about the reaction dynamics. For example, a linear dependency of the mean residence times and the square of the scattering vector indicates a diffusion limited agglomeration process.[295] To gain additional insight into the structure of agglomerates grown in microgravity, the instrumental set-up can also be extended with a static light scattering set-up.[279]

Secondly, the monitoring time of the agglomeration process was limited to the 9.3 s microgravity interval during the catapult launch. It is difficult to estimate how far the overall agglomeration process has been progressed in the observed interval (early-stage vs complete agglomeration). To obtain deeper insights and confirm the assumptions made, a longer observation period would be essential. Repeating the experiments in sounding rockets would allow for a study with extended microgravity interval. This approach is currently investigated in a follow-up project with an adapted set-up for a sounding rocket.

5 Experimental Details

The following experimental sections have been published in "Dynamic Light Scattering on Nanoparticles in Microgravity in a Drop Tower" by Pyttlik, Kuttich and Kraus in *Microgravity Science and Technology*, in **2022**.[196] and as "Microgravity Removes Reaction Limits from Nonpolar Nanoparticle Agglomeration" by Pyttlik, Kuttich and Kraus in *Small*, in **2022**.[274]

5.1   Sample preparation

5.1.1 Synthesis of chloroauric acid

The synthesis of chloroauric(III) acid by oxidation of gold with aqua regia is a well-established synthetic route in literature.[296] 2.7 g gold were placed in 12 mL aqua regia (a mixture of 9 mL hydrochloric acid (37 % Sigma Aldrich, Darmstadt, Germany) and 3 mL nitric acid (70 %, Sigma Aldrich, Darmstadt, Germany)). The mixture was heated to 100 °C. After 20 min, additional 4 mL aqua regia was added. After the gold was completely dissolved, the aqua regia was evaporated at ambient pressure until a reaction volume of 2 mL remained. Chloroauric acid was crystalized by placing the hot reaction flask on ice. The formation of yellow, needle shaped crystals was observed. To remove any excess acid and water, the crystals were dried for 48 h at 35 mbar. Afterwards, the crystals were completely dried under high vacuum and stored under an argon atmosphere.

5.1.2 Synthesis of gold nanoparticles

Oleylamine-capped gold nanoparticles with a core diameter of d_{Core} = 7.8 nm (± 0.4 nm) and a hydrodynamic diameter of d_H = 21 nm (± 1 nm) were synthesized following the established synthetic route of Zheng *et al.*[269] 1 g borane-tertbutylamine (97 %, Aldrich, Darmstadt, Germany) was dissolved in a 50 mL of a mixture of benzene (≥ 99 %, Sigma Aldrich, Darmstadt, Germany) and oleylamine (c18 content 80-90 %, Acros Organics Geel, Belgium) (with a mixing ratio of 1:1). As reaction mixture, 2.5 g chloroauric acid were dissolved in a mixture of 450 mL benzene (≥ 99 %, Sigma Aldrich, Darmstadt, Germany) and oleylamine (c18 content 80-90 %, Acros Organics Geel, Belgium) (with a mixing ratio of 1:1). The reaction mixture was flushed

with argon and stirred for 2.5 min at room temperature. Subsequently, the dissolved borane-tertbutylamine was added. The reaction mixture immediately turned from gold to a dark red color. The reaction was stirred for additional three hours. The particles were purified by precipitation with a mixture of ethanol und methanol (with a mixing ratio of 2:1) followed by centrifugation. The supernatant was discarded, and the particles were redispersed in 250 mL toluene (99 %, abcr, Karlsruhe, Germany).

5.1.3 Sample preparation of non-agglomerating gold nanoparticles

To perform experiments with non-agglomerating gold reference samples, the oleylamine ligand shell was renewed. To renew the ligand shell, oleylamine-capped nanoparticles in toluene were heated under reflux and 100 mL oleylamine (c18 content 80-90 %, Acros Organics Geel, Belgium) were added to the suspension. The sample was stirred under reflux for 150 min. The excessive oleylamine was removed by precipitation of the gold nanoparticles with a mixture of ethanol and methanol (2:1) followed by centrifugation. The supernatant was discarded and the particles were redispersed in 100 mL toluene (99 %, abcr, Karlsruhe, Germany). This washing step was repeated 3 times. After the last washing step, the particles were redispersed in tetradecane (99 % abcr, Karlsruhe, Germany). The core diameter of the particles was determined by SAXS measurements. The measurements were performed at T = 20 °C and the scattering data were analyzed using a Schulz-Zimm model, see **Figure 48**. A core diameter of d_{Core} = 7.8 nm (± 0.4 nm) was obtained. To ensure the spherical shape of the synthesized gold nanoparticles, transmission electron microscopy (TEM) images were recorded, see **Figure 49**. The surface plasmon peak of the gold nanoparticles was determined to minimize the absorption by the laser used for the DLS experiments. The recorded UV/Vis spectrum of the particles showed an absorption maximum at λ = 526 nm, see **Figure 50**.
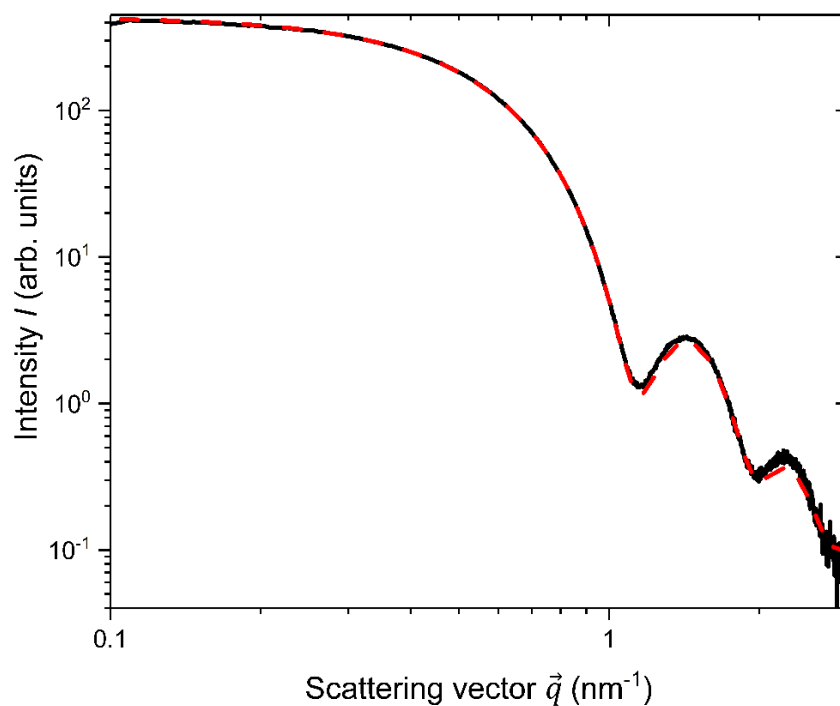
Figure 48: Recorded SAXS data (black line) and corresponding fit (red dashed line) of oleylamine-capped gold nanoparticles. A core diameter of d_{Core} = 7.8 nm (± 0.4 nm) was obtained. From Pyttlik *et al.*, **2022**.[196]
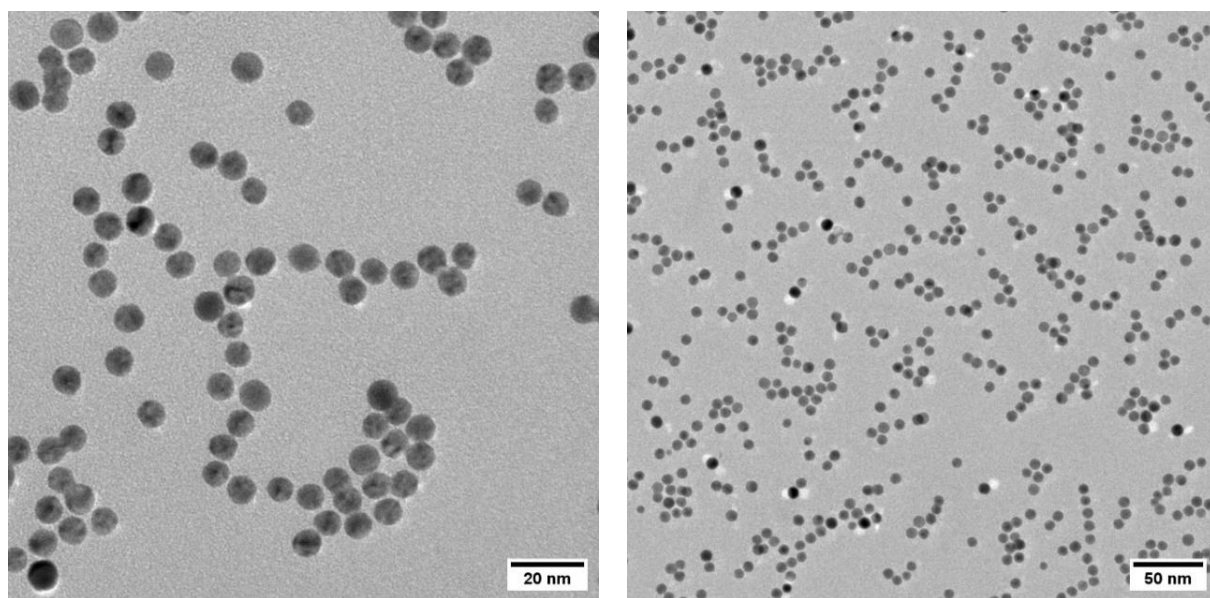
Figure 49: TEM images of oleylamine-capped gold nanoparticles with a core diameter of d_{Core} = 7.8 nm (± 0.4 nm). From Pyttlik *et al.*, **2022**.[196]
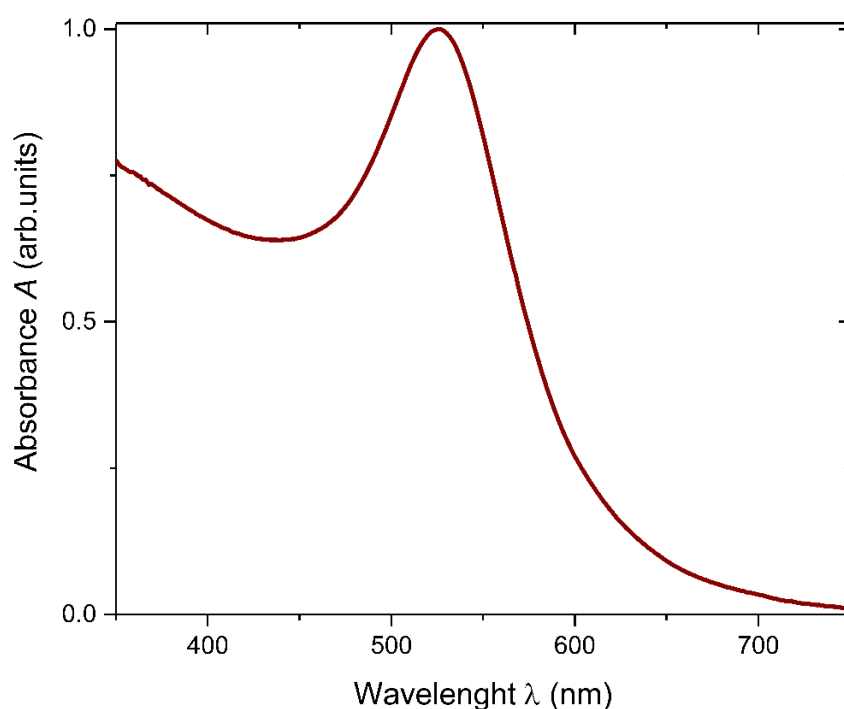
Figure 50: UV/Vis spectrum of oleylamine-capped gold nanoparticles with an absorption maximum of λ_{max} = 526 nm. From Pyttlik *et al.*, **2022**.[196]

5.1.4 Sample preparation of agglomerating gold nanoparticles

To perform experiments with gold nanoparticles, which will agglomerate during the DLS experiments due to the temperature change, hexadecanethiol-capped gold nanoparticles were synthesized. Oleylamine-capped gold nanoparticles were synthesized (see **Chapter 5.1.2**) followed by a ligand exchange to remove the oleylamine of the gold surface and replace it with hexadecanethiol. A modified protocol of Pileni was followed.[297] 10 mL of the gold nanoparticle dispersion in toluene was heated to approximately 100 °C and 1 mL 1- hexadecanethiol (≥ 95%, Sigma-Aldrich, Darmstadt, Germany) was added to the dispersion. After the reaction mixture was stirred for 20 min, the particles were purified by precipitation, followed by centrifugation. A mixture of ethanol and methanol (with a ratio 2:1) was added until the reaction mixture turned dark blue. After centrifugation, the supernatant was discarded and the agglomerated particles were redispersed in 10 mL toluene (99%, abcr, Karlsruhe, Germany). The purification was repeated two times. After the final centrifugation step, the particles were redispersed in 10 mL tetradecane (99 %, abcr, Karlsruhe, Germany). The recorded TEM images clearly showed the agglomerated nanoparticles, however, it still showed that the single nanoparticles preserved their spherical shape, see **Figure 51**. The

recorded UV/Vis spectrum of the particles showed an absorption maximum at λ = 518 nm, see **Figure 52**. Only a very small change of λ = 8 nm of the absorption maximum was observed after the ligand exchange. To be able to observe the deagglomerated gold nanoparticles, the UV/Vis measurement was performed at T = 75 °C.
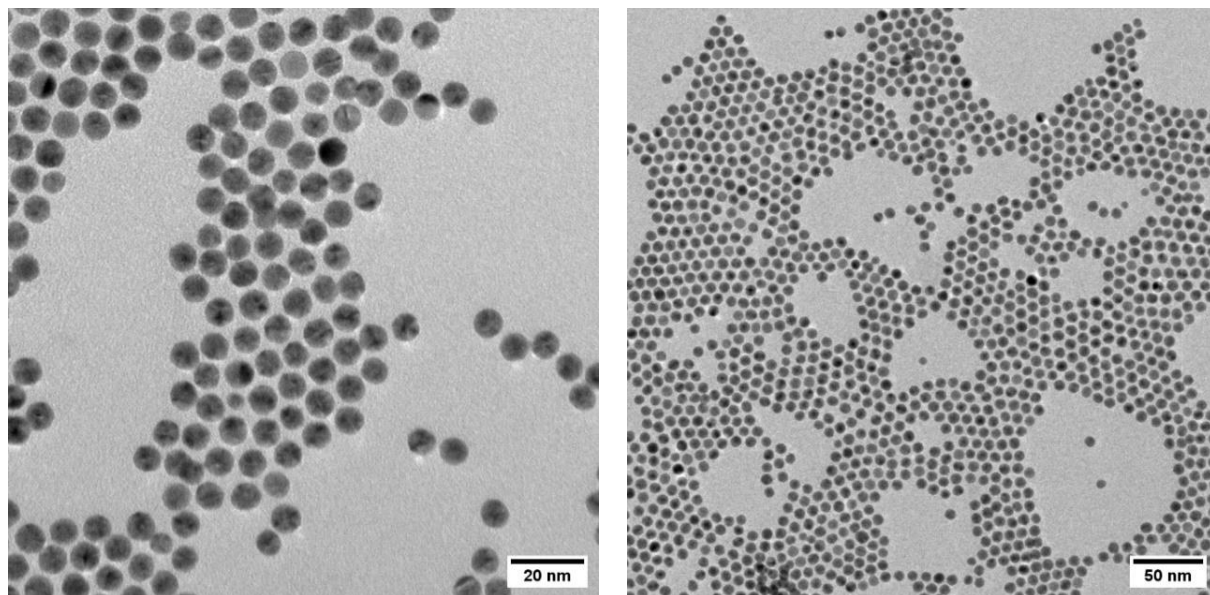
Figure 51: TEM images of hexadecanethiol-capped gold nanoparticles with a core diameter of d_{Core} = 7.8 nm (± 0.4 nm).
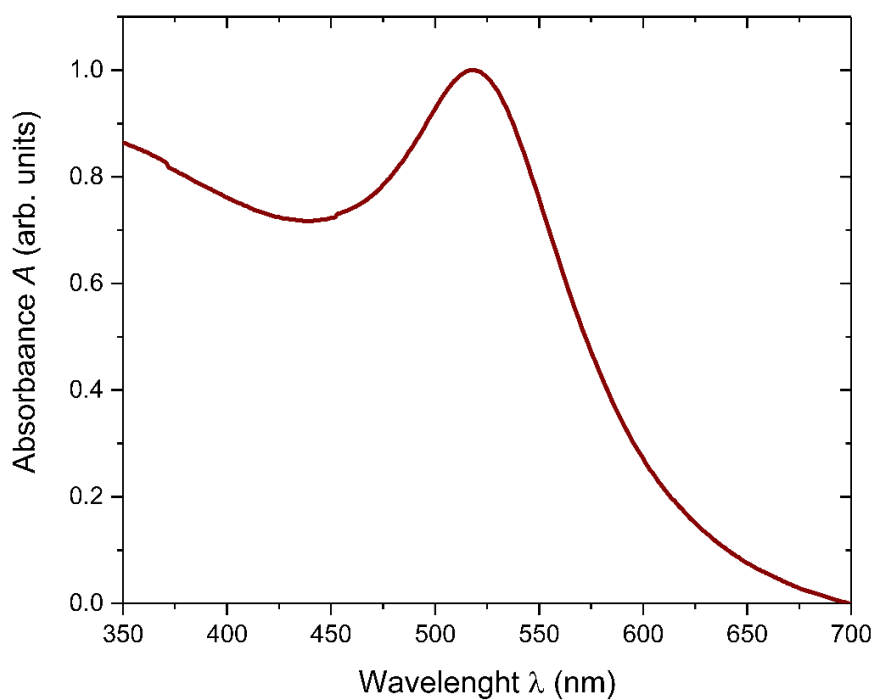
Figure 52: UV/Vis spectrum of hexadecanethiol-capped gold nanoparticles with an absorption maximum of λ = 518 nm, at T = 75 °C.

5.1.5 Particle characterization

To determine the core diameter of the gold nanoparticles, small angle X-ray measurements were performed by using a Xeuss 2.0 from Xenoncs (Grenoble, France). A copper Kα anode with a wavelength of $\lambda = 0.154$ nm was used. The instrument was equipped with a PILATUS Hybrid Photon Counting Detector from Dectris (Baden-Daettwil, Switzerland). 2D diffraction patterns were recorded with a sample to detector distance of 1200 mm. With the software FOXTROT v3.4.9, the fully isotropic 2D patterns were radially averaged into 1D scattering patterns. The final data analysis was performed using the software sasfit 0.94.11 (Villingen PSI, Switzerland) by applying a Schulz-Zimm fit model.

The gold concentration of the gold nanoparticle sample was determined by inductive coupled plasma optical emission spectroscopy (ICP-EOS) measurements. The experiments were performed using a Horiba Jobin Yvon Ultima 2 spectrometer (Oberursel, Germany) with an emission wavelength of $\lambda = 242.795$ nm.

5.2 Dynamic light scattering measurements

To perform dynamic light scattering measurements at a constant temperature and with a temperature drop under normal and microgravity conditions, the commercial DLS instrument NanoLab 3D was modified in cooperation with LS Instruments (Fribourg, Switzerland). A laser with a wavelength of $\lambda = 638$ nm and a scattering angle of $2\theta = 90°$ was used. The measurement cell was a quartz glass cuvette with an outer square-cross section of 12.5 mm and a height of 46 mm was used. The inner square-cross section was 10 mm and the thickness of the bottom was 1.25 mm. The measurements were performed at normal gravity conditions (1 g) or under microgravity conditions (μ g). The 2D pseudo-cross mode was used to record the autocorrelation functions, thereby a single laser beam illuminated the scattering volume. The scattering intensity was detected using two separate detectors. The mean residence time τ_{Diff} was obtained by fitting the autocorrelation functions with a simple exponential decay, by using the software Origin 2017 64bit from OriginLab (Northampton, United States). The corresponding hydrodynamic diameters d_H were calculated using the Stokes-Einstein relation (see **Chapter 2.3**). DLS measurements were performed at a constant temperature of $T = 20\,°C$ or with a temperature drop. The temperature drop was realized by heating the sample

externally inside a heating block. The heating block consisted of an aluminum block, where the liquid sample could be passed through by using plastic tubes. The aluminum block was heated using a silicon heating mat SR Pro 12 V 60 W (Frankfurt am Main, Germany) and a customized control system built by the mechanical workshop of the Leibniz Institute for New Materials (Saarbrücken, Germany). 3 mL of the sample were heated externally to 70 °C and injected into the pre-cooled measurement cell (10 °C) with an injection speed of 1 mL s^{-1} using a Cetoni syringe pump (Korbussen, Germany). 1 mL of the sample stayed inside the tubing as dead volume needed to connect the heating block and the measurement cell, so a total sample volume of 2 mL was injected into the measurement cell, with a deviation of approximately 50 µL. To prevent any disturbing scattering signals from dust or other contaminants, the particles were filtered [63] by using a syringe filter with pore sizes of 20 nm (Whateman). To determine the temperature inside the measurement cell during the temperature drop, the temperature was measured with a type K thermocouple and recorded using a GFT 300 UV datalogger from Greisinger (Regenstauf, Germany). Additionally, the temperature was determined by using non-agglomerating reference particles. It was assumed that the hydrodynamic diameter of these particles stayed constant during the temperature drop. By recording the autocorrelation functions, the corresponding temperatures inside the measurements cell could be calculated numerically using the software Mathematica 11.2 from Wolfram Research (Campaign, United States).

5.3 Dynamic light scattering experiments in microgravity

Experiments in microgravity were performed at the ZARM Institute in Bremen (Germany) in the drop tower. The drop provides a microgravity of 10^{-6} g for 9.3 s during a catapult launch and 4.7 s during a drop experiment. The experimental set-up was integrated into the drop tower capsule and sealed inside a steel shell, see **Figure 9**. To minimize condensation on the measurement cell during the cooling, the capsule was filled with argon. The drop tower capsule was placed either into the catapult system (see **Figure 10**) or lifted to the top of the tower for the drop experiments.

After the drop tower capsule was placed, the drop tower is sealed and evacuated for approximately 2 h. During the experiments with a temperature drop the injection of the

sample was finished right before the lift-off of the capsule. Autocorrelation functions were recorded as soon as the experimental set-up entered microgravity.

5.4   Dynamic light scattering experiments in hypergravity

Experiments in hypergravity were performed at Bremen University, using their large-scale centrifuge, see **Figure 44**. The centrifuge had a diameter of 12.5 m and provided continuously accelerations between 1 g up to 30 g. Experiments were performed by simply integrating the instrumental set-up into the drop tower capsule, followed by implementing the open drop tower capsule (without the outer shell) into the centrifuge, see **Figure 45**. Experiments were performed, using the previously described non-agglomerating gold nanoparticle reference sample, oleylamine-capped gold nanoparticles in tetradecane with a core diameter of d_{Core} = 7.8 nm (± 0.4 nm) and a hydrodynamic diameter of d_H = 21 nm (± 1 nm). Experiments were performed at an acceleration of 2.5 g, 5 g,7.5 g, 10 g, 12.5 g, 15 g, 17.5 g, 20 g, 22.5 g and 25 g. The centrifuge was accelerated to the desired acceleration, after 161 s a steady acceleration could be ensured and the DLS measurements were started. 163 autocorrelation functions with an integration time of 1 s were recorded. Subsequently, the acceleration was increased up to the next desired level.

6 Bibliography

1.   Woithe, J., Wiener, G. J. & Van Der Veken, F. F. Let's have a coffee with the Standard Model of particle physics! *Phys. Educ.* **52**, (2017).

2.   Talmage, D, W. & Sanderson, R, J. Why is Gravity so weak. *Phys. Essays* **7**, 415–421 (1994).

3.   Galili, I., Bar, V. & Brosh, Y. Teaching Weight-Gravity and Gravitation in Middle School: Testing a New Instructional Approach. *Sci. Educ.* **25**, 977–1010 (2016).

4.   Springel, V., Frenk, C. S. & White, S. D. M. The large-scale structure of the Universe. *Nature* **440**, 1137–1144 (2006).

5.   Knight, T. A. On the direction of the radicle and germen during the vegetation of seeds. *Philos. Trans. R. Soc. London* **96**, 99–108 (1806).

6.   Chen, R. *et al.* Gravitropism in Higher Plants. *Plant Physiol.* **120**, 343–350 (1999).

7.   Crossley, D., Hinderer, J. & Riccardi, U. The measurement of surface gravity. *Reports Prog. Phys.* **76**, 1–47 (2013).

8.   Velarde, M. G. & Normand, C. Convection. *Sci. Am.* **243**, 92–109 (1980).

9.   Straughan, B. Convection in a variable gravity field. *J. Math. Anal. Appl.* **140**, 467–475 (1989).

10.   Davis, R. H. Sedimentation of Noncolliodal Particles at low Reynolds Numbers. *Ann. Rev. Fluid Mech.* **17**, 91–118 (1985).

11.   Yang, Y. J., Kelkar, A. V., Corti, D. S. & Franses, E. I. Effect of Interparticle Interactions on Agglomeration and Sedimentation Rates of Colloidal Silica Microspheres. *Langmuir* **32**, 5111–5123 (2016).

12.   Cheng, Z., Chaikin, P. M., Zhu, J., Russel, W. B. & Meyer, W. V. Crystallization Kinetics of Hard Spheres in Microgravity in the Coexistence Regime: Interactions between Growing Crystallites. *Phys. Rev. Lett.* **88**, 4 (2002).

13.   Unsworth, B. R. & Lelkes, P. I. Growing tissues in microgravity. *Nat. Med.* **4**, 901–907 (1998).

14.   Amselem, S. Remote Controlled Autonomous Microgravity Lab Platforms for Drug

Research in Space. *Pharm. Res.* **36**, 1–15 (2019).

15. Ahari, H. *et al.* Effect of microgravity on the crystallization of a self- assembling layered material. *Lett. to Nat.* **388**, 857–860 (1997).

16. Lundager Madsen, H. E. *et al.* Calcium phosphate crystallization under terrestrial and microgravity conditions. *J. Cryst. Growth* **152**, 191–202 (1995).

17. McPherson, A. Recent advances in the microgravity crystallization of biological macromolecules. *Trends Biotechnol.* **15**, 197–200 (1997).

18. Lorber, B. The crystallization of biological macromolecules under microgravity: A way to more accurate three-dimensional structures? *Biochim. Biophys. Acta - Proteins Proteomics* **1599**, 1–8 (2002).

19. McPherson, A. & Delucas, L. J. Microgravity protein crystallization. *npj Microgravity* **1**, 1–20 (2015).

20. DeLucas, L. J. *et al.* Protein crystal growth in microgravity. *Science (80-.).* **246**, 651–654 (1989).

21. Erdmann, V. A. *et al.* Crystallization of proteins under microgravity. *FEBS Lett.* **259**, 194–198 (1989).

22. McPherson, A. *et al.* The effects of microgravity on protein crystallization: Evidence for concentration gradients around growing crystals. *J. Cryst. Growth* **196**, 572–586 (1999).

23. Lorber, B. Virus and protein crystallization under hypergravity. *Cryst. Growth Des.* **8**, 2964–2969 (2008).

24. Cross, M., Douglas, W. H. & Fields, R. P. The Relationship Between Filler Loading and Particle Size Distribution in Composite Resin Technology. *J. Dent. Res.* **62**, 850–852 (1983).

25. Yoon, M. K., Chen, H., Simacek, P., Heider, D. & Gillespie, J. W. Modeling VARTM processes with hybrid media incorporating gravity effects. *J. Compos. Mater.* **43**, 2903–2920 (2009).

26. Hanemann, T. & Szabó, D. V. Polymer-Nanoparticle Composites: From Synthesis to Modern Applications. *Materials (Basel).* **3**, 3468–3517 (2010).

27. Tjong, S. C. Structural and mechanical properties of polymer nanocomposites. *Mater.*

Sci. Eng. R **53**, 73–197 (2006).

28. Nelson, J. K. & Hu, Y. Nanocomposite dielectrics — properties and implications. *J. Phys. D. Appl. Phys.* **38**, 213–222 (2005).

29. Parola, S., Julián-lópez, B., Carlos, L. D. & Sanchez, C. Optical Properties of Hybrid Organic-Inorganic Materials and their Applications. *Adv. Funct. Mater.* **26**, 6506–6544 (2016).

30. Mota, E. G., Hörlle, L., Oshima, H. M. & Hirakata, L. M. Evaluation of inorganic particles of composite resins with nano filler content. *Stomatol. Balt. Dent. Maxillofac. J.* **14**, 103–107 (2012).

31. Khan, W. S., Hamadneh, N. N. & Khan, W. A. Polymer nanocomposites - synthesis techniques, classification and properties. in *Science and applications of Tailored Nanostructures* 50–67 (2016).

32. Nan, C., Shen, Y. & Ma, J. Physical Properties of Composites Near Percolation. *Annu. Rev. Mater. Res.* **40**, 131–151 (2010).

33. Kuang, T. *et al.* Creating poly(lactic acid)/carbon nanotubes/carbon black nanocomposites with high electrical conductivity and good mechanical properties by constructing a segregated double network with a low content of hybrid nanofiller. *Adv. Compos. Hybrid Mater.* **6**, 1–12 (2023).

34. Ngo, I. L., Prabhakar Vattikuti, S. V. & Byon, C. A modified Hashin-Shtrikman model for predicting the thermal conductivity of polymer composites reinforced with randomly distributed hybrid fillers. *Int. J. Heat Mass Transf.* **114**, 727–734 (2017).

35. Ribeiro, T., Baleizão, C. & Farinha, J. P. S. Functional films from silica/polymer nanoparticles. *Materials (Basel).* **7**, 3881–3900 (2014).

36. Liu, H. & Webster, T. J. Mechanical properties of dispersed ceramic nanoparticles in polymer composites for orthopedic applications. *Int. J. Nanomedicine* **5**, 299–313 (2010).

37. Nam, S. *et al.* Effects of silica particles on the electrical percolation threshold and thermomechanical properties of epoxy / silver nanocomposites. *Appl. Phys. Lett.* **99**, 1–3 (2011).

38. Huang, J.-C. Carbon Black Filled Conducting Polymers and Polymer Blends. *Adv. Polym. Technol.* **21**, 299–313 (2002).

39. Hassenkam, T. *et al.* Self-Assembly and Conductive Properties of Molecularly Linked Gold Nanowires. *Nano Lett.* **4**, 19–22 (2004).

40. Lu, Y., Yang, M., Qu, F., Shen, G. & Yu, R. Enzyme-functionalized gold nanowires for the fabrication of biosensors. *Bioelectrochemistry* **71**, 211–216 (2007).

41. Lu, C. *et al.* Flexible and stretchable nanowire-coated fibers for optoelectronic probing of spinal cord circuits. *Sci. Adv.* **3**, (2017).

42. Choi, S. *et al.* Highly conductive, stretchable and biocompatible Ag–Au core–sheath nanowire composite for wearable and implantable bioelectronics. *Nat. Nanotechnol.* **13**, 1048–1056 (2018).

43. Gong, S. *et al.* Highly Stretchy Black Gold E-Skin Nanopatches as Highly Sensitive Wearable Biomedical Sensors. *Adv. Electron. Mater.* **1**, 1–7 (2015).

44. Ryan, K. M., Mastroianni, A., Stancil, K. A., Liu, H. & Alivisatos, A. P. Electric-Field-Assisted Assembly of Perpendicularly Oriented Nanorod Superlattices. *Nano Lett.* **6**, 1479–1482 (2006).

45. Triet, M. *et al.* Electrical property enhancement by controlled percolation structure of carbon black in polymer-based nanocomposites via nanosecond pulsed electric field. *Compos. Sci. Technol.* **154**, 165–174 (2018).

46. Bayrak, T., Helmi, S., Ye, J. & Kauert, D. DNA-Mold Templated Assembly of Conductive Gold Nanowires. *Nano Lett.* **18**, 2116–2123 (2018).

47. Raeesi, V., Chou, L. Y. T. & Chan, W. C. W. Tuning the Drug Loading and Release of DNA-Assembled Gold-Nanorod Superstructures. *Adv. Mater.* **28**, 8511–8518 (2016).

48. Leeuwenburgh, S. C. G., Ana, I. D. & Jansen, J. A. Sodium citrate as an effective dispersant for the synthesis of inorganic-organic composites with a nanodispersed mineral phase. *Acta Biomater.* **6**, 836–844 (2010).

49. Zhao, R., Zhao, J., Wang, L. & Dang, Z. M. Reduced sedimentation of barium titanate nanoparticles in poly(vinylidene fluoride) films during solution casting by surface modification. *J. Appl. Polym. Sci.* **132**, 6–11 (2015).

50. Eckert, T., Schmidt, M. & De Las Heras, D. Sedimentation path theory for mass-polydisperse colloidal systems. *J. Chem. Phys.* **157**, (2022).

51. Liu, J., Sun, Z.-W. & AA, Y. Non-Gravitational Effects with Density-Matching in Evaluating the Influence of Sedimentation of Colloidal Coagulation. *Chinese Phys. Lett.* **22**, 3199–3202 (2005).

52. McMackin, P. M. *et al.* Simulated microgravity in the ring-sheared drop. *npj Microgravity* **6**, 1–7 (2020).

53. Kodger, T. E., Guerra, R. E. & Sprakel, J. Precise colloids with tunable interactions for confocal microscopy. *Sci. Rep.* **5**, 1–10 (2015).

54. Royall, C. P., Poon, W. C. K. & Weeks, E. R. In search of colloidal hard spheres. *Soft Matter* **9**, 17–27 (2013).

55. Witze, A. Astronauts have conducted nearly 3,000 science experiments aboard the ISS. *Nature* (2020).

56. Lämmerzahl, C. *et al.* Experiments in Fundamental Physics Scheduled and in Development for the ISS. *Gen. Relativ. Gravit.* **36**, 615–651 (2004).

57. Seibert, G. *The history of sounding rockets and their contribution to European Space Research*. *European Space Agency - History Study Reports ESA HSR* (2006).

58. Shelhamer, M. Parabolic flight as a spaceflight analog. *J. Appl. Physiol.* **120**, 1442–1448 (2016).

59. Kufner, E. *et al.* ESA's drop tower utilisation activities 2000 to 2011. *Microgravity Sci. Technol.* **23**, 409–425 (2011).

60. Kiss, J. Z. Plant biology in reduced gravity on the Moon and Mars. *Plant Biol.* **16**, 12–17 (2014).

61. Van Zoest, T. *et al.* Bose-einstein condensation in microgravity. *Science (80-.).* **328**, 1540–1543 (2010).

62. DiFrancesco, J. M. & Olson, J. M. The economics of microgravity research. *npj Microgravity* **1**, 1–6 (2015).

63. Hassan, P. A., Rana, S. & Verma, G. Making sense of Brownian motion: Colloid characterization by dynamic light scattering. *Langmuir* **31**, 3–12 (2015).

64. Modena, M. M., Rühle, B., Burg, T. P. & Wuttke, S. Nanoparticle Characterization: What to Measure? *Adv. Mater.* **31**, 1–26 (2019).

65. Tobler, D. J., Shaw, S. & Benning, L. G. Quantification of initial steps of nucleation and growth of silica nanoparticles: An in-situ SAXS and DLS study. *Geochim. Cosmochim. Acta* **73**, 5377–5393 (2009).

66. Carl, N., Prévost, S., Fitzgerald, J. P. S. & Karg, M. Salt-induced cluster formation of gold nanoparticles followed by stopped-flow SAXS, DLS and extinction spectroscopy. *Phys. Chem. Chem. Phys.* **19**, 16348–16357 (2017).

67. Anaraki, N. I. *et al.* New approach for time-resolved and dynamic investigations on nanoparticles agglomeration. *Nano Res.* **13**, 2847–2856 (2020).

68. Chen, K. L., Mylon, S. E. & Elimelech, M. Enhanced aggregation of alginate-coated iron oxide (Hematite) nanoparticles in the presence of calcium, strontium, and barium cations. *Langmuir* **23**, 5920–5928 (2007).

69. Keene, A. M. & Tyner, K. M. Analytical characterization of gold nanoparticle primary particles, aggregates, agglomerates, and agglomerated aggregates. *J. Nanoparticle Res.* **13**, 3465–3481 (2011).

70. Lazzari, S. *et al.* Colloidal stability of polymeric nanoparticles in biological fluids. *J. Nanoparticle Res.* **14**, 1–10 (2012).

71. Nelson, A. & Cosgrove, T. Dynamic light scattering studies of poly(ethylene oxide) adsorbed on laponite: Layer conformation and its effect on particle stability. *Langmuir* **20**, 10382–10388 (2004).

72. Lorber, B., Fischer, F., Bailly, M., Roy, H. & Kern, D. Protein analysis by dynamic light scattering: Methods and techniques for students. *Biochem. Mol. Biol. Educ.* **40**, 372–382 (2012).

73. Arzenšek, D., Podgornik, R. & Kuzman, D. Dynamic light scattering and application to proteins in solution. in *Seminar, Department of Physics, University of Ljubljana* (2010).

74. Mazzoni, S. *et al.* SODI-COLLOID: A combination of static and dynamic light scattering on board the International Space Station. *Rev. Sci. Instrum.* **84**, (2013).

75. Okubo, T. *et al.* Kinetic study of the formation reaction of colloidal silica spheres in

microgravity using aircraft. *Colloid Polym. Sci.* **277**, 474–478 (1999).

76.   Rogers, R. B. *et al.* Compact laser light-scattering instrument for microgravity research. *Appl. Opt.* **36**, 7493 (1997).

77.   Weitz, D. A. *et al.* Results from the Physics of Colloids experiment on ISS. in *53rd International Astronautical Congress* **No. IAC–02**, (2002).

78.   Mazzoni, S. *et al.* SODI-COLLOID: A combination of static and dynamic light scattering on board the International Space Station. *Rev. Sci. Instrum.* **84**, 1–10 (2013).

79.   Priecel, P., Salami, H. A., Padilla, R. H., Zhong, Z. & Lopez-Sanchez, J. A. Anisotropic gold nanoparticles: Preparation and applications in catalysis. *Chinese J. Catal.* **37**, 1619–1650 (2016).

80.   Boisselier, E. & Astruc, D. Gold nanoparticles in nanomedicine: preparations, imaging, diagnostics, therapies and toxicity. *Chem. Soc. Rev.* **38**, 1759–1782 (2009).

81.   Korotcenkov, G., Brinzari, V. & Cho, B. K. Conductometric gas sensors based on metal oxides modified with gold nanoparticles: a review. *Microchim. Acta* **183**, 1033–1054 (2016).

82.   Falahati, M. *et al.* Gold nanomaterials as key suppliers in biological and chemical sensing, catalysis, and medicine. *Biochim. Biophys. Acta - Gen. Subj.* **1864**, 1–27 (2020).

83.   Priyadarshini, E. & Pradhan, N. Gold nanoparticles as efficient sensors in colorimetric detection of toxic metal ions: A review. *Sensors Actuators B Chem. B Chem.* **238**, 888–902 (2017).

84.   Bardajee, G. R., Mizani, F. & Hosseini, S. S. pH sensitive release of doxorubicin anticancer drug from gold nanocomposite hydrogel based on poly(acrylic acid) grafted onto salep biopolymer. *J. Polym. Res.* **24**, 1–13 (2017).

85.   Fazio, E. *et al.* Laser light triggered smart release of silibinin from a PEGylated-PLGA gold nanocomposite. *J. Mater. Chem. B* **3**, 9023–9032 (2015).

86.   Zhao, X. *et al.* Thermoswitchable electronic properties of a gold nanoparticle/hydrogel composite. *Macromol. Rapid Commun.* **26**, 1784–1787 (2005).

87.   Doblas, D., Hubertus, J., Kister, T. & Kraus, T. A Translucent Nanocomposite with Liquid Inclusions of a Responsive Nanoparticle Dispersion. *Adv. Mater.* **30**, 1–6 (2018).

88.   Huang, D., Liao, F., Molesa, S., Redinger, D. & Subramanian, V. Plastic-Compatible Low Resistance Printable Gold Nanoparticle Conductors for Flexible Electronics. *J. Electrochem. Soc.* **150**, G412 (2003).

89.   Rajan, K. *et al.* Silver nanoparticle ink technology: State of the art. *Nanotechnol. Sci. Appl.* **9**, 1–13 (2016).

90.   Jeong, S. *et al.* Stable aqueous based Cu nanoparticle ink for printing well-defined highly conductive features on a plastic substrate. *Langmuir* **27**, 3144–3149 (2011).

91.   Doblas, D., Hubertus, J., Kister, T. & Kraus, T. A Translucent Nanocomposite with Liquid Inclusions of a Responsive Nanoparticle Dispersion. *Adv. Mater.* **30**, 1803159 (2018).

92.   Srivastava, M., Srivastava, S. K., Nirala, N. R. & Prakash, R. A chitosan-based polyaniline-Au nanocomposite biosensor for determination of cholesterol. *Anal. Methods* **6**, 817–824 (2014).

93.   Xian, Y. *et al.* Glucose biosensor based on Au nanoparticles-conductive polyaniline nanocomposite. *Biosens. Bioelectron.* **21**, 1996–2000 (2006).

94.   Kister, T., Monego, D., Mulvaney, P., Widmer-Cooper, A. & Kraus, T. Colloidal Stability of Apolar Nanoparticles: The Role of Particle Size and Ligand Shell Structure. *ACS Nano* **12**, 5969–5977 (2018).

95.   Monego, D. *et al.* Colloidal Stability of Apolar Nanoparticles: Role of Ligand Length. *Langmuir* **34**, 12982–12989 (2018).

96.   Born, P. & Kraus, T. Ligand-dominated temperature dependence of agglomeration kinetics and morphology in alkyl-thiol-coated gold nanoparticles. *Phys. Rev. E - Stat. Nonlinear, Soft Matter Phys.* **87**, (2013).

97.   Doblas, D., Kister, T., Cano-Bonilla, M., González-García, L. & Kraus, T. Colloidal Solubility and Agglomeration of Apolar Nanoparticles in Different Solvents. *Nano Lett.* **19**, 5246–5252 (2019).

98.   Potenza, M. A. C., Veen, S. J., Schall, P. & Wegdam, G. H. Nucleation of weakly attractive aggregates in microgravity. *Epl* **124**, (2018).

99.   Von Kampen, P., Kaczmarczik, U. & Rath, H. J. The new Drop Tower catapult system. *Acta Astronaut.* **59**, 278–283 (2006).

100. Saba, H. A Review on Nanoparticles: Their Synthesis and Types. *Res. J. Recent Sci. Res . J . Recent . Sci . Uttar Pradesh (Lucknow Campus)* **4**, 1–3 (2014).

101. Murray, R. W. Nanoelectrochemistry: Metal nanoparticles, nanoelectrodes, and nanopores. *Chem. Rev.* **108**, 2688–2720 (2008).

102. Mohanraj, V. J. & Chen, Y. Nanoparticles - A review. *Trop. J. Pharm. Res.* **5**, 561–573 (2007).

103. Ghosh Chaudhuri, R. & Paria, S. Core/shell nanoparticles: Classes, properties, synthesis mechanisms, characterization, and applications. *Chem. Rev.* **112**, 2373–2433 (2012).

104. Ealias, A. M. & Saravanakumar, M. P. A review on the classification, characterisation, synthesis of nanoparticles and their application. *IOP Conf. Ser. Mater. Sci. Eng.* **263**, 1–15 (2017).

105. Holister, P., Weener, J.-W., Vas, C. R., Harper, T. & Cientifica. Nanoparticles: Technology White Paper No.3. *Científica* 11 (2003).

106. Joudeh, N. & Linke, D. Nanoparticle classification, physicochemical properties, characterization, and applications: a comprehensive review for biologists. *J. Nanobiotechnology* **20**, 1–29 (2022).

107. Dijk, M. A. Van, Tchebotareva, A. L., Orrit, M., Lippitz, M. & Berciaud, S. Absorption and scattering microscopy of single metal nanoparticles. *Phys. Chem. Chem. Phys.* **8**, 3486–3495 (2006).

108. Link, S. & El-sayed, M. A. Shape and size dependence of radiative , non- radiative and photothermal properties of gold nanocrystals. *Int. Rev. Phys. Chem.* **19**, 409–453 (2000).

109. Guisbiers, G., Mejía-Rosales, S. & Leonard Deepak, F. Nanomaterial properties: Size and shape dependencies. *J. Nanomater.* **2012**, 2012–2014 (2012).

110. Rao, C. N. R., Kulkarni, G. U., Thomas, P. J. & Edwards, P. P. Metal nanoparticles and their assemblies. *Chem. Soc. Rev.* **29**, 27–35 (2000).

111. Mallakpour, S. & Madani, M. A review of current coupling agents for modification of metal oxide nanoparticles. *Prog. Org. Coatings* **86**, 194–207 (2015).

112. Grieve, K., Mulvaney, P. & Grieser, F. Synthesis and electronic properties of semiconductor nanoparticles/quantum dots. *Curr. Opin. Colloid Interface Sci.* **5**, 168–

172 (2000).

113. Gupta, S. M. & Tripathi, M. An overview of commonly used semiconductor nanoparticles in photocatalysis. *High Energy Chem.* **46**, 1–9 (2012).

114. Holmannova, D., Borsky, P., Svadlakova, T., Borska, L. & Fiala, Z. Carbon Nanoparticles and Their Biomedical Applications. *Appl. Sci.* **12**, 1–21 (2022).

115. Lim, J. V., Bee, S. T., Sin, L. T., Ratnam, C. T. & Hamid, Z. A. A. A review on the synthesis, properties, and utilities of functionalized carbon nanoparticles for polymer nanocomposites. *Polymers (Basel).* **13**, 1–45 (2021).

116. Chang, H. & Sun, S. Q. Silicon nanoparticles: Preparation, properties, and applications. *Chinese Phys. B* **23**, 1–14 (2014).

117. O'Farrell, N., Houlton, A. & Horrocks, B. R. Silicon nanoparticles: Applications in cell biology and medicine. *Int. J. Nanomedicine* **1**, 451–472 (2006).

118. Rao, J. P. & Geckeler, K. E. Polymer nanoparticles: Preparation techniques and size-control parameters. *Prog. Polym. Sci.* **36**, 887–913 (2011).

119. Mavila, S., Eivgi, O., Berkovich, I. & Lemcoff, N. G. Intramolecular Cross-Linking Methodologies for the Synthesis of Polymer Nanoparticles. *Chem. Rev.* **116**, 878–961 (2016).

120. Roy, A. *et al.* Biologically Derived Gold Nanoparticles and Their Applications. *Bioinorg. Chem. Appl.* **2022**, 1–13 (2022).

121. Corti, C. W., Holliday, R. J. & Thompson, D. T. Developing New Industrial Applications for Gold : Gold Nanotechnology. *Gold Bull.* **35**, 111–117 (2002).

122. Durán, N. & Marcato, P. D. Review Nanobiotechnology perspectives . Role of nanotechnology in the food industry : a review. *Int. J. Food Sci. Technol.* **48**, 1127–1134 (2013).

123. Stark, W. J., Stoessel, P. R., Wohlleben, W. & Hafner, A. Industrial applications of nanoparticles. *Chem. Soc. Rev.* **44**, 5793–5805 (2015).

124. Fazio, E. *et al.* Laser light triggered smart release of silibinin from a PEGylated-PLGA gold nanocomposite. *J. Mater. Chem. B* **3**, 9023–9032 (2015).

125. Siddique, S. & Chow, J. C. L. Gold nanoparticles for drug delivery and cancer therapy.

Appl. Sci. **10**, 1–21 (2020).

126. Srivastava, M., Srivastava, S. K., Nirala, N. R. & Prakash, R. A chitosan-based polyaniline-Au nanocomposite biosensor for determination of cholesterol. *Anal. Methods* **6**, 817–824 (2014).

127. Masud, M. K. *et al.* Nanostructured mesoporous gold biosensor for microRNA detection at attomolar level. *Biosens. Bioelectron.* **168**, 112429 (2020).

128. Afzal, A. B., Akhtar, M. J., Nadeem, M. & Hassan, M. M. Investigation of structural and electrical properties of polyaniline/gold nanocomposites. *J. Phys. Chem. C* **113**, 17560–17565 (2009).

129. Li, J. *et al.* Flexible, conductive, porous, fibrillar polymer-gold nanocomposites with enhanced electromagnetic interference shielding and mechanical properties. *J. Mater. Chem. C* **5**, 1095–1105 (2017).

130. Tiyyagura, H. R., Majerič, P., Bračič, M., Anžel, I. & Rudolf, R. Gold inks for inkjet printing on photo paper: Complementary characterisation. *Nanomaterials* **11**, 1–13 (2021).

131. Mekhmouken, S. *et al.* Gold nanoparticle-based eco-friendly ink for electrode patterning on flexible substrates. *Electrochem. commun.* **123**, 1–4 (2021).

132. Piella, J., Bastús, N. G. & Puntes, V. Size-Controlled Synthesis of Sub-10-nanometer Citrate-Stabilized Gold Nanoparticles and Related Optical Properties. *Chem. Mater.* **28**, 1066–1075 (2016).

133. Turkevich, J. & Enüstün, B. V. Coagulation of Colloidal Gold. *J. Am. Chem. Soc.* **85**, 3317–3328 (1963).

134. Brown, K. R. & Natan, M. J. Hydroxylamine seeding of colloidal Au nanoparticles in solution and on surfaces. *Langmuir* **14**, 726–728 (1998).

135. Sau, T. K. & Murphy, C. J. Seeded High Yield Synthesis of Short Au Nanorods in Aqueous Solution. *Langmuir* **20**, 6414–6420 (2004).

136. Sau, T. K. & Murphy, C. J. Room Temperature , High-Yield Synthesis of Multiple Shapes of Gold Nanoparticles in Aqueous Solution. *JACS Commun.* **126**, 8648–8649 (2004).

137. Mandal, S., Phadtare, S., Pasricha, R. & Sastry, M. Capping of Gold Nanoparticles by the Amino Acid Lysine Renders Them Water-Dispersible. *Langmuir* **19**, 3545–3549 (2003).

138. Bogdanov, A. a *et al.* Gold Nanoparticles Stabilized with MPEG-Grafted Poly(L-lysine): in Vitro and in Vivo Evaluation of a Potential Theranostic Agent. *Bioconjug. Chem.* **26**, 39–50 (2015).

139. Laaksonen, T., Ahonen, P., Johans, C. & Kontturi, K. Stability and Electrostatics of Mercaptoundecanoic Acid-Capped Gold Nanoparticles with Varying Counterion Size. *ChemPhysChem* **7**, 2143–2149 (2006).

140. Bajpai, S. K., Mohan, Y. M., Bajpai, M., Tankhiwale, R. & Thomas, V. Synthesis of polymer stabilized silver and gold nanostructures. *J. Nanosci. Nanotechnol.* **7**, 1–17 (2007).

141. Sánchez-Iglesias, A. *et al.* Reversible Clustering of Gold Nanoparticles under Confinement. *Angew. Chemie* **130**, 3237–3240 (2018).

142. Corbierre, M. K. *et al.* Polymer-stabilized gold nanoparticles and their incorporation into polymer matrices. *J. Am. Chem. Soc.* **123**, 10411–10412 (2001).

143. Liu, Y., Cheng, S. Z. D., Wen, X. & Hu, J. Preparing and Stabilizing Colloidal Nanoparticles with a Helical Synthetic Polymer. *Langmuir* **18**, 10500–10502 (2002).

144. Benkovičová, M. *et al.* Preparation of sterically stabilized gold nanoparticles for plasmonic applications. *Chem. Pap.* **67**, 1225–1230 (2013).

145. Daniel, M. & Astruc, D. Gold Nanoparticles: Assembly , Supramolecular Chemistry , Quantum-Size-Related Properties , and Applications toward Biology , Catalysis , and Nanotechnology. *Chem. Rev.* **104**, 293–346 (2004).

146. Weitz, D. A., Huang, J. S., Lin, M. Y. & Sung, J. Dynamics of Diffusion-Limited Kinetic Aggregation. *Phys. Rev. Lett.* **53**, 1657–1660 (1984).

147. Leite, F. L. *et al.* Nanoscale conformational ordering in polyanilines investigated by SAXS and AFM. *J. Colloid Interface Sci.* **316**, 376–387 (2007).

148. Chen, X., Wang, J., Pan, R., Roth, S. & Förster, S. Insights into Growth Kinetics of Colloidal Gold Nanoparticles: In Situ SAXS and UV-Vis Evaluation. *J. Phys. Chem. C* **125**, 1087–1095 (2021).

149. Pontoni, D., Narayanan, T. & Rennie, A. R. Time-resolved SAXS study of nucleation and growth of silica colloids. *Langmuir* **18**, 56–59 (2002).

150. Bolze, J. *et al.* Formation and growth of amorphous colloidal CaCO3 precursor particles

as detected by time-resolved SAXS. *Langmuir* **18**, 8364–8369 (2002).

151. Ballauff, M. SAXS and SANS studies of polymer colloids. *Curr. Opin. Colloid Interface Sci.* **6**, 132–139 (2001).

152. Hura, G. L. *et al.* Comprehensive macromolecular conformations mapped by quantitative SAXS analyses. *Nat. Methods* **10**, 453–454 (2013).

153. Brosey, C. A. & Tainer, J. A. Evolving SAXS versatility: solution X-ray scattering for macromolecular architecture, functional landscapes, and integrative structural biology. *Curr. Opin. Struct. Biol.* **58**, 197–213 (2019).

154. Mertens, H. D. T. & Svergun, D. I. Structural characterization of proteins and complexes using small-angle X-ray solution scattering. *J. Struct. Biol.* **172**, 128–141 (2010).

155. Lipfert, J. & Doniach, S. Small-angle X-ray scattering from RNA, proteins, and protein complexes. *Annu. Rev. Biophys. Biomol. Struct.* **36**, 307–327 (2007).

156. Li, T., Senesi, A. J. & Lee, B. Small Angle X-ray Scattering for Nanoparticle Research. *Chem. Rev.* **116**, 11128–11180 (2016).

157. Schwamberger, A. *et al.* Combining SAXS and DLS for simultaneous measurements and time-resolved monitoring of nanoparticle synthesis. *Nucl. Instruments Methods Phys. Res. Sect. B Beam Interact. with Mater. Atoms* **343**, 116–122 (2015).

158. Garcia, P. R. A. F. *et al.* An in situ SAXS investigation of the formation of silver nanoparticles and bimetallic silver-gold nanoparticles in controlled wet-chemical reduction synthesis. *Nanoscale Adv.* **2**, 225–238 (2020).

159. Pavlopoulou, E. *et al.* Following the synthesis of metal nanoparticles within pH-Responsive microgel particles by SAXS. *Macromolecules* **43**, 9828–9836 (2010).

160. Loubat, A. *et al.* Growth and self-assembly of ultrathin au nanowires into expanded hexagonal superlattice studied by in situ SAXS. *Langmuir* **30**, 4005–4012 (2014).

161. Bonini, M., Fratini, E. & Baglioni, P. SAXS study of chain-like structures formed by magnetic nanoparticles. *Mater. Sci. Eng. C* **27**, 1377–1381 (2007).

162. Paik, T., Ko, D.-K., Gordon, T. R., Doan-Nguyen, V. & Murray, C. B. Studies of Liquid Crystalline Self-Assembly of GdF3 Nanoplates by In-Plane, Out-of-Plane SAXS. *ACS Nano* **5**, 8322–8330 (2011).

163. Appel, C., Kuttich, B., Kraus, T. & Stühn, B. In situ investigation of temperature induced agglomeration in non-polar magnetic nanoparticle dispersions by small angle X-ray scattering. *Nanoscale* **13**, 6916–6920 (2021).

164. Bonini, M., Fratini, E. & Baglioni, P. SAXS study of chain-like structures formed by magnetic nanoparticles. *Mater. Sci. Eng. C* **27**, 1377–1381 (2007).

165. Özkan, E. *et al.* Peering into the Formation of Cerium Oxide Colloidal Particles in Solution by in Situ Small-Angle X-ray Scattering. *Langmuir* **36**, 9175–9190 (2020).

166. Chen, Z. H. *et al.* Characterizing size and porosity of hollow nanoparticles: SAXS, SANS, TEM, DLS, and adsorption isotherms compared. *Langmuir* **28**, 15350–15361 (2012).

167. Wertheim, M. S. Exact solution of the percus-yevick integral equation for hard spheres. *Phys. Rev. Lett.* **10**, 321–323 (1963).

168. Ashcroft, N. W. & Lekner, J. Structure and resistivity of liquid metals. *Phys. Rev.* **145**, 83–90 (1966).

169. Wagner, J., Härtl, W. & Hempelmann, R. Characterization of Monodisperse Colloidal Particles: Comparison between SAXS and DLS. *Langmuir* **16**, 4080–4085 (2000).

170. National Institute for Standards and Technology – Center for Neutron Research, Neutron activation and scattering calculator. *https://www.ncnr.nist.gov/resources/activation/*

171. Bhattacharjee, S. DLS and zeta potential - What they are and what they are not? *J. Control. Release* **235**, 337–351 (2016).

172. Eaton, P. *et al.* A direct comparison of experimental methods to measure dimensions of synthetic nanoparticles. *Ultramicroscopy* **182**, 179–190 (2017).

173. Wagner, J., Härtl, W. & Hempelmann, R. Characterization of monodisperse colloidal particles: comparison between SAXS and DLS. *Langmuir* **16**, 4080–4085 (2000).

174. Chu, B., Wang, Z. & Yu, J. Dynamic Light Scattering Study of Internal Motions of Polymer Coils in Dilute Solution. *Macromolecules* **24**, 6832–6838 (1991).

175. Stetefeld, J., McKenna, S. A. & Patel, T. R. Dynamic light scattering: a practical guide and applications in biomedical sciences. *Biophys. Rev.* **8**, 409–427 (2016).

176. Ferré-D'Amaré, A. R. & Burley, S. K. Use of dynamic light scattering to assess

crystallizability of macromolecules and macromolecular assemblies. *Structure* **2**, 357–359 (1994).

177.   Lorber, B., Fischer, F., Bailly, M., Roy, H. & Kern, D. Protein Analysis by Dynamic Light Scattering: Methods and Techniques for Students. *Biochem. Mol. Biol. Educ.* **40**, 372–382 (2012).

178.   Xu, R. Light scattering: A review of particle characterization applications. *Particuology* **18**, 11–21 (2015).

179.   Comtois, P. John Tyndall and the floating matter of the air. *Aerobiologia (Bologna).* **17**, 193–202 (2001).

180.   Tyndall, J. On the Blue Colour of the Sky, and the Polarization of Sky-light, and on the Polarization of Light by Cloudy matter generally. *Proc. R. Soc. London 17* 223–233 (1869).

181.   Zhao, G., Bi, S., Fröna, A. P. & Wu, J. Liquid Viscosity and Surface Tension of R1234yf and R1234ze Under Saturation Conditions by Surface Light Scattering. *J. Chem. Eng. Data* **59**, 1366–1371 (2014).

182.   Strutt, J. W. On the light from the sky, its polarization and colour. *London, Edinburgh, Dublin Philos. Mag. J. Sci.* **41**, 274–279 (1871).

183.   Hon. J.W. Strutt (1871) LVIII. On the scattering of light by small particles, The London, Edinburgh, and Dublin Philosophical Magazine and Journal of Science, 41:275, 447-454.

184.   Hon. J.W. Strutt (1871) XXXVI. On the light from the sky, its polarization and colour, The London, Edinburgh, and Dublin Philosophical Magazine and Journal of Science, 41:273, 274-279.

185.   Mie, G. Beiträge zur Optik trüber Medien, speziell kolloidaler Metallösungen. *Ann. Phys.* **330**, 377–445 (1908).

186.   Debye, P. Zerstreuung von Röntgenstrahlen. *Ann. Phys.* **351**, 809–823 (1915).

187.   Yang, H., Zheng, G. & Li, M. C. A discussion of noise in dynamic light scattering for particle sizing. *Part. Part. Syst. Charact.* **25**, 406–413 (2009).

188.   Einstein, A. Über die von der molekularkinetischen Theorie der Wärme geforderte Bewegumg von in ruhenden Flüssigkeiten suspendierten Teilchen. *Ann. d. Phys.* **322**,

549–560 (1905).

189. Hoo, C. M., Starostin, N., West, P. & Mecartney, M. L. A comparison of atomic force microscopy (AFM) and dynamic light scattering (DLS) methods to characterize nanoparticle size distributions. *J. Nanoparticle Res.* **10**, 89–96 (2008).

190. Pecora, R. Dynamic light scattering measurement of nanometer particles in liquids. *J. Nanoparticle Res.* **2**, 123–131 (2000).

191. Smoluchowski, M. Zur kinetischen Theorie der Brownschen Molekularbewegung und der Suspensionen. *Ann. Phys.* **326**, 756–780 (1906).

192. Bingham, N. H. & Dunham, B. Estimating diffusion coefficients from count data: Einstein-smoluchowski theory revisited. *Ann. Inst. Stat. Math.* **49**, 667–679 (1997).

193. Miller, C. C. The Stokes-Einstein Law for Diffusion in Solution. *Proc. R. Soc. Lond. A* **106**, 724–749 (1924).

194. Cappelezzo, M., Capellari, C. A., Pezzin, S. H. & Coelho, L. A. F. Stokes-Einstein relation for pure simple fluids. *J. Chem. Phys.* **126**, 1–5 (2007).

195. Goldburg, W. I. Dynamic light scattering Dynamic light scattering. *Am. J. Phys.* **67**, 1152–1160 (1999).

196. Pyttlik, A., Kuttich, B. & Kraus, T. Dynamic Light Scattering on Nanoparticles in Microgravity in a Drop Tower. *Microgravity Sci. Technol.* **34**, 1–11 (2022).

197. Gabriel, J., Blochowicz, T. & Stühn, B. Compressed exponential decays in correlation experiments: The influence of temperature gradients and convection. *J. Chem. Phys.* **142**, (2015).

198. An, X., Zhao, H., Jiang, F., Mao, C. & Shen, W. The coexistence curves of {xC6H5NO2 + (1 - X)CH3(CH2)12CH3} in the critical region. *J. Chem. Thermodyn.* **29**, 1047–1054 (1997).

199. Zhang, L. *et al.* Densities and Viscosities of Binary Mixtures of exo - Tetrahydrodicyclopentadiene with N -Undecane or N -Tetradecane at T) (293 . 15 to 313 . 15) K. *J. Chem. Eng. Data* **55**, 4108–4113 (2010).

200. Hernández-Galván, M. A., García-Sánchez, F. & Macías-Salinas, R. Liquid viscosities of benzene, n-tetradecane, and benzene + n-tetradecane from 313 to 393 K and pressures

up to 60 MPa: Experiment and modeling. *Fluid Phase Equilib.* **262**, 51–60 (2007).

201.   Tânia, V. M., Santos, M., Pereira, F. V & Helena, M N T.Avelino, Fernando J.P.Caetano, J. M. N. A. F. F. P. E. Erratum to 'Viscosity and density measurements on liquid n-tetradecane at moderately high pressures' [Fluid Phase Equil. 453 15 December 2017 46–57]. *Fluid Phase Equilib.* **456**, 203–203 (2018).

202.   Khodier, S. A. Refractive index of standard oils as a function of wavelength and temperature. *Opt. Laser Technol.* **34**, 125–128 (2002).

203.   Lehmann, M. *et al.* DLS Setup for in Situ Measurements of Photoinduced Size Changes of Microgel-Based Hybrid Particles. *Langmuir* **34**, 3597–3603 (2018).

204.   Babick, F. *Dynamic light scattering (DLS)*. *Characterization of Nanoparticles: Measurement Processes for Nanoparticles* (Elsevier Inc., 2019).

205.   Veen, S. J. *et al.* Colloidal aggregation in microgravity by critical Casimir forces. *Phys. Rev. Lett.* **109**, 1–5 (2012).

206.   Harland, D. M. microgravity. *Encycl. Br.* 2023–2024 (2024).

207.   Snell, E. H. & Helliwell, J. R. Microgravity as an environment for macromolecular crystallization – an outlook in the era of space stations and commercial space flight crystallization – an outlook in the era of space stations and ABSTRACT. *Crystallogr. Rev.* 1–44 (2021).

208.   Graybiel, A. & Orientation, S. Motor function in microgravity: movement in weightlessness James R Lackner 1 and Paul DiZio 2. *Curr. Opin. Neurobiol.* **6**, 744–750 (1996).

209.   Chandler, D. Weightlessness and Microgravity. *Phys. Teach. - Mointclaire High Sch.* 312–313 (1991).

210.   Y. Malméjac, A. Bewersdorff, I. D. R. & L. G. G. N. Challenges & Prospectives of Microgravity Research in Space. *esa BR-05* **ISSN 0250**-, 1–77 (1981).

211.   Maier, J. A. M., Cialdai, F., Monici, M. & Morbidelli, L. The impact of microgravity and hypergravity on endothelial cells. *Biomed Res. Int.* **2015**, (2015).

212.   Eberspeaker, P. J. & Pierce, D. L. An Overview of the NASA Sounding Rockets and Balloon Programs. in *20th Symposium on European Rocket and Ballon Programmes and*

Related Research **700**, (2011).

213. Könemann, T. *et al.* Concept for a next-generation drop tower system. *Adv. Sp. Res.* **55**, 1728–1733 (2015).

214. Beysens, D. A. & Van Loon, J. J. W. A. *Generation and Applications of Extra- Terrestrial Environments on Earth*. *River Publishers* **6**, (2015).

215. Liu, T. Y., Wu, Q. P., Sun, B. Q. & Han, F. T. Microgravity Level Measurement of the Beijing Drop Tower Using a Sensitive Accelerometer. *Sci. Rep.* **6**, 1–9 (2016).

216. Arjun, B. J., Manu, N. M., Muruganandam, T. . & Amit, K. Experiments in reduced gravity space environment using 1.1 second drop tower and challenges involved. in *Proceeding of the 2nd National Propulsion Confercne NPC-2015* 1–9 (2015).

217. Thompson, M. Zero Gravity User ' s Guide Facility. *Natl. Aeronaut. Sp. Adminstration* 1–27 (1999).

218. Karmali, F. & Shelhamer, M. The dynamics of parabolic flight: Flight characteristics and passenger percepts. *Acta Astronaut.* **63**, 594–602 (2008).

219. Schmidt, W. Quickly changing acceleration forces (QCAFs) vibration analysis on the A300 ZERO-G. *Microgravity Sci. Technol.* **15**, 42–48 (2004).

220. Altenbuchner, L. *et al.* MORABA – Overview on DLR's Mobile Rocket Base and Projects. *SpaceOps* 1–10 (2012).

221. Schütte, A. & Grothe, D. Sounding Rocket Programm: MINITEXUS; TEXUS and MAXUS. in *17th ESA Symposium on European Rocket and Balloon Programmes and Related Research* 481–485 (2005).

222. Sabbatini, M. & Sentse, N. European Users Guide to Low Gravity Platforms. in *Sounding Rockets* 1–47 (2010).

223. O'Malley, T. F. & Weiland, K. J. The FCF combustion integrated rack: Microgravity combustion science on board the international space station. in *2001 Conference and Exhibit on International Space Station Utilization* 1–11 (2001).

224. Thirsk, R., Andre, K., Mukai, C. & David, W. The space-flight environment: the International Space. *Cmaj* **180**, 1216–1220 (2009).

225. Lösch, S., Iles, G. N., Schmitz, B. & Günther, B. H. Agglomeration of Ni-nanoparticles in

the gas phase under gravity and microgravity conditions. *J. Phys. Conf. Ser.* **327**, 012036 (2011).

226. DeLucas, L. J. *et al.* Protein crystal growth in microgravity. *Science (80-.).* **246**, 651–654 (1989).

227. Long, M. M. *et al.* Protein crystal growth in microgravity-temperature induced large scale crystallization of insulin. *Microgravity Sci. Technol.* **7**, 196—202 (1994).

228. Littke, W. & John, C. Protein single crystal growth under microgravity. *Science (80-.).* **225**, 203–204 (1984).

229. Cheng, Z., Zhu, J., Russel, W. B., Meyer, W. V. & Chaikin, P. M. Colloidal hard-sphere crystallization kinetics in microgravity and normal gravity. *Appl. Opt.* **40**, 4146 (2001).

230. Freed, L. E. & Vunjak-Novakovic, G. Microgravity tissue engineering. *Vitr. Cell. Dev. Biol. - Anim.* **33**, 381–385 (1997).

231. Barzegari, A. & Saei, A. A. An update to space biomedical research: Tissue engineering in microgravity bioreactors. *BioImpacts* **2**, 23–32 (2012).

232. Rogers, R. B. *et al.* Compact laser light-scattering instrument for microgravity research. *Appl. Opt.* **36**, 7493–7500 (1997).

233. Manley, S. *et al.* Limits to gelation in colloidal aggregation. *Phys. Rev. Lett.* **93**, 2–5 (2004).

234. Schoen, Herbert, M., Grove Jr, C. S. & Palermo, J. A. The early history of crystallization. *J. Chem. Educ.* **33**, 373 (1956).

235. Giegé, R. A historical perspective on protein crystallization from 1840 to the present day. *FEBS J.* **280**, 6456–6497 (2013).

236. Luft, J. R., Newman, J. & Snell, E. H. Crystallization screening: The influence of history on current practice. *Acta Crystallogr. Sect. FStructural Biol. Commun.* **70**, 835–853 (2014).

237. Kulkarni, S. J. A Review on Studies and Research on Crystallization. *Int. J. Res. Rev.* **2**, 615–618 (2015).

238. Chemistry, R. Reactive Crystallization: A Review. *React. Chem. Eng.* (2020).

239. Gao, Z., Rohani, S., Gong, J. & Wang, J. Recent Developments in the Crystallization Process: Toward the Pharmaceutical Industry. *Engineering* **3**, 343–353 (2017).

240. Mcpherson, A. Introduction to protein crystallization. *Methods* **34**, 254–265 (2004).

241. Friedmann, D. Crystallization of Macromolecules. *Curr Protoc Protein Sci* 1–34 (2004).

242. McPherson, A. Two approaches to the rapid screening of crystallization conditions. *J. Cryst. Growth* **122**, 161–167 (1992).

243. McPherson, A. The Role of X-Ray Crystallography in Structure-Based Rational Drug Design. in *Chemical and Structural Approaches to Rational Drug Design* 19 (CRC Press, 1994).

244. Bernal, J. D. & Crowfoot, D. X-Ray Photographs of Crystalline Pepsin. *Nature* **133**, 794–795 (1934).

245. Perutz, M. F. The Hemoglobin Molecule. *Sci. Am.* **211**, 64–79 (1964).

246. Sumner, J. B. The Isolation and Crysttallization of the Enzyme Urease. *J. Biol. Chem.* **69**, 435–441 (1926).

247. Boddupalli, S. S. *et al.* Crystallization and preliminary x-ray diffraction analysis of P450terp and the hemoprotein domain of P450BM-3, enzymes belonging to two distinct classes of the cytochrome P450 superfamily. *Proc. Natl. Acad. Sci. U. S. A.* **89**, 5567–5571 (1992).

248. De Yoreo, J. J., Burnham, A. K. & Whitman, P. K. Developing KH2PO4 and KD2PO4 crystaks for the world's most power laser. *Int. Mater. Rev.* **47**, 113–152 (2002).

249. Liu, C. Y. & Bard, A. J. Optoelectronic properties and memories based on organic single-crystal thin films. *Acc. Chem. Res.* **32**, 235–245 (1999).

250. Vekilov, P. G. Nucleation. *Cryst. Growth Des.* **10**, 5007–5019 (2011).

251. Davey, R. J., Schroeder, S. L. M. & ter Horst, J. H. Nucleation of Organic Crystals - A Molecular Perspective. *Angew. Chemie Int. Ed. English* **52**, 2166–2179 (2013).

252. Gebauer, D., Gale, J. D. & Cölfen, H. Crystal Nucleation and Growth of Inorganic Ionic Materials from Aqueous Solution: Selected Recent Developments , and Implications. *small* **18**, 1–14 (2022).

253. Zhou, J., Zhou, Y. & Tang, W. Molecular Mechanism of Organic Crystal Nucleation: A Perspective of Solution Chemistry and Polymorphism. *crystals* **12**, 1–25 (2022).

254. Kashchiev, D. *Nucleation: Basic Theory with Applications*. (Butterworth-Heinemann, 2000).

255. Garciá-Ruiz, J. M., Otálora, F. & Garciá-Caballero, A. The role of mass transport in protein crystallization. *IYCr Cryst. Ser.* **F72**, 96–104 (2016).

256. Tomita, Y. *et al.* Crystallization of Charged Colloids under Microgravity during Aircraft Parabolic Flights. *Int. J. Microgravity Sci. Appl.* **35**, 1–6 (2018).

257. Xu, Z., Wang, L., Fang, F., Fu, Y. & Yin, Z. A Review on Colloidal Self-Assembly and their Applications. *Curr. Nanosci.* **12**, 725–746 (2016).

258. Kolluru, L. P., Atre, P. & Rizvi, S. A. A. Characterization and Applications of Colloidal Systems as Versatile Drug Delivery Carriers for Parenteral Formulations. *pharmaceuticals* **14**, 1–12 (2021).

259. Ise, N. & Sogami, I. *Structure formation in solution: ionic polymers and colloidal particles*. *Springer Science & Business Media* (2005).

260. Miki, H. *et al.* Clustering of charged colloidal particles in the microgravity environment of space. *npj Microgravity* **33**, 1–6 (2023).

261. Zvyagolskaya, O., Archer, A. J. & Bechinger, C. Criticality and phase separation in a two-dimensional binary colloidal fluid induced by the solvent critical behavior. *Europhys. Lett.* **96**, 1–6 (2011).

262. Bonn, D. *et al.* Direct observation of colloidal aggregation by critical casimir forces. *Phys. Rev. Lett.* **103**, 1–4 (2009).

263. Nguyen, V. D., Dang, M. T., Nguyen, T. A. & Schall, P. Critical Casimir forces for colloidal assembly. *J. Phys. Condens. Matter* **28**, 043001 (2016).

264. Maciołek, A. & Dietrich, S. Collective behavior of colloids due to critical Casimir interactions. *Rev. Mod. Phys.* **90**, 1–88 (2018).

265. Sketch of the structure of the ZARM drop tower in Bremen provided by the ZARM Institute in Bremen.

266. ZARM Drop Tower User Manual. in *Drop Tower Operation and Service Company ZARM*

FABmbH 1–42 (2012).

267. Selig, H., Dittus, H. & Lämmerzahl, C. Drop tower microgravity improvement towards the nano-g level for the MICROSCOPE payload tests. *Microgravity Sci. Technol.* **22**, 539–549 (2010).

268. Sketch of the catapult capsule and the capsule platform provided by the ZARM Institute in Bremen.

269. Wu, B. H., Yang, H. Y., Huang, H. Q., Chen, G. X. & Zheng, N. F. Solvent effect on the synthesis of monodisperse amine-capped Au nanoparticles. *Chinese Chem. Lett.* **24**, 457–462 (2013).

270. Mourdikoudis, S. & Liz-Marzán, L. M. Oleylamine in nanoparticle synthesis. *Chem. Mater.* **25**, 1465–1476 (2013).

271. Stenkamp, V. S. & Berg, J. C. The role of long tails in steric stabilization and hydrodynamic layer thickness. *Langmuir* **13**, 3827–3832 (1997).

272. Hinman, S. S. *Plasmonic Interrogation of Biomimetic Systems for Enhanced Toxicity Assays*. *Dissertation, University of California Riverside* (2017).

273. Wang, Y. *et al.* Self-assembled gold nanorime mesh conductors for invisible stretchable supercapacitors. *Nanoscale* **10**, 15948–15955 (2018).

274. Pyttlik, A., Kuttich, B. & Kraus, T. Microgravity Removes Reaction Limits from Nonpolar Nanoparticle Agglomeration. *small* **18**, 2204621 (2022).

275. Weisbecker, S., Merritt, V., Weisbecker, C. S., Merritt, M. V & Whitesidesx, G. M. Molecular Self-Assembly of Aliphatic Thiols on Gold Golloids. *Langmuir* **12**, 3763–3772 (1996).

276. Pham, T., Jackson, J. B., Halas, N. J. & Lee, T. R. Preparation and characterization of gold nanoshells coated with self-assembled monolayers. *Langmuir* **18**, 4915–4920 (2002).

277. Lin, M. Y. *et al.* Universality in colloid aggregation. *Lett. to Nat.* **339**, 360–362 (1989).

278. Weitz, D. A., Lin, M. Y. & Sandroff, C. J. Colloidal aggregation revisited: New insights based on fractal structure and surface-enhanced Raman scattering. *Surf. Sci.* **158**, 147–164 (1985).

279. Lin, M. Y. *et al.* Universal reaction-limited colloid aggregation. *Phys. Rev. A* **2**, 3093–

3113 (1990).

280. Waite, T. D., Cleaver, J. K. & Beattie, J. K. Aggregation Kinetics and Fractal Structure of γ-Alumina Assemblages. *J. Colloid Interface Sci.* **241**, 333–339 (2001).

281. Kolb, M. & Jullien, R. Chemically limited versus diffusion limited aggregation. *J. Phys. Lett.* **45**, 977–981 (1984).

282. Wijnen, P. W. J. G., Beelen, T. P. M., Rummens, C. P. J. & van Santen, R. A. Diffusion- and reaction-limited aggregation of aqueous silicate solutions. *J. Non. Cryst. Solids* **136**, 119–125 (1991).

283. Aubert, C. & Cannell, D. S. Restructuring of colloidal silica aggregates. *Phys. Rev. Lett.* **56**, 738–741 (1986).

284. Meakin, P. Strucutre and dynamics of reaction-limited aggregation. *Phys. Rev. A* **36**, 5498–5501 (1987).

285. Sheard, G. J. & King, M. P. Horizontal convection: Effect of aspect ratio on Rayleigh number scaling and stability. *Appl. Math. Model.* **35**, 1647–1655 (2011).

286. Yao, Y., Criddle, C. S. & Fringer, O. B. Competing flow and collision effects in a monodispersed liquid-solid fluidized bed at a moderate Archimedes number. *J. Fluid Mech.* **927**, 1–27 (2021).

287. Xu, A., Shi, L. & Zhao, T. S. Thermal effects on the sedimentation behavior of elliptical particles. *Int. J. Heat Mass Transf.* **126**, 753–764 (2018).

288. Weitz, D. A. & Huang, J. S. Self–Similar Structures and the Kinetics of Aggregation of Gold Colloids. *Kinet. Aggreg. Gelation* 19–28 (1984).

289. Large-Scale Centrifuge. (2022). Available at: https://www.zarm.uni-bremen.de/en/test-center/test-labs/large-scale-centrifuge.html.

290. Chowdhury, D. P., Sorensen, C. M., Taylor, T. W., Merklin, J. F. & Lester, T. W. Application of Photon Correlation Spectroscopy To Brownian Motion System. *Appl. Opt.* **23**, 4149–4154 (1986).

291. Lederle, C. Brownsche Dynamik nanoskopischer, anisotroper Partikel im externen elektrischen Feld. in *Dissertation, Technische Unversität Darmstadt* (2016).

292. Al Rashid, A., Khan, S. A., G. Al-Ghamdi, S. & Koç, M. Additive manufacturing of polymer

nanocomposites: Needs and challenges in materials, processes, and applications. *J. Mater. Res. Technol.* **14**, 910–941 (2021).

293. Lattuada, M. Predictive model for diffusion-limited aggregation kinetics of nanocolloids under high concentration. *J. Phys. Chem. B* **116**, 120–129 (2012).

294. Babick, F., Gropp, S., Kätzel, U. & Vorbau, M. Dynamic light scattering of dispersed fumed silica aggregates. *Powder Technol.* **217**, 39–45 (2012).

295. Carl, N., Prévost, S., Fitzgerald, J. P. S. & Karg, M. Salt-induced cluster formation of gold nanoparticles followed by stopped-flow SAXS, DLS and extinction spectroscopy. *Phys. Chem. Chem. Phys.* **19**, 16348–16357 (2017).

296. Lenher, V. & Kao, C. H. Studies on the Chemistry of Gold. *J. Phys. Chem.* **30**, 126–129 (1926).

297. Wei, J., Schaeffer, N. & Pileni, M. P. Ag nanocrystals: 1. Effect of ligands on plasmonic properties. *J. Phys. Chem. B* **118**, 14070–14075 (2014).

298. Lauth, G. J. & Kowalczyk, J. *Flüssigkristalle - Einführung in die Physik und Chemie der Grenzflächen und Kolloide*. (2016).

299. Dabaghi, M. & Hilger, I. Magnetic nanoparticles behavior in biological solutions; The impact of clustering tendency on sedimentation velocity and cell uptake. *Materials (Basel).* **13**, 1–11 (2020).

300. Khasanshin, T. S. & Shchemelev, A. P. The thermodynamic properties of n-tetradecane in liquid state. *Thermophys. Prop. Mater.* **40**, 207–211 (2002).

301. Fang, Y. *et al.* Preparation and Thermal Performance of Silica/n-Tetradecane Microencapsulated Phase Change Material for Cold Energy Storage. *Energy and Fuels* **30**, 9652–9657 (2016).

7 Appendix

The following sections have been published in "Dynamic Light Scattering on Nanoparticles in Microgravity in a Drop Tower" by Pyttlik, Kuttich and Kraus in *Microgravity Science and Technology*, in 2022 [196] and in "Microgravity Removes Reaction Limits from Nonpolar Nanoparticle Agglomeration" by Pyttlik, Kuttich and Kraus in *Small*, in 2022.[274]

7.1 Comparison sedimentation and diffusion

To compare the sedimentation and diffusion of hexadecanethiol-capped gold nanoparticles in tetradecane, the time in which the agglomerates move the distance equal to its hydrodynamic diameter is regarded. In the following the hydrodynamic diameter d_H is expressed as two times of the hydrodynamic radius r_H. First the sedimentation of the agglomerates is calculated.

7.1.1 Sedimentation

Sedimentation of a particle through a medium can be described as the balance of three forces, gravitation F_G, buoyancy F_B and friction F_F.[298] The friction F_F of the system can be described using the hydrodynamic radius of the particle r_H, the hydrodynamic viscosity of the solvent η, and the sedimentation velocity of the particle v, see **Equation (40)**.[298]

$$F_F = 6\pi \cdot \eta \cdot r_H \cdot v \tag{40}$$

The Gravitation F_G is expressed by the gravitational constant 1 g and the mass m_P of the particle, see **Equation (41)**.[298] The mass of the particle can thereby also be described by its volume V_P and its density ρ_P, or by the agglomeration number N_{Agglo} and the core radius of the particles r_{Core}, see **Equation (42)**.

$$F_G = m_P \cdot g \tag{41}$$

$$F_G = \rho_P \cdot V_P \cdot g = \rho_P \cdot N_{Agg} \cdot \frac{4}{3}\pi \cdot r_C^3 \cdot g \tag{42}$$

The buoyancy F_B of the particles depends on the gravitational constant 1 g and the mass of the solvent, which is displaced by the particle m_S, see **Equation (43)**.[298] The mass of the displaced solvent equals the volume of the particle V_P times the density of the solvent ρ_S, see **Equation (44)**.

$$F_B = m_S \cdot g \tag{43}$$

$$F_B = \rho_S \cdot V_P \cdot g = \rho_S \cdot N_{Agg} \cdot \frac{4}{3} \pi \cdot r_C^3 \cdot g \tag{44}$$

The agglomeration number N_{Agglo} is estimated by using the ratio of the agglomerated particle r_H and the hydrodynamic radius of a single particle r_{H0}, see **Equation (45)**.

$$N_{Agglo} = \frac{r_H^3}{r_{H0}^3} \tag{45}$$

Assuming a steady state, when the particle moves with constant velocity through the medium, the three forces F_G, F_B, and F_F will add up to zero, see **Equation (46)**.

$$F_G + F_B + F_F = 0 \tag{46}$$

The sedimentation velocity v of the particle depends on the density difference of the particle ρ_P and the solvent ρ_S, the core and the hydrodynamic radius of the particle (r_{Core} and r_H), and the gravitational constant g, see **Equation (47)**.[299]

$$v = \frac{2 \cdot r_{Core}^3 \cdot g \cdot (\rho_P - \rho_S) \cdot r_H^2}{9 \cdot \eta \cdot r_H^3} \tag{47}$$

At this state, the time t_{Sed}, which a particle needs to sediment a distance twice of its hydrodynamic radius r_H, can be calculated by using the sedimentation velocity v, see **Equation (48)**.

$$t_{Sed} = \frac{2r_H}{v} = \frac{9 \cdot \eta \cdot r_{H0}^3}{r_{Core}^3 \cdot g \cdot (\rho_P - \rho_S) \cdot r_H} \tag{48}$$

7.1.2 Diffusion

Diffusion of the particle can be characterized by the diffusion coefficient D_{Diff}. The diffusion coefficient can be described according to the Stoke-Einstein relation by using **Equation (49)**.[188]

$$D_{Diff} = \frac{k_B \cdot T}{6 \cdot \pi \cdot \eta \cdot r_H} \tag{49}$$

The distance a particle moves due to diffusion after a given time t, can be described as the root mean squared displacement $RMSD$, see **Equation (50)**.

$$RMSD = \sqrt{6 \cdot D_{Diff} \cdot t} \qquad (50)$$

The diffusion time t_{Diff} after which a particle moved a distance of a RMSD equal to twice its hydrodynamic radius r_H, can be described using **Equation (51)**.

$$t_{Diff} = \frac{4 \cdot r_H^2}{6 \cdot D_{Diff}} = \frac{4 \cdot \pi \cdot \eta \cdot r_H^3}{k_B \cdot T} \qquad (51)$$

7.1.3 Ratio between diffusion and sedimentation

The ratio Γ of the diffusion time t_{Diff} and the sedimentation time t_{Sed}, can be described according to **Equation (52)**.

$$\Gamma = \frac{t_{Diff}}{t_{Sed}} = \frac{4\pi \cdot \eta \cdot r_H^3 \cdot r_{Core}^3 \cdot g \cdot (\rho_P - \rho_S) \cdot r_H}{k_B \cdot T \cdot 9 \cdot \eta \cdot r_{H0}^3} = \frac{4\pi \cdot g \cdot (\rho_P - \rho_S) \cdot r_{Core}^3 \cdot r_H^4}{9 \cdot k_B \cdot T \cdot r_{H0}^3} \qquad (52)$$

Equation (52) is applied to the used particle system, gold nanoparticles dispersed in tetradecane. The core radius of the particles is r_{Core} = 3.9 nm and the hydrodynamic radius of a single particle is r_{H0} =13 nm. At a temperature of T = 293 K the ratio of the sedimentation time t_{Sed} and the diffusion time t_{Diff} is given by $\Gamma \approx 10^{-11}$ (r_H nm^{-1})^4.

For deagglomerated nanoparticles, the hydrodynamic radius of the agglomerates r_H equals the hydrodynamic radius of a single particle r_{H0}, therefore, the ratio Γ is approximately 10^{-8}. Indicating that the diffusion of the deagglomerated particles is 10^8 times faster than its sedimentation, see **Equation (53)** and **Equation (54)**.

$$\Gamma = \frac{t_{Diff}}{t_{Sed}} \approx 10^{-8} \qquad (53)$$

$$t_{Diff} \approx 10^{-8} \cdot t_{Sed} \qquad (54)$$

Assuming an agglomerated nanoparticle sample with a hydrodynamic radius of r_H = 100 nm, the ratio between the diffusion time t_{Diff} and the sedimentation time t_{Sed} is approximately 10^{-3}, indicating that even for the agglomerated particles the diffusion is still 10^3 times faster than the sedimentation.

Assuming the system has a ratio of $\Gamma = 0.1$ which is at least needed to be able to detect the diffusion and the sedimentation simultaneously, the agglomerates would have a hydrodynamic radius of at least 400 nm, and a hydrodynamic diameter of 800 nm. Assuming on ground particles with a hydrodynamic diameter of 800 nm were formed during the agglomeration process, the agglomerates would have a sedimentation velocity of approximately $v \approx 4 \cdot 10^{-12}$ m s^{-1}, see **Equation (47)**, resulting in a movement of 0.04 nm of the agglomerates after 10 s (without considering the displacement of the agglomerates due to diffusion). Consequently, the formation of larger agglomerates on ground and their undetected sedimentation during the DLS measurements is unlikely.

7.2 Calculation of the Rayleigh number and Archimedes number

The Rayleigh number is a dimensionless number to describe the convection in a fluid.[285] The Archimedes number is a dimensionless number to describe the motion of different fluids due to their different densities. By applying the Archimedes number on a colloidal system, it can be used to characterize the sedimentation of the particles though the medium.[286] To calculate the Rayleigh number and the Archimedes number, the following parameters were used, see **Table 10.**

Table 10: Parameters used to calculate Rayleigh number and Archimedes number. From Pyttlik *et al.*, **2022.**[274]

Density of gold	ρ_{Au}	$19.3 \cdot 10^3$ kg/m^3
Density of tetradecane[300]	ρ_{Tetra}	$0.76 \cdot 10^3$ kg/m^3
Dynamic viscosity of tetradecane[200]	η_{Tetra}	$2.13 \cdot 10^{-3}$ Pa s
Thermal conductivity of tetradecane[301]	k_{Tetra}	0.098 W/m/K
Isobaric heat capacity of tetradecane[300]	c_{P_Tetra}	$2.3 \cdot 10^3$ J/kg/K
Thermal expansion coefficient of tetradecane[300]	β_{Tetra}	$0.9 \cdot 10^{-3}$ 1/K
Characteristic particle length	l	$1 \cdot 10^{-8}$ m
Characteristic length	z	$5 \cdot 10^{-3}$ m
Temperature difference	ΔT	60 K

While on ground, the parameter a = 9.81 m s^{-2} is applicable, in microgravity, the parameter a = 9.81·10^{-6} m s^{-2} was used.

The Rayleigh number can be calculated according to **Equation (55)**.[285]

$$Ra = a \, \frac{\beta \cdot \rho_{Tetra} \cdot c_{P\_Tetra} \cdot \Delta T \cdot z^3}{\eta_{Tetra} \cdot k_{Tetra}} \tag{55}$$

On ground, a Rayleigh number of approximately $Ra \approx 10^5$ and in microgravity $Ra \approx 10^{-1}$ was found. The strong reduction of the Rayleigh number indicates the strong reduction of the convection in microgravity, even with the large temperature drop during the agglomeration experiments.[285] As expected, effects of convection can be neglected in microgravity.

The Archimedes number was calculated according to **Equation (56)**.[286]

$$Ar = a \cdot \frac{l^3 \cdot \rho_{Tetra} \cdot (\rho_{Au} - \rho_{Tetra})}{\eta_{Tetra}^2} \tag{56}$$

On ground, an Archimedes number of approximately $Ar \approx 10^{-8}$ and in microgravity $Ar \approx 10^{-14}$ was found. In microgravity the Archimedes number is strongly decreased, showing the strongly decreased sedimentation of the particles.[287]

7.3   SAXS data of gold nanoparticles at different temperatures
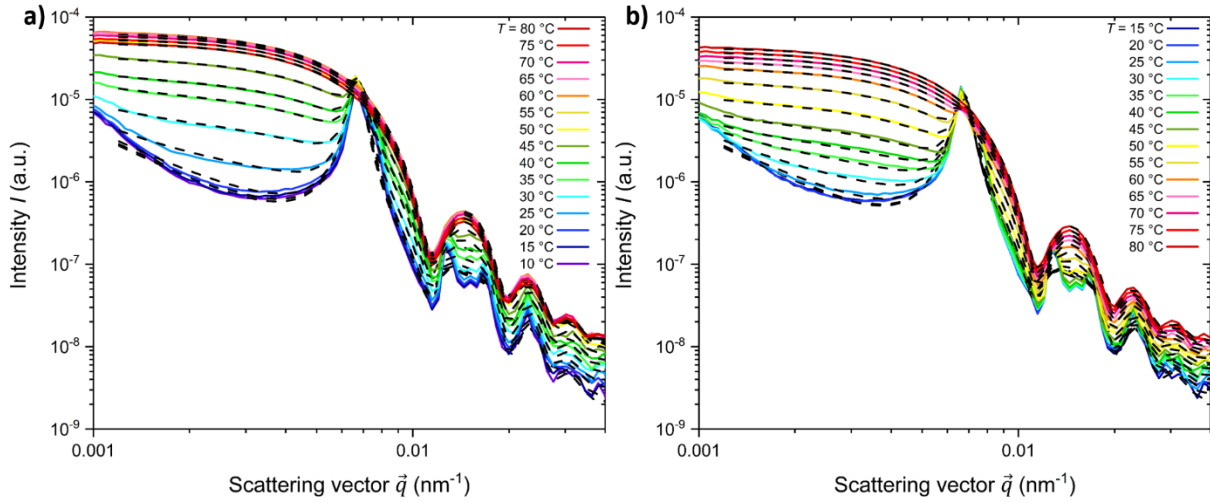
Figure 53: Recorded SAXS data of hexadecanethiol gold nanoparticles in tetradecane. The particles have a core diameter of d_{Core} = 7.8 nm (± 0.5 nm) and a hydrodynamic diameter of d_H = 13 nm (± 1 nm). (a) The particles were heated to 75 °C and cooled down to 5 °C. (b) The particles were reheated back to 75 °C.

7.4   Autocorrelation functions of silica nanoparticles
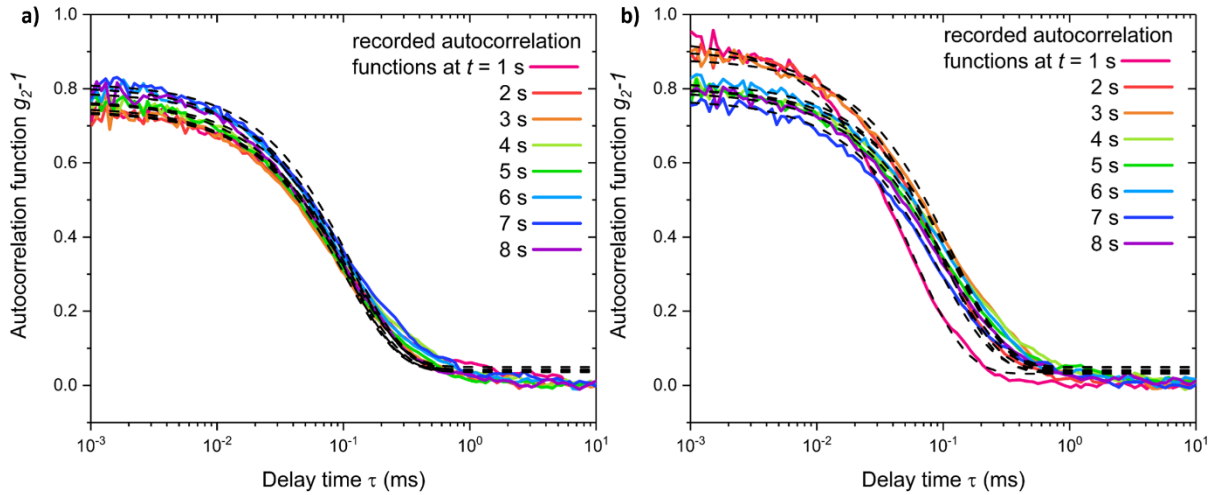
Figure 54: Consecutive recorded autocorrelation functions (colored, solid lines) and corresponding fits (black, dashed lines), with an integration time of 1 s of silica nanoparticles in water, with a hydrodynamic diameter of d_H = 25 nm (± 3 nm). The measurement was performed at a constant temperature of T = 20 °C (a) under normal conditions (1 g) and (b) in microgravity (µ g).

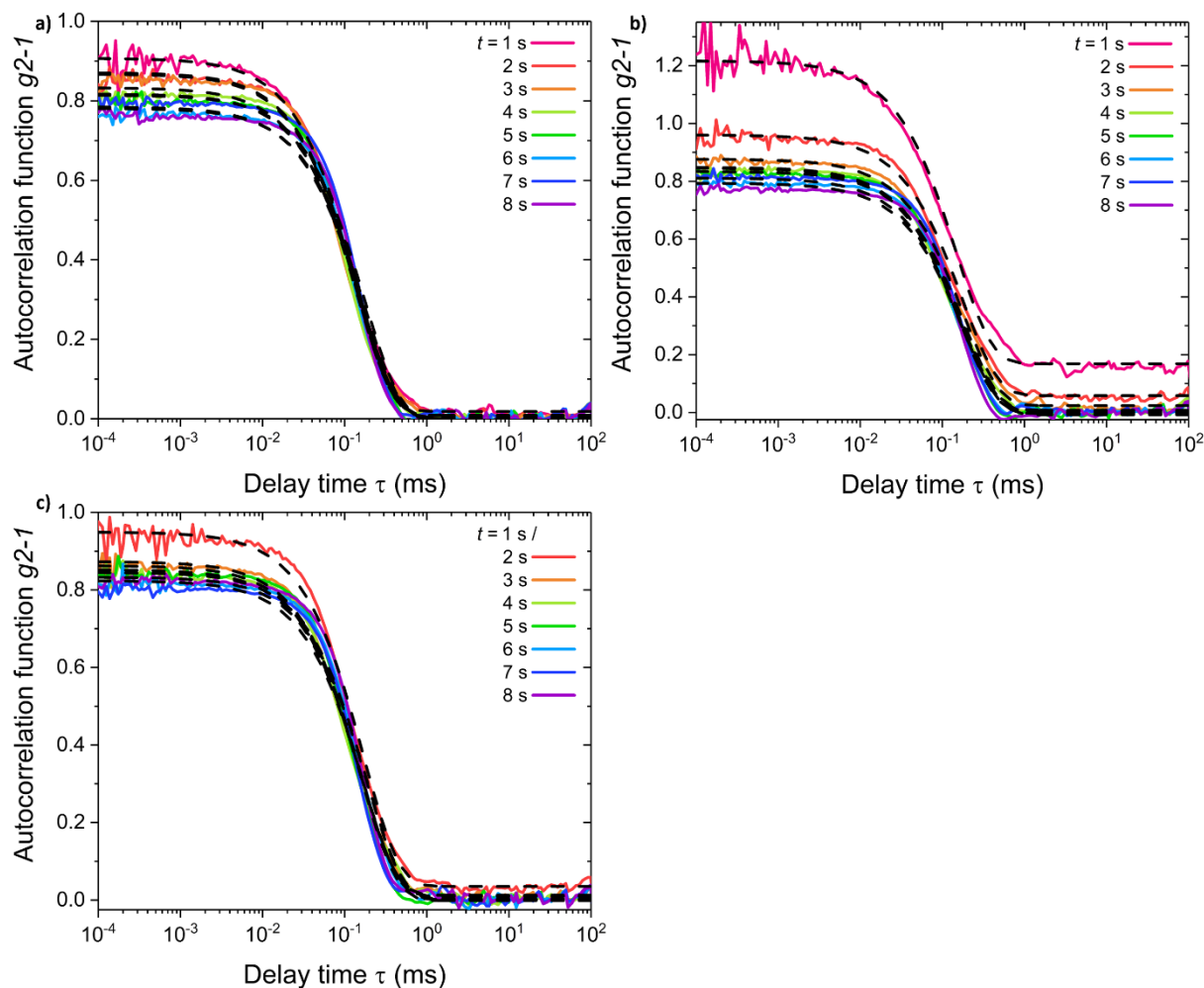## 7.5 Autocorrelation functions of oleylamine-capped gold nanoparticles
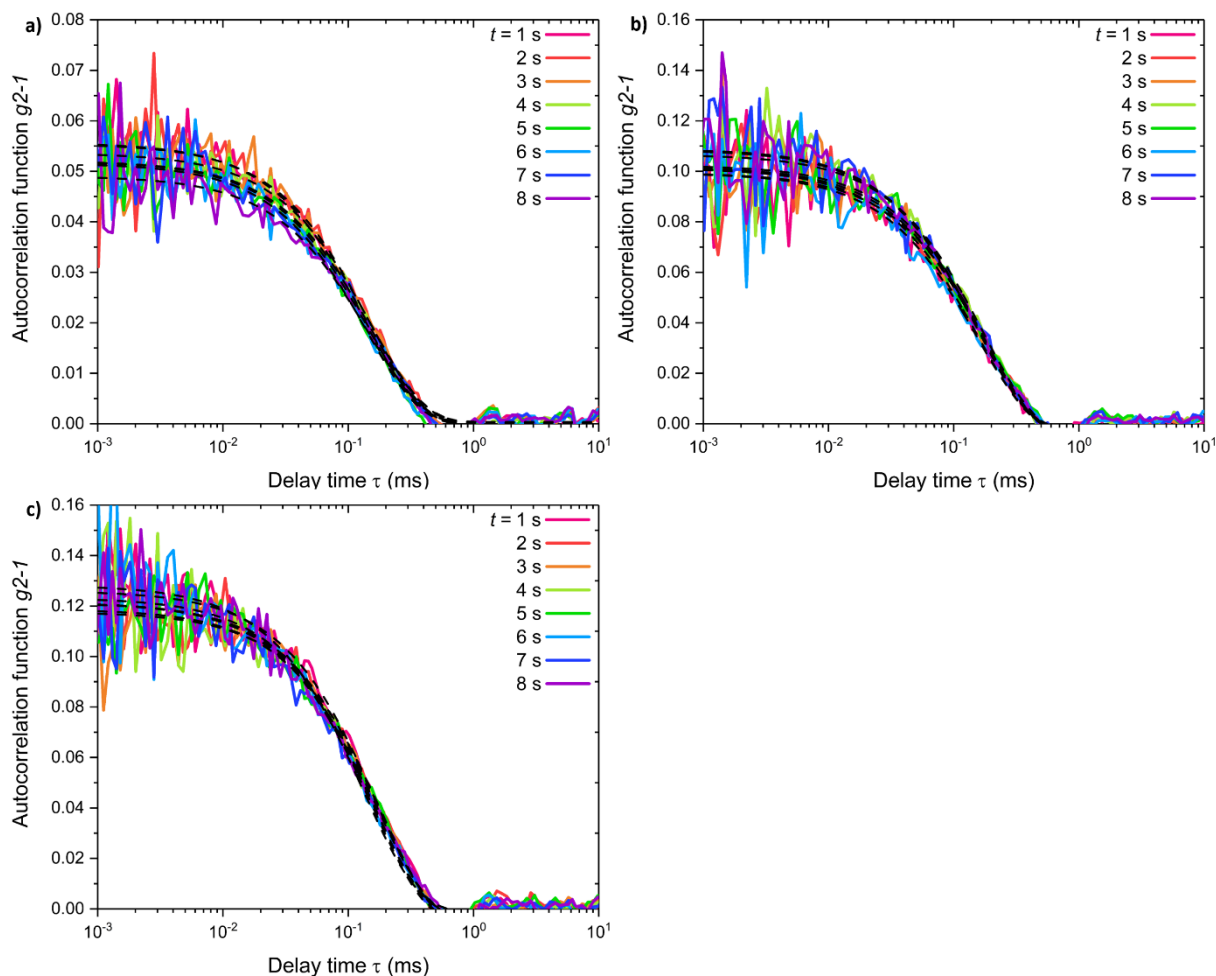
Figure 55: Consecutive recorded autocorrelation functions (colored, solid lines) and corresponding fits (black, dashed lines), with an integration time of 1 s of oleylamine-capped gold nanoparticles in tetradecane. The particles had a hydrodynamic diameter of d_H = 21 nm (± 1 nm). The dispersion had a gold concentration of c = 0.72 mg mL^{-1} (± 0.03 mg mL^{-1}). The measurement was performed at a constant temperature of T = 20 °C under normal conditions (1 g). The DLS measurements was repeated three times a)-c).
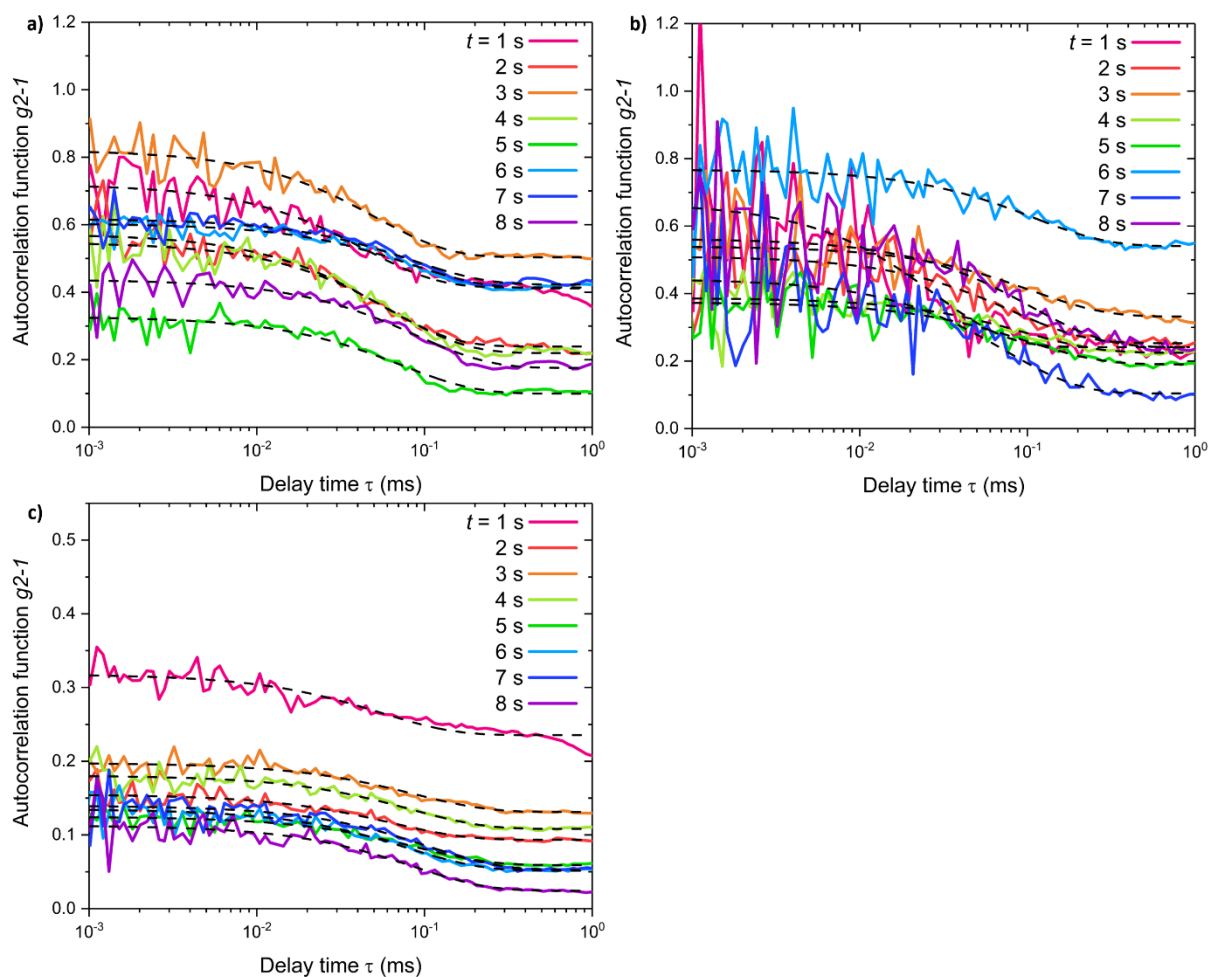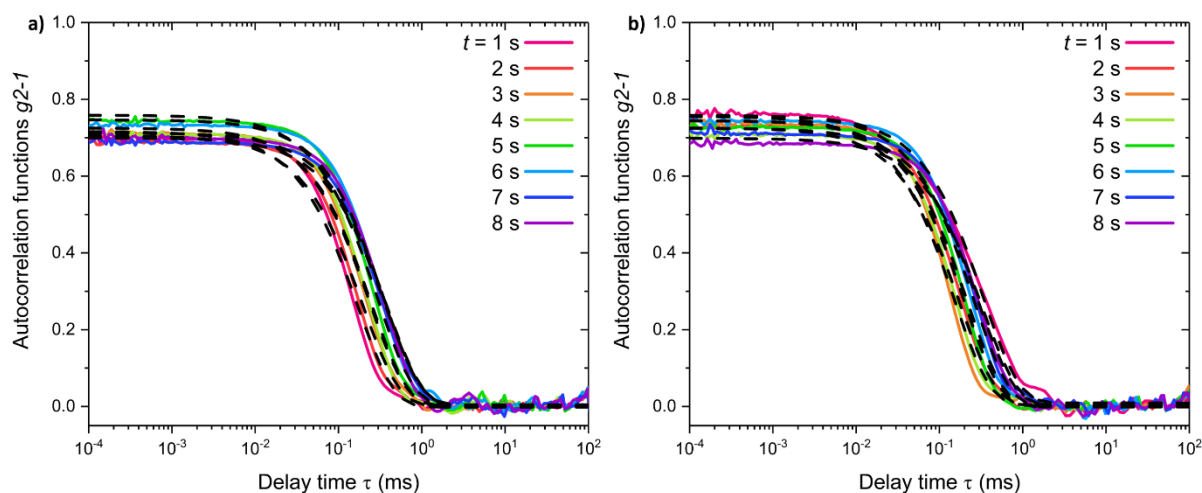
Figure 56: Consecutive recorded autocorrelation functions (colored, solid lines) and corresponding fits (black, dashed lines), with an integration time of 1 s of oleylamine-capped gold nanoparticles in tetradecane. The particles had a hydrodynamic diameter of d_H = 21 nm (± 1 nm). The dispersion had a gold concentration of c = 0.72 mg mL^{-1} (± 0.03 mg mL^{-1}). The measurement was performed with a rapid temperature drop (70 °C to 10 °C) under normal conditions (1 g). The DLS experiment was repeated three times a)-c).
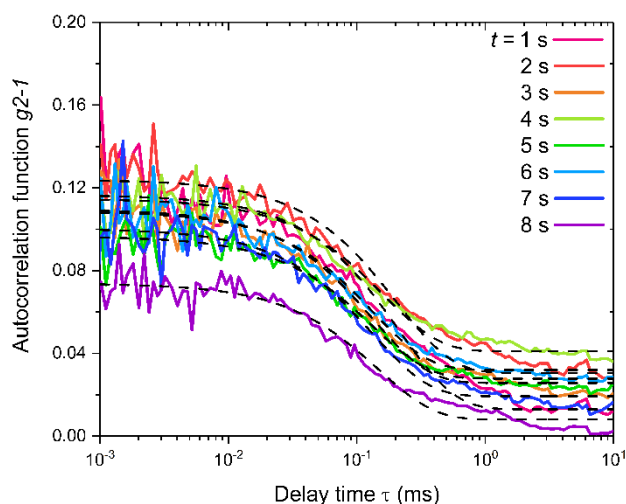
Figure 57: Consecutive recorded autocorrelation functions (colored, solid lines) and corresponding fits (black, dashed lines), with an integration time of 1 s of oleylamine-capped gold nanoparticles in tetradecane. The particles had a hydrodynamic diameter of d_H = 21 nm (± 1 nm). The dispersion had a gold concentration of c = 0.72 mg mL^{-1} (± 0.03 mg mL^{-1}). The measurement was performed at a constant temperature of T = 20 °C in microgravity (μ g) by using a catapult launch.
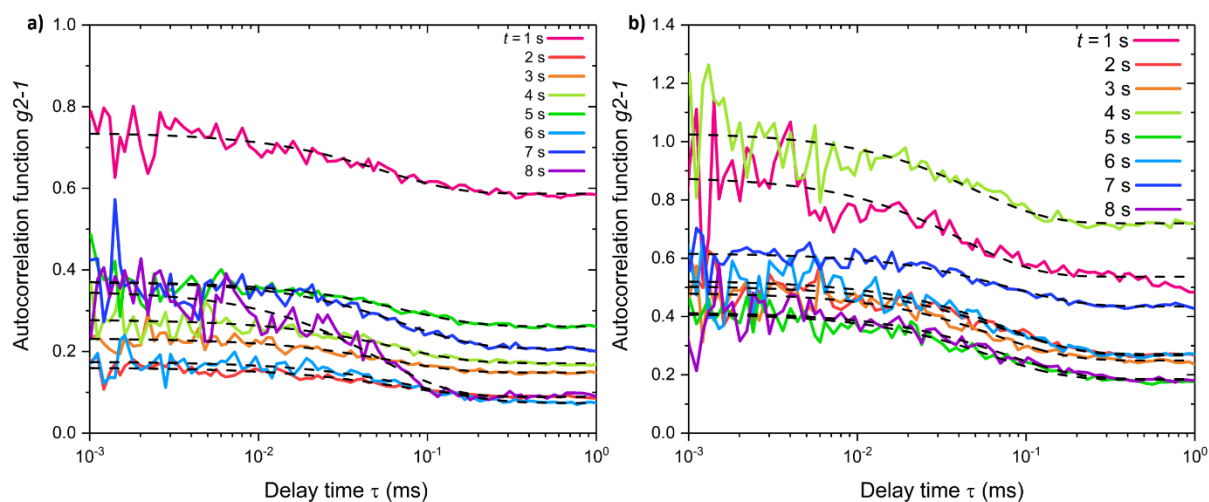
Figure 58: Consecutive recorded autocorrelation functions (colored, solid lines) and corresponding fits (black, dashed lines), with an integration time of 1 s of oleylamine-capped gold nanoparticles in tetradecane. The particles had a hydrodynamic diameter of d_H = 21 nm (± 1 nm). The dispersion had a gold concentration of c = 0.72 mg mL^{-1} (± 0.03 mg mL^{-1}). The measurement was performed with a temperature drop (70 °C to 10 °C) in microgravity (μ g) by using a catapult launch. The DLS experiments were repeated two times a)-b).
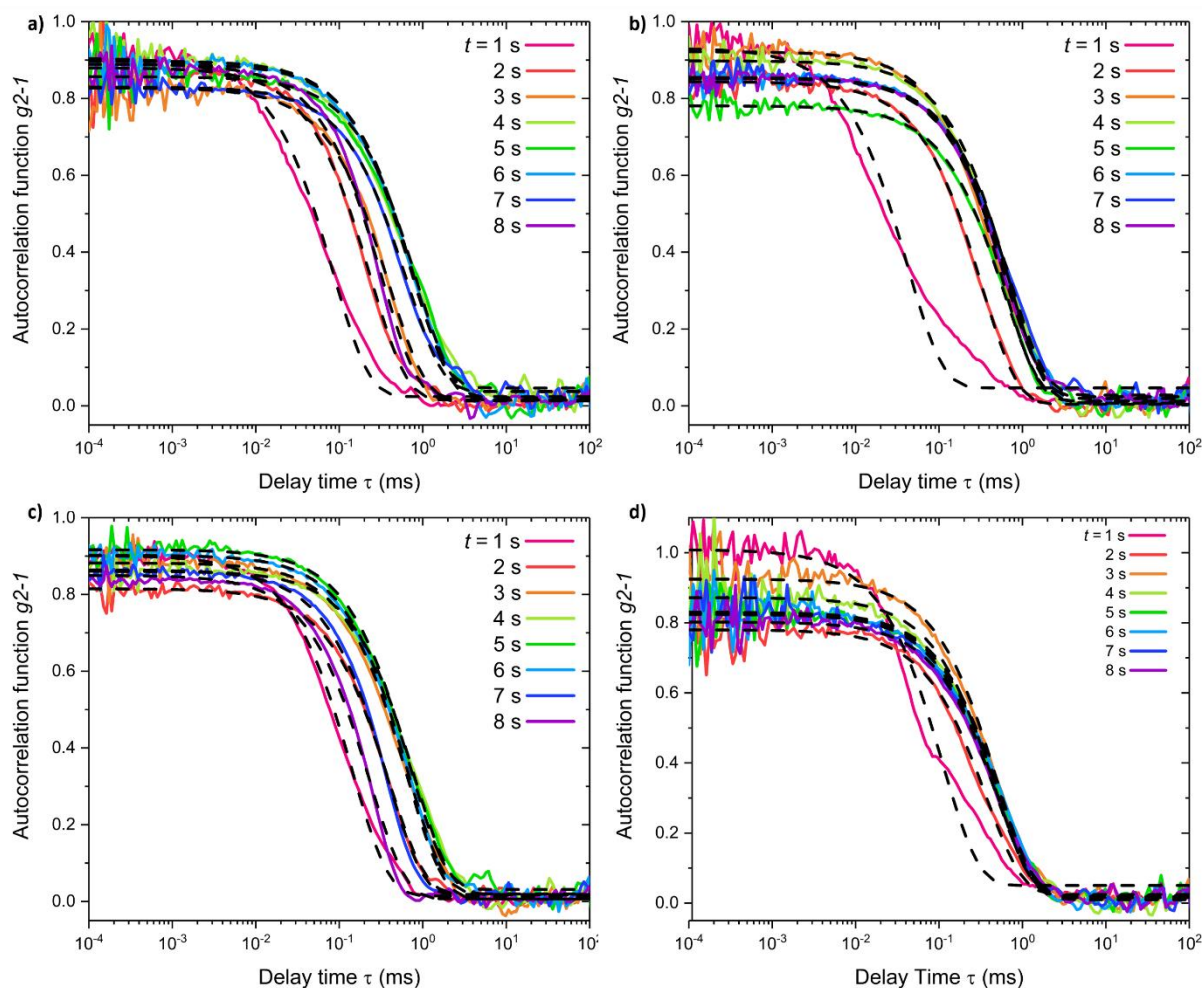
7.6 Autocorrelation functions of hexadecanethiol-capped gold nanoparticles

Figure 59: Consecutive recorded autocorrelation functions (colored, solid lines) and corresponding fits (black, dashed lines), with an integration time of 1 s of hexadecanethiol-capped gold nanoparticles in tetradecane. The particles had a hydrodynamic diameter of d_H = 13 nm (± 1 nm). The dispersion had a gold concentration of c = 1.03 mg mL^{-1} (± 0.12 mg mL^{-1}). The measurement was performed with a temperature drop (70 °C to 10 °C) on ground (1 g). The DLS experiment was repeated three times a)-c). c) At t = 1 s, the liquid injected influenced the autocorrelation function, so the data could not be analyzed.
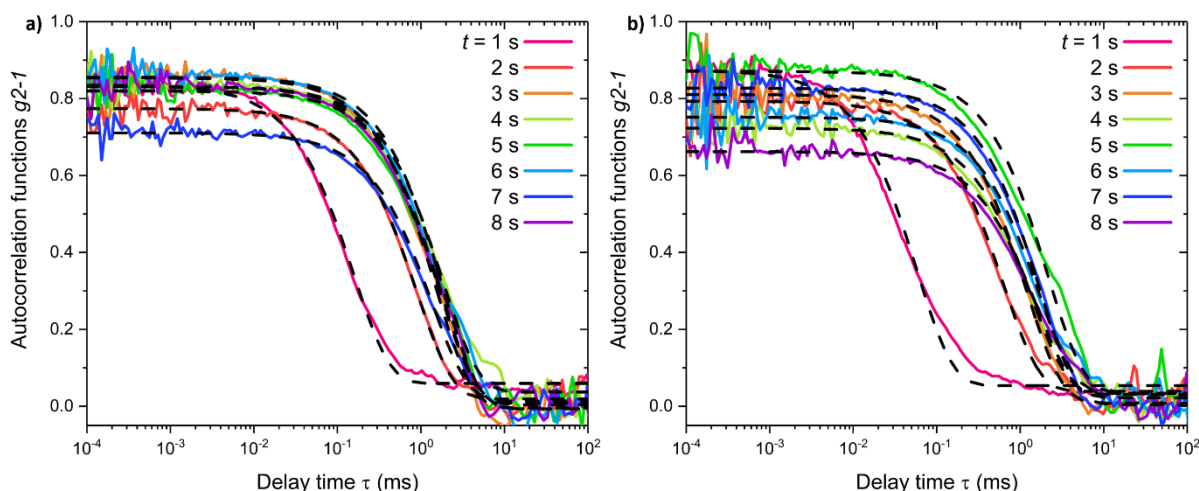
Figure 60: Consecutive recorded autocorrelation functions (colored, solid lines) and corresponding fits (black, dashed lines), with an integration time of 1 s hexadecanethiol-capped gold nanoparticles in tetradecane. The particles had a hydrodynamic diameter of d_H = 13 nm (± 1 nm). The dispersion had a gold concentration of c = 2.75 mg mL^{-1} (± 0.04 mg mL^{-1}). The measurement was performed with a temperature drop (70 °C to 10 °C) on ground (1 g). The DLS experiment was repeated two times a)-b).
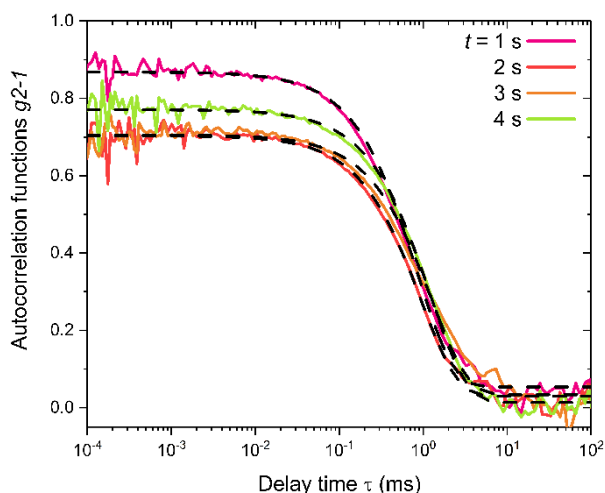
Figure 61: Consecutive recorded autocorrelation functions (colored, solid lines) and corresponding fits (black, dashed lines), with an integration time of 1 s of hexadecanethiol-capped gold nanoparticles in tetradecane. The particles had hydrodynamic diameter of d_H = 13 nm (± 1 nm). The dispersion had a gold concentration of c = 0.86 mg mL^{-1} (± 0.16 mg mL^{-1}). The measurement was performed with a temperature drop (70 °C to 10 °C) in microgravity (µ g) by using a catapult launch. The DLS experiment was repeated four times a)-d).

Figure 62: Consecutive recorded autocorrelation functions (colored, solid lines) and corresponding fits (black, dashed lines), with an integration time of 1 s of hexadecanethiol-capped gold nanoparticles in tetradecane. The particles had a hydrodynamic diameter of d_H = 13 nm (± 1 nm). The dispersion had a gold concentration of c = 3.27 mg mL^{-1} (± 0.79 mg mL^{-1}). The measurement was performed with a temperature drop (70 °C to 10 °C) in microgravity (µ g) by using a catapult launch. The DLS experiment was repeated two times a)-b).

Figure 63: Consecutive recorded autocorrelation functions (colored, solid lines) and corresponding fits (black, dashed lines), with an integration time of 1 s of hexadecanethiol-capped gold nanoparticles in tetradecane. The particles had a hydrodynamic diameter of d_H = 13 nm (± 1 nm). The dispersion had a gold concentration of c = 2.67 mg mL^{-1}. The measurement was performed with a temperature drop (70 °C to 10 °C) in microgravity (µ g) by performing a drop experiment.